Engineering Journal

American Institute of Steel Construction

Fourth Quarter 2016 Volume 53, No. 4

www.aisc.org

Stability of Rectangular Connection Elements

BO DOWSWELL

ABSTRACT

Connection elements are commonly designed using the flexural buckling and lateral-torsional buckling provisions in AISC *Specification* Sections E3 and F11, respectively, as well as the combined-load requirements of Section H1. Because these provisions were developed for main members, their accuracy for designing connection elements is questionable. The factors affecting the stability of connection elements are discussed, with an emphasis on the differences between main members and connection elements. The available experimental and theoretical results are compared to the AISC *Specification* equations. Where required, new equations are derived, and practical design solutions are recommended. Recommendations are also made for connection elements subjected to combined axial and flexural loads. Examples are provided to illustrate the proposed design procedures for double-coped beams.

Keywords: connections, rectangular elements, stability, flexural buckling, lateral-torsional buckling.

INTRODUCTION

In design, simplifying assumptions are required to reduce complex problems to idealized models with well-documented solutions and predictable behavior. Connections are often divided into rectangular elements, which are modeled as beams, columns and tension members. However, connection elements may not behave the same as the main members in a structure due to smaller length-to-depth ratios, unpredictable stress distributions, ambiguous boundary conditions, different residual stress patterns, and large out-of-flatness tolerances. These differences are usually insignificant for compact connection elements, where yielding is the primary limit state; however, they may be detrimental to connection elements subject to buckling.

AISC *Specification* (AISC, 2010a) Sections E3 for flexural buckling, F11 for lateral-torsional buckling, and H1 for combined loads were developed for designing main structural members. Although the applicability of these *Specification* provisions for the design of connection elements has not been verified, they are commonly used to design gusset plates and other connection elements. Inaccuracies in connection design models caused by adapting member design equations to connection elements can lead to a reduction in stability.

The purpose of this paper is to determine the accuracy of the AISC *Specification* stability provisions for designing rectangular connection elements. The factors affecting the stability of connection elements are discussed, with an emphasis on the differences between main members and connection elements. The available research relevant to the stability of connection elements is reviewed, and the available experimental and theoretical results are compared to the AISC *Specification* equations. Where required, new equations are derived and practical design solutions are recommended.

CONNECTION DESIGN MODELS

Several existing solutions are available, where the effective length factors, K, and lateral-torsional buckling modification factors, C_b, have been calibrated with experimental and/or finite element results. Some of these solutions are presented in a qualitative manner to provide background information on the applicability of *Specification* Sections E3, F11 and H1 to the design of connection elements.

Gusset Plates in Compression

Thornton (1984) proposed a method to calculate the flexural buckling strength of corner gusset plates (Figure 1a), where the gusset plate is modeled as a rectangular column as shown in Figure 1b. The buckling strength is calculated using the equations in Section E3 of the AISC *Specification*. As experimental and finite element data became available, the effective length factors were calibrated to provide more accurate solutions (Dowswell, 2006; Dowswell, 2012a).

Lapped Gusset Plates in Compression and Flexure

Due to a high level of erection efficiency, HSS bracing connections are sometimes fabricated using lapped gusset plate connections, shown in Figure 2a. The connection consists of a lug plate shop welded to a slot on the HSS brace centerline, which is field bolted to the gusset plate. The eccentricity

---

Bo Dowswell, P.E., Ph.D., Principal, ARC International, LLC, Birmingham, AL. Email: bo@arcstructural.com

Paper No. 2014-19

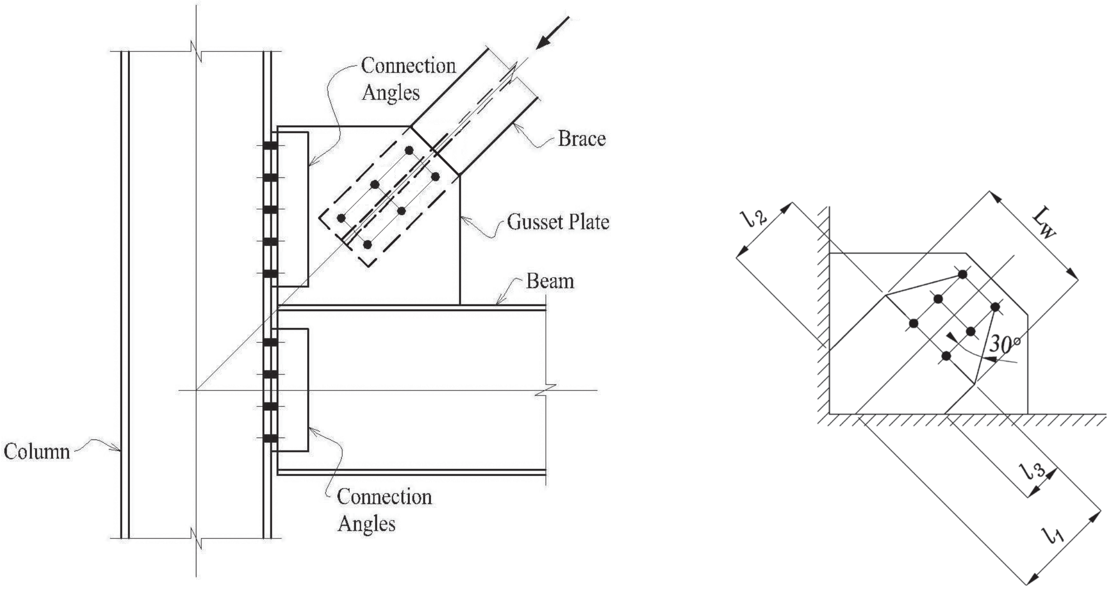

(a) *(b)*

Fig. 1. Gusset plate in compression: (a) cover gusset plate; (b) equivalent column.

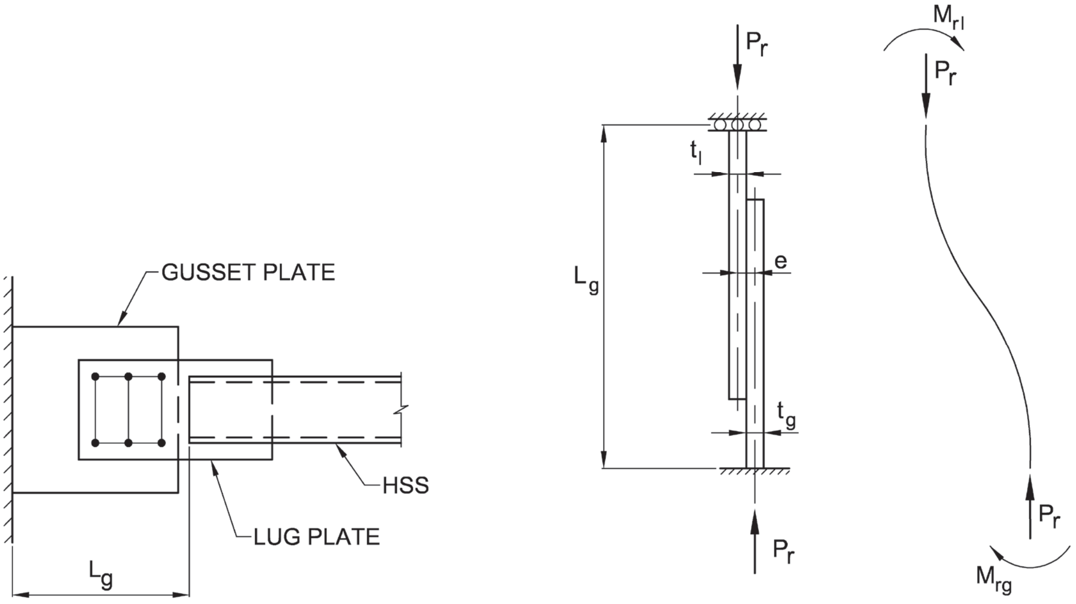

(a) *(b)*

Fig. 2. Lapped gusset plate in compression and flexure: (a) lapped gusset plate; (b) equivalent beam-column.

between the centerline of the brace and the center of the gusset plate causes an eccentricity that significantly lowers the compression strength of the connection.

In AISC Design Guide 24 Hollow Structural Section Connections (Packer et al., 2010), the plates are modeled as a beam-column as shown in Figure 2b. The buckling strength is calculated using the beam-column provisions of AISC *Specification* Section H1 and the flexural buckling provisions in Section E3. This beam-column model was first published in the AISC *Hollow Structural Sections Connections Manual* (AISC, 1997). Clifton (2006), Clifton et al. (2007), Albermani et al. (2009), Hogan and Collins (2010), and Wilkinson et al. (2010) have refined the design procedure.

Double-Coped Beams

In beam-to-girder connections, the beam is usually coped to allow a standard connection to the girder web. If the beam and girder are of equal depth, both flanges must be coped as shown in Figure 3a. Due to the flexural and shear stresses in the coped portion of the web, web buckling can limit the local strength.

The AISC *Steel Construction Manual* (AISC, 2011) provides a semi-empirical design procedure for localized stability of double-coped beams. The AISC *Manual* procedure was developed by Cheng et al. (1984) by modeling the cope as a cantilever beam with a length equal to the cope length, *e*, as shown in Figure 3b. Dowswell and Whyte (2014) developed equations for lateral-torsional buckling modification factors, C_b, for use with the lateral-torsional buckling provisions in Section F11 of the AISC *Specification*.

Wrap-Around Gusset Plates

Where a horizontal brace is located at a beam-to-column intersection, the gusset plate must be cut out around the column as shown in Figure 4a. Due to the unconventional geometry, flexural stresses develop in the plate that must be accounted for in design. The assumed load distribution in wrap-around gusset plate connections is shown in Figure 4b, where the moment varies linearly along the length of each leg, and the maximum moment is at the reentrant corner.

Dowswell (2005) showed that the strength of each leg can be calculated based on an equivalent cantilever beam model. Dowswell (2012b) recommended using the lateral-torsional buckling provisions in Section F11 of the AISC *Specification* with different buckling lengths that were based on experimental behavior.

FACTORS AFFECTING STABILITY OF CONNECTION ELEMENTS

The primary factors influencing the stability of connection elements, such as buckling length and sectional properties, are explicitly addressed in the equations of *Specification* Sections E3 and F11. Other factors, including material and geometric imperfections, were considered in the development of the equations; however, the influence of these variables is defined only implicitly.

Although some imperfections can be beneficial, they usually have a detrimental effect on connection stability. Buckling strength decreases with increasing geometric imperfections, which are typically much larger for connection elements than for main members. Compression residual stresses decrease the elastic range of behavior, causing a decrease in buckling strength.

Geometric Imperfections

Although the AISC *Code of Standard Practice* (AISC, 2010b) requires a maximum out-of-straightness of $L/1{,}000$ for straight compression members, the column curve in AISC *Specification* Section E3 was developed for column shapes with an initial out-of-straightness of $L/1{,}500$ (Bjorhovde, 1988). This is because Bjorhovde (1988) calculated an average out-of-straightness of $L/1{,}500$ for wide flange shapes used in North America, where L is the length between points of lateral support. For lateral-torsional buckling, AISC *Specification* Section F11 was developed based on a geometrically perfect member.

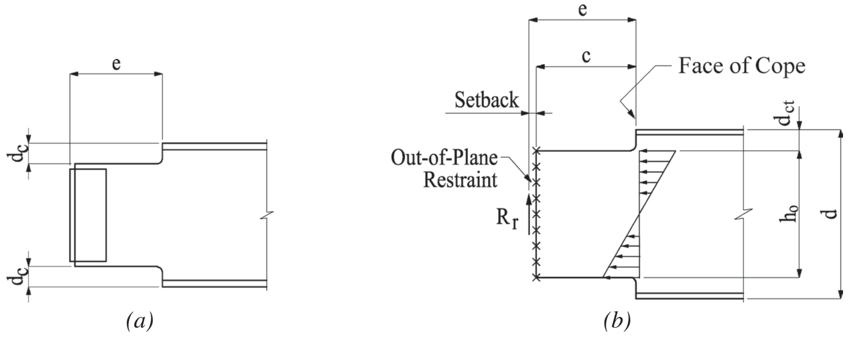

(a) (b)

Fig. 3. Double-coped beam: (a) double-coped beam; (b) design model.

Geometric imperfections in connection elements can come from mill tolerances, fabrication operations, shipping damage, or distortion caused by pulling out-of-tolerance members together during erection. The out-of-flatness of connection elements are usually much larger than the out-of-straightness of a typical column when expressed as the imperfection-to-buckling length ratio. However, there are no standard tolerances for in-place connection elements. ASTM A6 (ASTM, 2013) specifies a permissible camber of 0.025 in./ft and a permissible variation from flat of 0.25 in. for carbon steel plates less than 36 in. long. This is equivalent to a permissible out-of-flatness of $L/480$, which is twice the permissible out-of-straightness of columns less than 30 ft long. The ASTM standard is applicable only to manufacturing tolerances and does not address the tolerances for plates after fabrication and erection is complete. Fouad et al. (2003) surveyed state departments of transportation, manufacturers and engineers to determine the current state of practice regarding flatness tolerances for connection plates and base plates. They recommended using the flatness requirements of ASTM A6 as a post-fabrication tolerance. Because geometric imperfections can significantly reduce the buckling strength of connection elements, they must be considered in the development of design recommendations.

Residual Stresses

Residual stresses are self-equilibrating stresses that are built into members as a result of the manufacturing and fabrication operations. Thermal residual stresses are caused by uneven cooling of the material after hot rolling, welding, and flame cutting. For bars and universal mill (UM) plates with rolled edges, the across-width residual stress pattern is shown in Figure 5a.

Welded and flame-cut members have tensile residual stresses at the location of the heat input. Plates with thermally cut edges have a residual stress pattern that varies across the width as shown in Figure 6a, with very high tensile residual stresses at the cut edges and balancing compression residual stresses at the center of the width.

According to Bjorhovde et al. (2001), the magnitude of the tension residual stress for oxyfuel thermal cutting is “generally around 60 to 70 ksi, regardless of the original material properties.” This was confirmed by Spragen and Claussen (1937), Rao and Tall (1961), Tall (1964), Dwight and Ractliffe (1967), McFalls and Tall (1969), and Bjorhovde et al. (1972). Dwight and Ractliffe (1967), Young and Dwight (1971), and Dwight and Moxham (1977) used a simplified residual stress pattern in their studies, where the curved pattern was replaced with the rectangular stress blocks shown in Figure 6b. Due to the lower heat input typical of plasma cutting, tensile residual stress for plasma-cut edges are typically less than half of the material yield strength (Harris, 1997).

Most connection material is thermally cut, with grinding if required to remove imperfections. Residual stresses due to grinding are dependent on several factors, such as wheel speed, abrasive roughness, grinding direction, and use of coolant. In typical structural fabrication shops, hand-held angle grinders are used with no coolant, which creates tensile residual stresses due to uneven cooling (Harvey, 1985). Measurements by Blehaut et al. (2002) showed tension residual stresses at the ground surface between 20 and

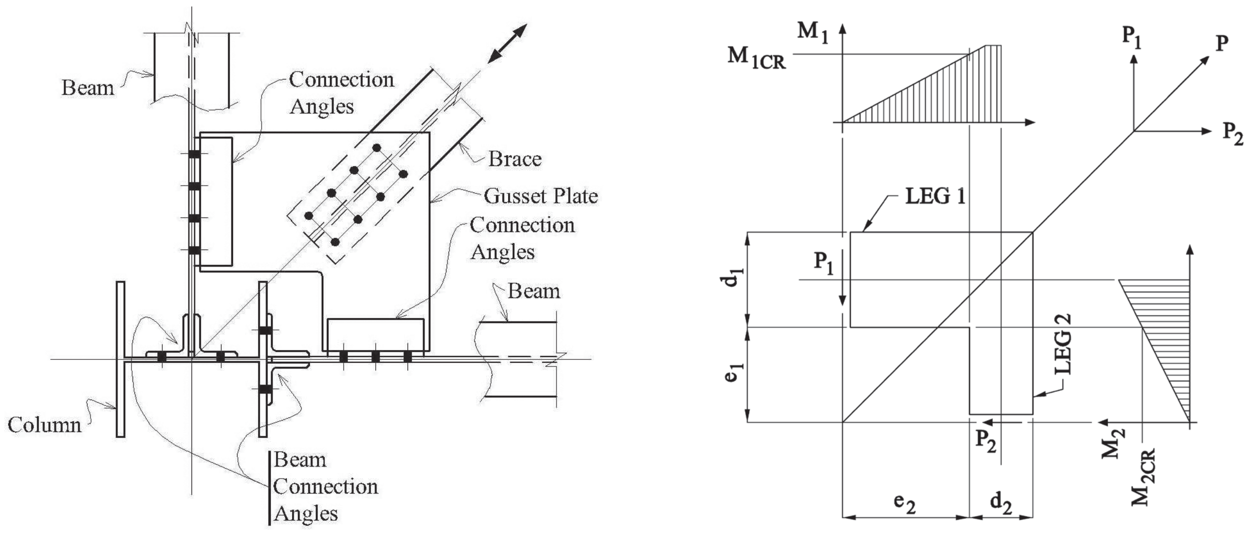

(a) *(b)*

Fig. 4. Wrap-around gusset plate: (a) wrap-around gusset plate; (b) load system.

64 ksi, with the lower values perpendicular to the grinding direction.

Through-thickness residual stress patterns can be determined from the two-dimensional mapping of measured residual stresses by Alpsten (1968) and Alpsten and Tall (1969). For bars and UM plates, the pattern in Figure 7a provides a reasonable fit to the data from Alpsten (1968). For flame-cut plates, the pattern in Figure 7b is based on the data from Alpsten and Tall (1969).

Because residual stresses must be in equilibrium across any plane, the through-thickness and across-width residual stresses are interdependent. Due to this, the through-thickness residual stress distribution varies along the plate width. Both the Alpsten (1968) specimens and the Alpsten and Tall (1969) specimens had small aspect ratios (between 7 and 8); therefore, both sets of data were affected by the residual stresses at the edge of the plate. A wide plate that would be more typical of a connection element is not likely to be significantly affected by the across-width residual stress pattern. In that case, the tension and compression residual stresses would need to balance for equilibrium across the thickness as shown in Figure 7c. The maximum experimental compression residual stress is estimated at 9 ksi.

The research by Alpsten (1968) and Alpsten and Tall (1969) used 2- and 3.5-in.-thick plates. For thinner plates, cooling occurs with a lower temperature gradient throughout the plate; therefore, the residual stresses in thinner plates are smaller. The simplified, linear approximation in Figure 7d will be used in the derivation of weak-axis flexural buckling strength of connection elements. The magnitude of both the tension and compression residual stresses are $0.25\sigma_y$, which is a conservative estimate based on the experimental results.

Residual stresses must be considered when assessing the inelastic buckling behavior of columns and beams. The column curve in AISC *Specification* Section E3 was developed using experimental results of rolled and welded I-shape members and box columns with various residual stress patterns. For doubly symmetric I-section members, the elastic-to-inelastic transition moment for lateral-torsional buckling in AISC *Specification* Section F2 is 70% of the yield moment. This implies a pattern with a compression residual stress of $0.3F_y$ at the flange tips, as shown in Figure 5a, which is a common pattern for elements with rolled edges. However, the different residual stress patterns created by the various fabrication processes brings uncertainty to the stability design of connection elements. Further complicating the stability design of connection elements, the buckling direction must be considered to determine whether the across-width residual stress pattern or the through-thickness pattern is applicable.

Kim and Chen (1996) and ASCE (1997) found that the AISC column curve can be closely estimated for I-shape members using a linear residual stress pattern across the flanges with a maximum compressive residual stress of $\sigma_{rc} = 0.30\sigma_y$ at the flange tips (Figure 5b). Because the residual stress pattern across the width of an I-shape flange

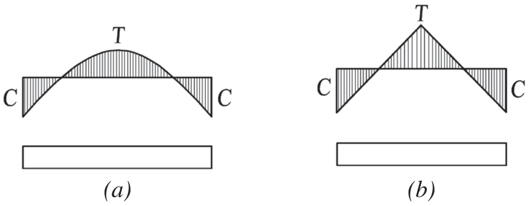

Fig. 5. Across-width residual stress pattern for bars and UM plates: (a) experimental; (b) simplified.

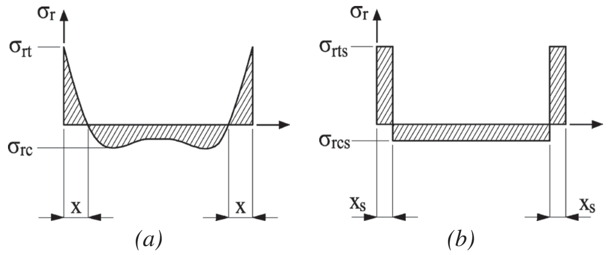

Fig. 6. Across-width residual stress pattern for plates with thermally cut edges: (a) experimental; (b) simplified.

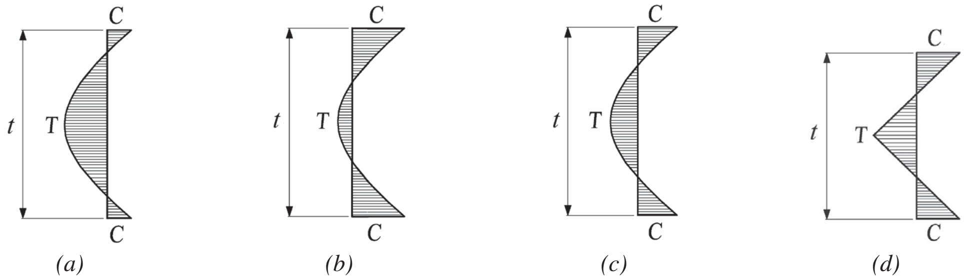

Fig. 7. Through-thickness residual stress patterns: (a) bars and UM plates; (b) flame-cut plates; (c) bars, UM plates, and flame-cut plates with large aspect ratios; (d) simplified.

is identical to that of a bar with rolled edges (Figure 5a), the strong-axis buckling behavior of a bar with rolled edges is similar to the weak-axis buckling behavior of an I-section. Therefore, for rectangular connection elements buckling about the strong axis, the effect of residual stresses is expected to be similar to that of I-shape columns. Thermally cut plates with tensile residual stress at the edges have improved buckling behavior. The stabilizing effect caused by tension residual stresses at the edges was demonstrated in the research of Bambach and Rasmussen (2002) and Rogers and Dwight (1977).

COMPRESSION STRENGTH

The flexural buckling provisions in AISC *Specification* Section E3 are reviewed, and a theoretical, tangent modulus solution is derived to analyze the differences in buckling behavior for connection elements and main members. The AISC column curve and the tangent modulus curve are compared to the available experimental results to determine their applicability to the design of connection elements.

AISC *Specification* Section J4.4

Provisions for strength of connecting elements in compression are in *Specification* Section J4.4. The available strength of connecting elements in compression for the limit states of yielding and buckling are determined as follows:

(a) When $KL/r \le 25$

$$P_n = F_y A_g \tag{1}$$

(b) When $KL/r > 25$, the provisions of Chapter E apply.

AISC *Specification* Section E3

Provisions for the flexural buckling strength of members in compression are in *Specification* Section E3. The nominal compressive strength is

$$P_n = F_{cr} A_g \tag{2}$$

The critical stress is determined as follows:

(a) When $\dfrac{KL}{r} \le 4.71\sqrt{\dfrac{E}{F_y}}$

$$F_{cr} = \left[0.658^{\left(\frac{F_y}{F_e}\right)}\right] F_y \tag{3}$$

(b) When $\dfrac{KL}{r} > 4.71\sqrt{\dfrac{E}{F_y}}$

$$F_{cr} = 0.877 F_e \tag{4}$$

where

$$F_e = \frac{\pi^2 E}{\left(\dfrac{KL}{r}\right)^2} \tag{5}$$

A_g = gross cross-sectional area, in.^{2}

E = modulus of elasticity, ksi

F_e = elastic buckling stress, ksi

F_y = specified minimum yield stress, ksi

K = effective length factor for flexural buckling

L = laterally unbraced length, in.

r = radius of gyration, in.

Theoretical Solutions

Using a tangent modulus approach, Galambos (1968) derived the weak-axis and strong-axis flexural buckling solutions for a rectangular column with the linear across-width residual stress pattern shown in Figure 5b. The maximum tension and compression residual stress was $0.5\sigma_y$, and the stiffness of all yielded material outside of the elastic core was neglected.

For most connection elements, the weak axis is critical for buckling, where the behavior is based on the through-thickness residual stress pattern. The tangent modulus approach from Galambos (1968) will be used to derive the buckling curve for weak-axis buckling of a plate with through-thickness residual stresses, $\sigma_{rt} = 0.25\sigma_y$ and $\sigma_{rc} = 0.25\sigma_y$. The linear approximation in Figure 7d will be used. The initial yielding condition is defined by Equation 6:

$$\sigma + \sigma_{rc} = \sigma_y \tag{6}$$

Using $\sigma_{rc} = 0.25\sigma_y$, the initial yielding stress ratio is

$$\sigma/\sigma_y = 0.75 \tag{7}$$

And the initial yielding load ratio is

$$P/P_y = 0.75 \tag{8}$$

When $P/P_y > 0.75$, the edges of the plate yield, leaving an elastic core of width, b, shown as the shaded portion in Figure 8a. Figure 8b shows the sectional stresses across the plate thickness, including the applied axial compression stress, σ, and the compression residual stress, σ_{rc}. The material behavior is defined by an elastic-perfectly plastic curve; therefore, the maximum stress on the cross-section is the material yield strength, σ_y. The elastic core is defined by a, where $b = 2\alpha t$ as shown in Figure 8b. From equilibrium of the cross section using the stress blocks in Figure 8b, the normalized load is

$$\frac{P}{P_y} = \frac{\sigma}{\sigma_y} + \frac{\sigma_{rc} - \sigma_{rt}}{2\sigma_y} - \left(\frac{\sigma + \sigma_{rc}}{\sigma_y} - 1\right)\left(\frac{1}{2} - \alpha\right) \tag{9}$$

Substitute $\sigma_{rt} = 0.25\sigma_y$ and $\sigma_{rc} = 0.25\sigma_y$ into Equation 9 to get Equation 10:

$$\frac{P}{P_y} = \frac{\sigma}{\sigma_y} - \left(\frac{\sigma}{\sigma_y} - \frac{3}{4}\right)\left(\frac{1}{2} - \alpha\right) \tag{10}$$

Using similar triangles for the stresses in Figure 8b,

$$\frac{\sigma + \sigma_{rc} - \sigma_y}{2} = \left(\sigma_{rt} + \sigma_{rc}\right)\left(\frac{1}{2} - \alpha\right) \tag{11}$$

Substitute $\sigma_{rt} = 0.25\sigma_y$ and $\sigma_{rc} = 0.25\sigma_y$ into Equation 11 to get Equation 12:

$$\frac{\sigma}{\sigma_y} = 1.25 - \alpha \tag{12}$$

Substitute Equation 12 into Equation 10 to get Equation 13:

$$\alpha = \sqrt{1 - \frac{P}{P_y}} \tag{13}$$

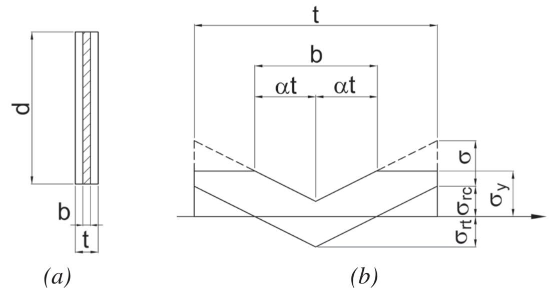

Fig. 8. Inelastic rectangular column with through-thickness residual stress pattern: (a) elastic core; (b) stresses.

The tangent modulus ratio of the cross-section is defined by τ:

$$\begin{aligned}\tau &= \frac{A_c}{A_g} \\ &= \frac{2\alpha td}{td} \\ &= 2\alpha \\ &= 2\sqrt{1 - \frac{P}{P_y}}\end{aligned} \tag{14}$$

The weak-axis moment of inertia of the plate is

$$I_y = \frac{dt^3}{12} \tag{15}$$

The weak-axis moment of inertia of the elastic core is

$$\begin{aligned}I_{yc} &= \frac{d\left(2\alpha t\right)^3}{12} \\ &= I_y \tau^3\end{aligned} \tag{16}$$

The slenderness parameter is

$$\lambda_y = \sqrt{\frac{I_{yc}/I_y}{P/P_y}} \tag{17}$$

Substituting Equation 16 into Equation 17:

$$\lambda_y = \sqrt{\frac{\tau^3}{P/P_y}} \tag{18}$$

Substituting Equation 14 into Equation 18, the slenderness parameter is given by Equation 19:

$$\lambda_y = \sqrt{\frac{8\left(1 - P/P_y\right)^{3/2}}{P/P_y}} \tag{19}$$

where

A_c = area of the elastic core, in.^{2}
P = axial load, kips
P_y = axial yield load, kips
$= A_g\sigma_y$
d = plate depth, in.
t = plate thickness, in.

σ = axial stress, ksi

σ_{rt} = tension residual stress, ksi

σ_{rc} = compression residual stress, ksi

σ_y = yield stress, ksi

The normalized load, P/P_y, versus the slenderness parameter, λ_y, for the tangent modulus solution with through-thickness residual stress is plotted in Figure 9. Because geometric imperfections are not accounted for, the tangent modulus solution follows the elastic critical load curve until $P/P_y > 0.75$. The column curve from AISC *Specification* Section E3 is also plotted. Except for very low slenderness values, the tangent modulus curve is above the AISC curve.

The tangent modulus solution for the weak-axis buckling of bars and UM plates with rolled edges can be solved using the across-width residual stress pattern of Figure 6b, with $\sigma_{rt} = 0.30\sigma_y$ and $\sigma_{rc} = 0.30\sigma_y$. The initial yielding condition is defined by Equation 6 with $\sigma_{rc} = 0.30\sigma_y$. The initial yielding load ratio is

$$P/P_y = 0.70 \tag{20}$$

When $P/P_y > 0.70$, the edges of the plate yield, leaving an elastic core of depth, h, shown as the shaded portion in Figure 10a. The elastic core is defined by the parameter, α, where $h = 2\alpha d$. Using the stresses in Figure 10b, the normalized load is

$$\frac{P}{P_y} = \frac{\sigma}{\sigma_y} + \frac{\sigma_{rc} - \sigma_{rt}}{2\,\sigma_y} - \left(\frac{\sigma + \sigma_{rc}}{\sigma_y} - 1\right)\left(\frac{1}{2} - \alpha\right) \tag{21}$$

Substitute $\sigma_{rt} = 0.30\sigma_y$ and $\sigma_{rc} = 0.30\sigma_y$ into Equation 21 to get Equation 22:

$$\frac{P}{P_y} = \frac{\sigma}{\sigma_y} - \left(\frac{\sigma}{\sigma_y} - 0.70\right)\left(\frac{1}{2} - \sigma\right) \tag{22}$$

Using similar triangles for the stresses in Figure 10b,

$$\frac{\sigma + \sigma_{rc} - \sigma_y}{2} = (\sigma_{rt} + \sigma_{rc})\left(\frac{1}{2} - \alpha\right) \tag{23}$$

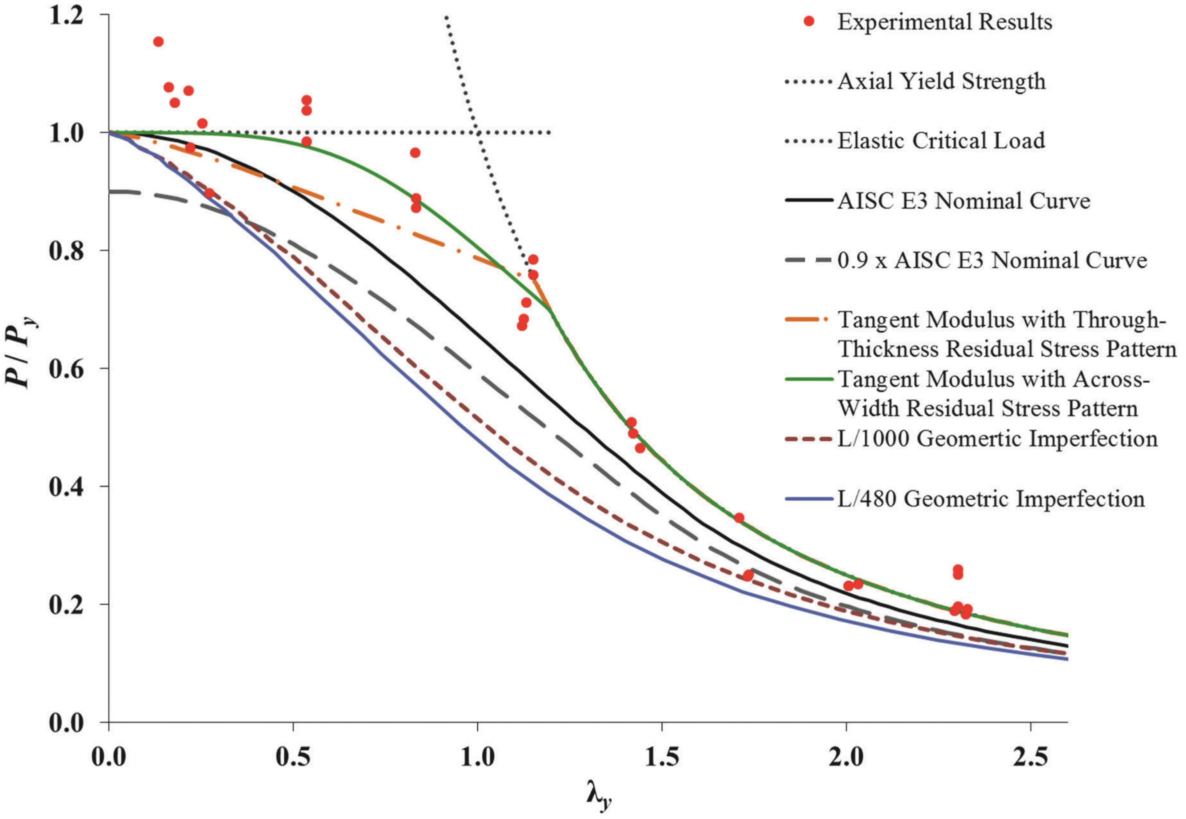

Fig. 9. Column curves for AISC Specification and theoretical solutions.

Substitute $\sigma_{rt} = 0.30\sigma_y$ and $\sigma_{rc} = 0.30\sigma_y$ into Equation 23 to get Equation 24:

$$\frac{\sigma}{\sigma_y} = 1.3 - 1.2\alpha \tag{24}$$

Substitute Equation 24 is into Equation 22 to get Equation 25:

$$\alpha = 0.913\sqrt{1 - \frac{P}{P_y}} \tag{25}$$

The tangent modulus of the cross-section is defined by τ:

$$\begin{aligned} \tau &= \frac{A_c}{A_g} \\ &= \frac{2\alpha td}{td} \\ &= 2\alpha \\ &= 1.83\sqrt{1 - \frac{P}{P_y}} \end{aligned} \tag{26}$$

The weak-axis moment of inertia of the plate is

$$I_y = \frac{dt^3}{12} \tag{27}$$

The weak-axis moment of inertia of the elastic core is

$$\begin{aligned} I_{ye} &= \frac{(2\alpha d)t^3}{12} \\ &= I_y\tau \end{aligned} \tag{28}$$

The slenderness parameter is

$$\lambda_y = \sqrt{\frac{I_{ye}/I_y}{P/P_y}} \tag{29}$$

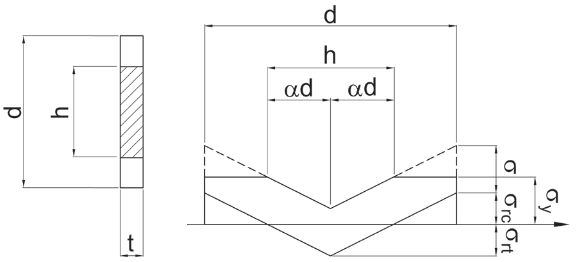

(a) (b)

Fig. 10. Inelastic rectangular column with across-width residual stress pattern: (a) elastic core; (b) stresses.

Substituting Equation 28 into Equation 29 results in Equation 30:

$$\lambda_y = \sqrt{\frac{\tau}{P/P_y}} \tag{30}$$

Substituting Equation 26 into Equation 30, the slenderness parameter is given by Equation 31:

$$\lambda_y = 1.35\sqrt{\frac{\left(1 - P/P_y\right)^{1/2}}{P/P_y}} \tag{31}$$

The normalized load, P/P_y, versus the slenderness parameter, λ_y, for the tangent modulus solution with an across-width residual stress pattern is plotted in Figure 9. Because geometric imperfections are not accounted for, the tangent modulus solution follows the elastic critical load curve until $P/P_y > 0.70$. The tangent modulus curve is above the AISC curve for the full slenderness range.

The tangent modulus curves do not account for the initial out-of-flatness of the plate. Because the initial deformations have a negative influence on the behavior, they must be considered in the design method. A lower-bound curve for buckling of rectangular members with an initial out-of-straightness can be determined using a beam-column approach. The moment-thrust-curvature relationships by Galambos (1968) described further in the "Combined Loads" section of this paper were solved for the cases of initial mid-height out-of-straightness values of $\delta_0 = L/1{,}000$ and $\delta_0 = L/480$. The first-order moment, at the mid-height of the column is

$$M_1 = P\delta_0 \tag{32}$$

The second-order moment is

$$M_2 = \frac{M_1}{1 - \frac{P}{P_e}} \tag{33}$$

where

M_1 = first-order moment, kip-in.

M_2 = second-order moment, kip-in.

P_e = elastic critical load, kips

δ_0 = initial mid-height out-of-straightness, in.

The normalized load, P/P_y, versus the slenderness parameter, λ_y, for the moment-thrust-curvature solution by Galambos (1968) is plotted in Figure 9. The slenderness parameter is

$$\lambda_y = \frac{KL}{\pi r}\sqrt{\frac{\sigma_y}{E}} \tag{34}$$

For both out-of-straightness values, the curves are plotted in Figure 9. Both curves are similar in shape to the AISC curve; however, the theoretical solutions are well below the AISC curve for the full slenderness range. Because the derivation neglects the stiffness of all material outside the elastic core, the theoretical solution is expected to be conservative.

Experimental Comparisons

Also plotted in Figure 9 are 39 experimental results from the research projects of Seely and Putnam (1919), Haaijer (1953) and Robinson (1983), who tested small-scale solid rectangular mild steel specimens in axial compression. All of the specimens failed by flexural buckling, and the end conditions were accounted for in the calculation of the slenderness parameter, λ_y, according to Equation 34. The results are plotted as the normalized experimental load, P_t/P_y, versus the slenderness parameter. Compared to the nominal strength from AISC *Specification* Section E3, the average experimental-to-nominal load is 1.15 and the standard deviation is 0.226.

Design Recommendations

By comparing the AISC column curve to the experimental results and theoretical solutions, it can be concluded that rectangular members with proportions similar to connection elements can be designed using the flexural buckling provisions in AISC *Specification* Section E3. The resistance factor, $\phi = 0.90$, specified in Section E1 has traditionally been used to design connection elements and is adequate for isolated compression members. However, for connection elements such as the corner gusset plate shown in Figure 1, the definition of the effective width, buckling length, and effective length factor must be considered when determining the resistance factor. For example, the effective length factors proposed for gusset plate design by Dowswell (2006) were calibrated for use with $\phi = 0.90$, but Dowswell (2014) recommended using $\phi = 0.75$ to design gusset plates with a new design method with variable effective width trajectory angles.

FLEXURAL STRENGTH

The lateral-torsional buckling provisions in AISC *Specification* Section F11 are reviewed, and a theoretical, tangent modulus solution is developed to analyze the differences between connection elements and main members. Both methods are compared to the available experimental results to determine their applicability to the design of connection elements.

AISC *Specification* Section J4.5

Provisions for the strength of connecting elements in flexure are in *Specification* Section J4.5, which contains a general statement requiring the following limit states to be checked: flexural yielding, local buckling, lateral-torsional buckling, and flexural rupture. Flexural yielding and lateral-torsional buckling of rectangular connection elements can be checked using *Specification* Section F11.

For typical member design, the cross-section is made up of two or more elements; therefore, local buckling and lateral-torsional buckling are two distinct limit states. However, rectangular connection elements in flexure have a buckled shape that closely resembles lateral-torsional buckling, with lateral deformation and twisting of the cross-section. Because rectangular beams are single-element cross-sections, the local buckling limit state is not applicable.

AISC *Specification* Section F11

Provisions for the flexural strength and stability of rectangular members bent about their major axis are in *Specification* Section F11. The nominal flexural strength is

For yielding, $\frac{L_b d}{t^2} \le \frac{0.08E}{F_y}$

$$M_n = M_p = F_y Z_x \le 1.6M_y \tag{35}$$

For inelastic lateral-torsional buckling, $\frac{0.08E}{F_y} < \frac{L_b d}{t^2} \le \frac{1.9E}{F_y}$

$$M_n = C_b\left[1.52 - 0.274\left(\frac{L_b d}{t^2}\right)\frac{F_y}{E}\right]M_y \le M_p \tag{36}$$

For elastic lateral-torsional buckling, $\frac{L_b d}{t^2} > \frac{1.9E}{F_y}$

$$M_n = F_{cr} S_x \le M_p \tag{37}$$

The critical stress is

$$F_{cr} = \frac{1.9EC_b}{\frac{L_b d}{t^2}} \tag{38}$$

where

C_b = lateral-torsional buckling modification factor

E = modulus of elasticity, ksi

F_y = specified minimum yield strength, ksi

L_b = distance between brace points, in.

M_n = nominal moment, kip-in.

M_y = yield moment, kip-in.

M_p = plastic moment, kip-in.

S_x = strong-axis elastic section modulus, in.^{3}

Z_x = strong-axis plastic modulus, in.^{3}

d = beam depth, in.

t = beam width, in.

Equation 38 is the theoretical solution for the elastic critical buckling stress multiplied by C_b and simplified by substituting the properties for a rectangular cross section. It can be derived from the critical moment for a rectangular beam with equal end moments (Timoshenko and Gere, 1961):

$$M_e = \frac{\pi}{L_b}\sqrt{EI_yGJ} \tag{39}$$

where

G = shear modulus of elasticity, ksi

I_y = weak-axis moment of inertia, in.^{4}

J = torsional constant, in.^{4}

M_e = elastic critical moment, kip-in.

The critical stress is

$$F_{cr} = \frac{M_e}{S_x} \tag{40}$$

The strong-axis section modulus is

$$S_x = \frac{td^2}{6} \tag{41}$$

The weak-axis moment of inertia is

$$I_y = \frac{dt^3}{12} \tag{42}$$

The torsional constant is

$$J = \frac{dt^3}{3} \tag{43}$$

The shear modulus of elasticity is

$$G = 0.385E \tag{44}$$

Substitute Equations 42, 43 and 44 into Equation 39 and then substitute Equations 39 and 41 into Equation 40 to get

$$F_{cr} = \frac{1.95Et^2}{L_bd} \tag{45}$$

Round the constant 1.95 down to 1.9 and multiply by C_b to account for nonuniform moment to get Equation 38.

Theoretical Solutions

For cantilever beams, the inelasticity is concentrated at the fixed end of the beam, which is the location of least deformation during lateral-torsional buckling. Therefore, material inelasticity has less of a detrimental effect on cantilever beams than simply supported beams. Chakrabarti (2000) solved the differential equations for stability of a rectangular cantilever beam with a concentrated load at the free end. He determined that the beam can be considered elastic when the slenderness parameter, λ, exceeds 1.31, where λ is calculated with Equation 46. This is less conservative than AISC *Specification* Section F11, where elastic buckling is assumed for λ greater than 1.9.

$$\lambda = \frac{L_bdF_y}{Et^2} \tag{46}$$

Galambos (1968) and Galambos and Surovek (2008) derived the tangent modulus solution for inelastic lateral-torsional buckling of a rectangular beam, using only the resistance of the elastic core as shown in Figure 11. The inelastic parts of the cross section were assumed to have no torsional stiffness or weak-axis flexural stiffness. However, Neal (1950) showed, both theoretically and experimentally, that the torsional rigidity remains at the elastic value after a beam has yielded in the presence of a strong-axis moment. It was also shown that the extent of yielding has no influence on the torsional rigidity. An independent theoretical derivation by Wittrick (1952) verified Neal's conclusions. A numerical analysis by Hartmann (1971), based on the tangent modulus concept, was in agreement with the results of Neal (1950).

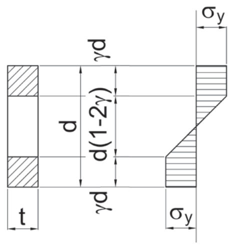

Fig. 11. Elastic core of an inelastic rectangular beam.

A new tangent modulus solution is derived here, which assumes the torsional rigidity remains at the elastic value after flexural yielding. As in the Galambos and Surovek (2008) and Neal (1950) solutions, geometric imperfections and residual stresses are neglected. The plastic moment of a rectangular cross section is

$$M_p = \frac{F_y t d^2}{4} \tag{47}$$

The weak-axis moment of inertia of the elastic core is

$$I_{yc} = \frac{t^3 d(1-2\gamma)}{12} \tag{48}$$

Substitute the sectional and material properties of Equations 43, 44 and 48 into Equation 39 to get the critical load

$$M_{cr} = \frac{0.325 E t^3 d}{L_b}\sqrt{1-2\gamma} \tag{49}$$

Divide by M_p from Equation 47 and substitute λ from Equation 46:

$$\frac{M_{cr}}{M_p} = \frac{1.30}{\lambda}\sqrt{1-2\gamma} \tag{50}$$

The depth of the yielded portion of the cross section is calculated based on the strength of the stress blocks:

$$\gamma = \frac{1}{2}\left(1-\sqrt{3-3\frac{M_{cr}}{M_p}}\right) \tag{51}$$

Substitute Equation 51 into Equation 50 to get the critical moment ratio:

$$\frac{M_{cr}}{M_p} = \frac{1.71}{\lambda}\left(1-\frac{M_{cr}}{M_p}\right)^{1/4} \tag{52}$$

Buckling is defined by the elastic critical load when $\lambda = 1.95$. This is where $M_{cr}/M_p = \tfrac{2}{3}$, which is the S_x/Z_x ratio. The normalized moment, M_{cr}/M_p, versus the slenderness parameter, λ, for the Galambos (1968) solution and the simplified Neal solution (Equation 52) is plotted in Figure 12. The simplified Neal curve is above the Galambos curve over the entire inelastic range, showing the effect of assuming the elastic

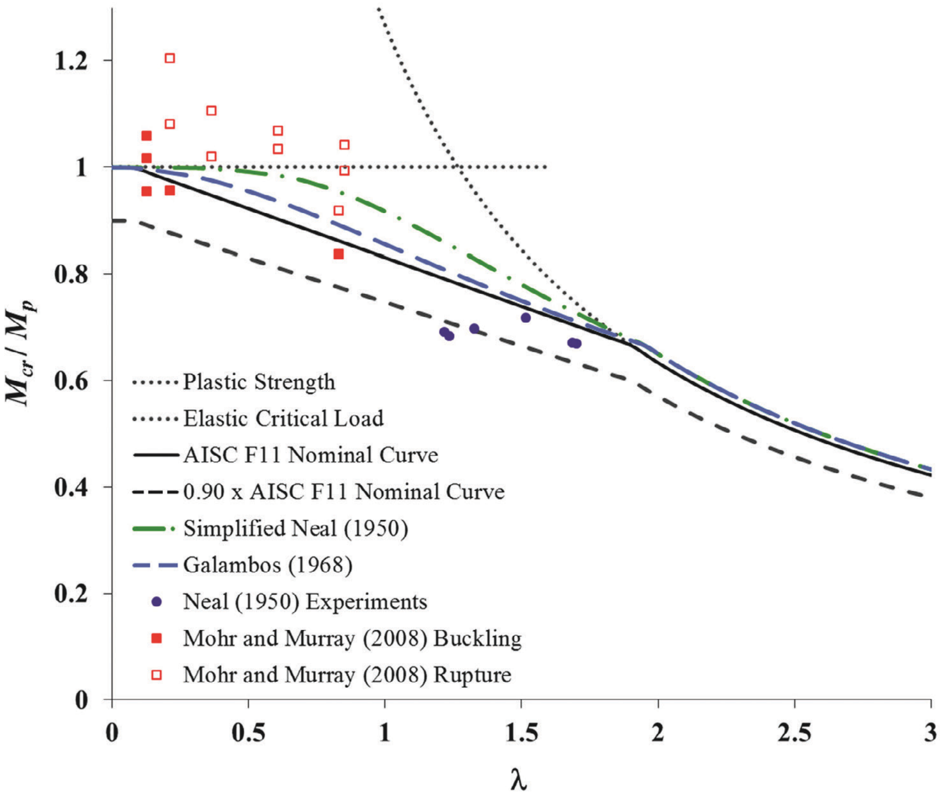

Fig. 12. Lateral-torsional buckling curves for AISC Specification and theoretical solutions.

torsional rigidity is unaffected by flexural yielding. The AISC curve consistently falls below the theoretical curves.

Experimental Comparisons

The normalized experimental moments for specimens tested by Neal (1950) and Mohr and Murray (2008) are plotted against the slenderness parameter in Figure 12. The tests by Neal were small-scale, simply supported beams with a width-to-depth ratio of 8. The results are indicated by the solid circles. The Mohr and Murray (2008) specimens were full-scale, beam web splice plates subjected to uniform moment. All six specimens by Neal (1950) and three of the five specimens by Mohr and Murray (2008) that failed by excessive deformation were below the AISC *Specification* Section F11 nominal curve. This is believed to be primarily due to the effect of geometric imperfections. For these 11 specimens, the average experimental-to-nominal load is 0.958 and the standard deviation is 0.0571.

Design Recommendations

By comparing the AISC flexural strength curve to the experimental results and theoretical solutions, it has been concluded that rectangular connection elements can be designed using the lateral-torsional buckling provisions in AISC *Specification* Section F11. The resistance factor, $\phi = 0.90$, specified in Section F1, should be analyzed using further test results. Based on the limited experimental results available, with two of the specimens buckling below the available moment resistance, it appears that a lower value may be needed in some cases with uniform moment. However, this may not be justified for connection elements with a moment gradient along the length. In this case, the slightly conservative nature of Equation F1-1 in the AISC *Specification* will partially offset the need for a lower resistance factor. Also, $\phi = 0.90$ may be adequate for specific connection elements where the C_b factor is calibrated using experimental or finite element results to provide the required safety index.

COMBINED LOADS

The combined loading provisions in AISC *Specification* Sections H1 and H2 are reviewed and compared to approximate theoretical solutions for rectangular members derived by Vlasov (1961), Galambos (1968) and Tomas et al. (2013), as well as to an empirical curve-fit equation proposed by Pisarenko and Mullagulov (1998). Based on these comparisons, design provisions for the buckling strength of connection elements under combined loading are recommended.

AISC *Specification* Section H1

Provisions for the load interaction of doubly symmetric members under combined flexure and compression are in *Specification* Section H1.1.

When $P_r/P_c \geq 0.2$

$$\frac{P_r}{P_c}+\frac{8}{9}\left(\frac{M_{rx}}{M_{cx}}+\frac{M_{ry}}{M_{cy}}\right)\leq 1.0 \tag{53}$$

When $P_r/P_c < 0.2$

$$\frac{P_r}{2P_c}+\frac{M_{rx}}{M_{cx}}+\frac{M_{ry}}{M_{cy}}\leq 1.0 \tag{54}$$

where

M_{cx} = available flexural strength about the strong axis, kip-in.

M_{cy} = available flexural strength about the weak axis, kip-in.

M_{rx} = required flexural strength about the strong axis, kip-in.

M_{ry} = required flexural strength about the weak axis, kip-in.

P_c = available axial strength, kips

P_r = required axial strength, kips

Specification Section H1.2 is for members under combined flexure and tension. The equations in Section H1 are used with an increase in the lateral-torsional buckling modification factor according to Equation 55.

$$C_b' = C_b\sqrt{1+\frac{\alpha P_r}{P_{ey}}} \tag{55}$$

where

$$P_{ey} = \frac{\pi^2 EI_y}{L_b^2} \tag{56}$$

$\alpha = 1.0$ (LRFD); $\alpha = 1.6$ (ASD)

AISC *Specification* Section H2

AISC *Specification* Section H2 provides a linear stress interaction equation that can be used for all shapes. The equation is presented in terms of stress ratios; however, for doubly symmetric members, it can be expressed using load ratios as in Equation 57:

$$\frac{P_r}{P_c}+\frac{M_{rx}}{M_{cx}}+\frac{M_{ry}}{M_{cy}}\leq 1.0 \tag{57}$$

AISC *Specification* Appendix 8

The required moments used in the interaction equations in Sections H1 and H2 are second-order moments, which can be calculated using amplified first-order moments with equations similar to those in AISC *Specification* Appendix 8:

$$M_r = BM_1 \tag{58}$$

$$B=\frac{1}{1-\alpha P_r/P_e} \tag{59}$$

The elastic critical load about the bending axis is

$$P_e=\frac{\pi^2 EI}{(KL)^2} \tag{60}$$

where

B = moment amplification multiplier

M_1 = first-order moment, kip-in.

M_r = required flexural strength, kip-in.

I = moment of inertia about the bending axis, in.^{4}

Plastic Interaction

At low slenderness ratios ($\lambda_y \approx 0$), stability is not a concern, and a plastic interaction curve is applicable. For axial loading plus biaxial flexure, the equation recommended by Dowswell (2015) is

$$\left(\frac{P_r}{P_y}\right)^2+\left[\left(\frac{M_{rx}}{M_{px}}\right)^{1.7}+\left(\frac{M_{rz}}{M_{pz}}\right)^{1.7}\right]^{0.59}=1.0 \tag{61}$$

For single-axis flexure, Equation 61 reduces to

$$\left(\frac{P_r}{P_y}\right)^2+\frac{M_r}{M_p}=1.0 \tag{62}$$

Effect of Single-Axis Flexure on Axial Compression Strength

Galambos (1968) derived an approximate solution for single-axis flexure–compression interaction using inelastic moment-thrust-curvature relationships of a rectangular member. The solution accounted for instability due to flexural buckling, but not lateral-torsional buckling. The axial-moment interaction curve is defined as follows.

When $\frac{P_r}{P_y}+\left(\frac{P_r}{P_e}\right)^{1/3}>1$

$$\frac{M_r}{M_p}=2\left(1-\frac{P_r}{P_y}\right)\left[1-\left(\frac{P_r}{P_e}\right)^{1/3}\right] \tag{63}$$

When $\frac{P_r}{P_y}+\left(\frac{P_r}{P_e}\right)^{1/3}\leq 1$

$$\frac{M_r}{M_p}=1-\left(\frac{P_r}{P_y}\right)^2-\left(\frac{P_r}{P_e}\right)^{2/3} \tag{64}$$

where

P_y = axial yield load, kips

$= A_g\sigma_y$

At very low slenderness ratios, $P_r/P_e \approx 0$, Equation 64 reduces to Equation 62. In Figure 13, three interaction curves are plotted for elements with a slenderness ratio of zero ($\lambda_y = 0$). These curves are defined by AISC *Specification* Section H1, AISC *Specification* Section H2, and Galambos (1968). Both of the AISC curves are well below the Galambos curve for the full loading range; however, *Specification* Section J4.4 allows the axial yield strength to be used for connecting elements in compression when $KL/r \leq 25$. The Galambos curve is also plotted for $\lambda_y = 1/3$, which was selected based on $KL/r = 25$ for $F_y = 50$ ksi (at $F_y = 36$ ksi, $KL/r = 29$). It can be readily observed that the AISC *Specification* Section H1 curve for $\lambda_y = 0$ matches well with the Galambos curve for $\lambda_y = 1/3$.

The change in shape of the interaction curve with increasing λ_y is apparent in Figure 14, which shows the interaction curves for three slenderness values: $\lambda_y = 0.5$, 1.5 and 2.5. The Galambos curves are above the AISC H1 curves for most loading ranges and slenderness values; however, at high slenderness values and high moment ratios, they drop below the AISC H1 curves.

Interaction of Lateral-Torsional Buckling and Flexural Buckling

Vlasov (1961) solved the approximate differential equations for a narrow rectangular member under the action of an eccentric axial compression force applied at each end of a simply supported member. The member was restrained against torsional rotation at the ends but was free to warp. The assumed weak-axis buckled shape was a half sine wave.

The elastic critical buckling load is

$$P_{el} = \frac{P_{ey} + P_{ez}}{2H}\left[1 - \sqrt{1 - \frac{4P_{ey}P_{ez}H}{\left(P_{ey} + P_{ez}\right)^2}}\right] \tag{65}$$

The weak-axis buckling load is

$$P_{ey} = \frac{\pi^2 EI_y}{(KL)_y^2} = \frac{\pi^2 EA_g}{\left(\frac{KL}{r}\right)_y^2} \tag{66}$$

The torsional buckling load is

$$P_{ez} = \frac{GJ}{r_o^2} \tag{67}$$

where

$$H = 1 - \left(\frac{e_y}{r_x}\right)^2 \tag{68}$$

$$r_o^2 = \frac{I_x + I_y}{A_g} = \frac{t^2 + d^2}{12} \tag{69}$$

where

e_y = eccentricity in the y-direction, inducing strong-axis flexure, in.

r_x = strong-axis radius of gyration, in.

Pisarenko and Mullagulov (1998) developed an elliptical interaction equation (Equation 70) using experimental results of small-scale rectangular members under combined flexure and axial compression:

$$\left(\frac{M_r}{M_e}\right)^2 + \left(\frac{P_r}{P_{ey}}\right)^2 = 1 \tag{70}$$

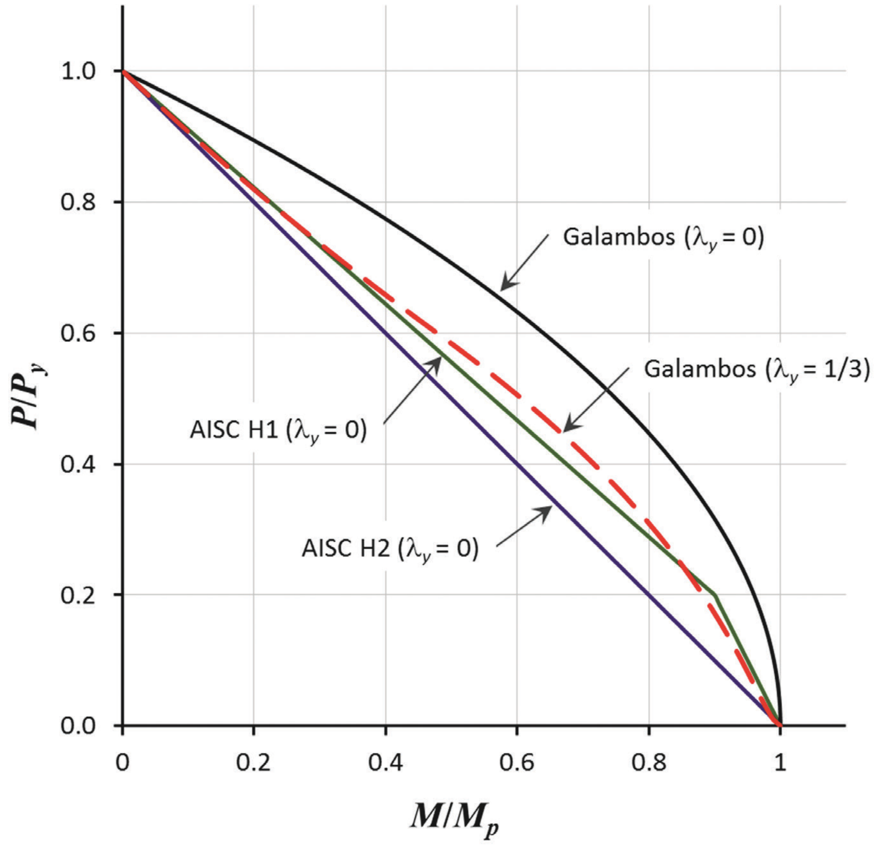

Fig. 13. Interaction curves for single-axis flexure and axial compression at low slenderness.

The elliptical and the AISC interaction equations are compared to Vlasov's (1961) solution in Figure 15. For members sized with typical beam proportions, with $L_b/d \geq 4$, elliptical interaction according to Equation 70 is conservative over most of the axial load range, with a slight nonconservatism at very high axial load ratios. The AISC interaction equations are conservative over the entire loading range. For lower length-to-depth ratios typical of connection elements, where $L_b/d \leq 2$, Equation 70 is nonconservative over much of the axial load range. Therefore, for connection elements, the AISC interaction equations are more appropriate at high axial load ratios. A more accurate solution is given by Equation 71, which is a second-order polynomial curve fit to the Vlasov (1961) solution for $L_b/d = 1$. The curve fit equation provides a good fit to the Vlasov curve, with $R^2 = 0.991$; however, the linear approximation of the Vlasov (1961) solution given by Equation 72 may be more appropriate for design purposes:

$$\frac{P}{P_{ey}} = 1 - 0.95\frac{M}{M_e} + 0.46\left(\frac{M}{M_e}\right)^2 \tag{71}$$

$$\frac{P}{P_{ey}} + 0.65\frac{M}{M_e} = 1.0 \tag{72}$$

Effect of Axial Tension on Lateral-Torsional Buckling

Tomas et al. (2013) showed that the critical buckling moment increases with the axial tension according to Equation 73:

$$M_e' = M_e\sqrt{\left(1 + \frac{P_r}{P_{ey}}\right)\left(1 + \frac{P_r}{P_{ez}}\right)} \tag{73}$$

By comparing Equation 73 to Equation 55, it can be observed that the AISC *Specification* equation neglects the effect of the second term under the radical in Equation 73. Numerical comparisons between the two equations showed that for rectangular members with an L/d ratio of 2 or greater, the maximum increase in critical moment due to the additional term is only 7%.

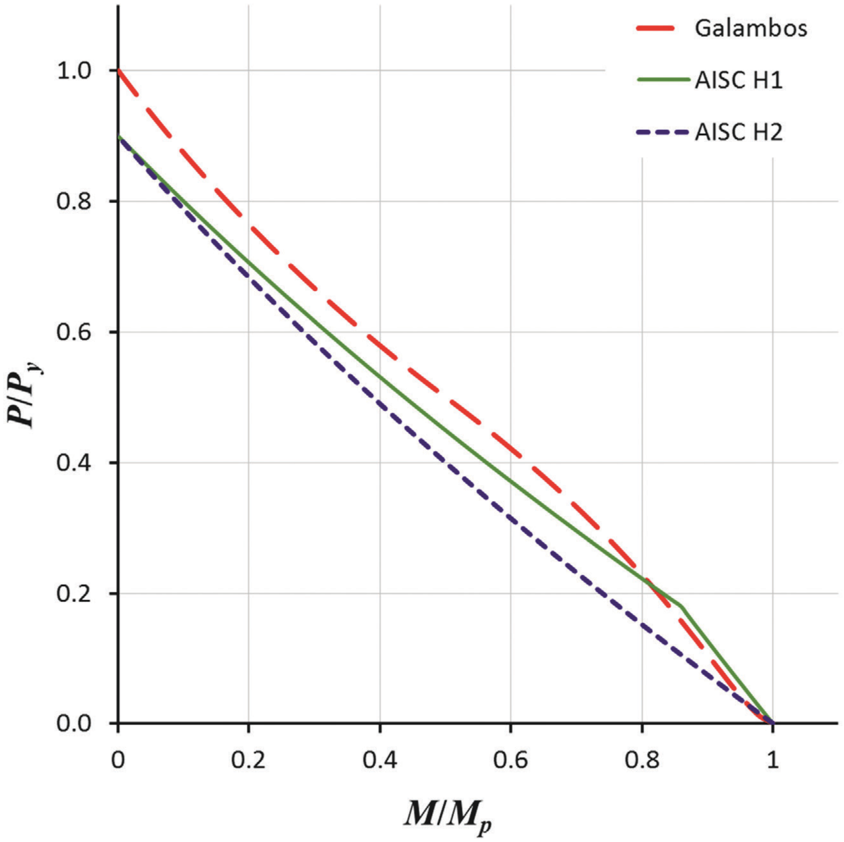

$\lambda_y = 0.5$

Fig. 14a. Interaction curves for single-axis flexure and axial compression at high slenderness.

Design Recommendations

By comparing the AISC load interaction curves to the theoretical solutions, it was concluded that rectangular connection elements can be designed using the following slenderness zones:

- When $\lambda_y \le 0.12$ ($KL/r \le 9.1$ for $F_y = 50$ ksi) and $M_n = M_p$, the effects of stability can be neglected and plastic interaction according to Equation 62 is applicable. This gives a maximum nonconservative error of 5%.
- When $0.12 < \lambda_y \le 0.33$ ($KL/r \le 25$ for $F_y = 50$ ksi) and $M_n = M_p$, the effects of stability can be neglected and the equations in AISC *Specification* Section H1.1 are applicable.
- When $0.33 < \lambda_y$ ($KL/r > 25$ for 50 ksi) or $M_n < M_p$, the effects of stability must be included in the design and the interaction equation in AISC *Specification* Section H2 is applicable.

For cases with combined axial tension and lateral-torsional buckling, the increased buckling resistance can be calculated with Equation 55, which is from AISC *Specification* Section H1.2. Because connection elements are often subjected to high shear demands at the same location as the maximum axial and flexural demands, an additional plastic interaction calculation may be required to determine the strength of the connection element.

CONCLUSIONS

Various factors affecting the stability of connection elements were discussed, with an emphasis on the differences between main members and connection elements. The main differences affecting the buckling strength of connection elements are smaller length-to-depth ratios, unpredictable stress distributions, ambiguous boundary conditions, different residual stress patterns, and large out-of-flatness tolerances.

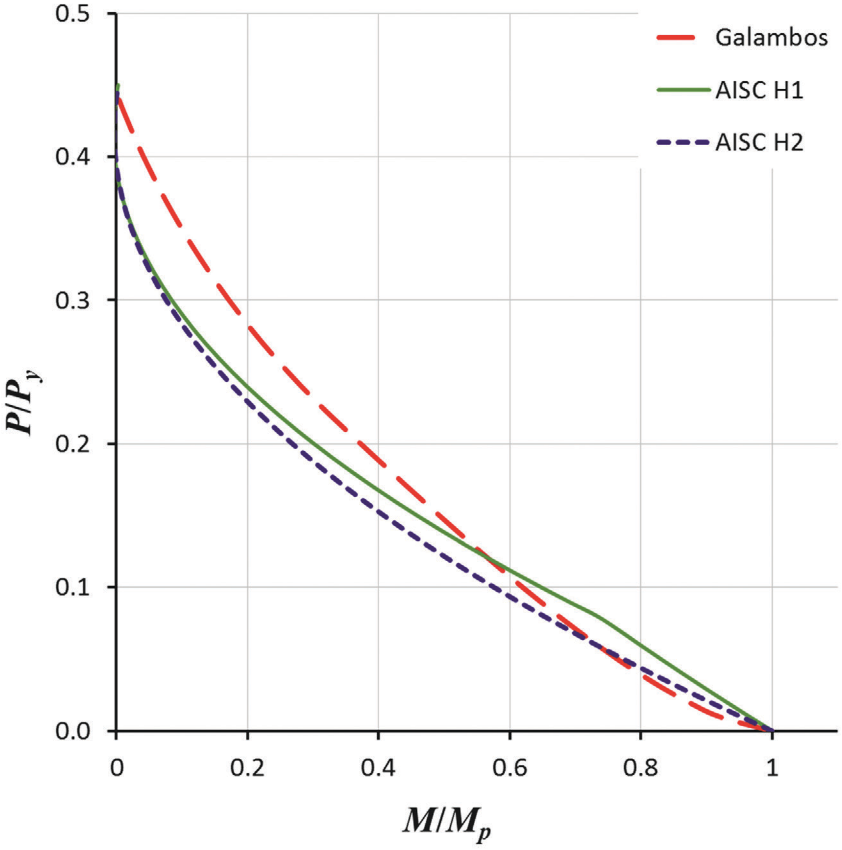

$\lambda_y = 1.5$

Fig. 14b. Interaction curves for single-axis flexure and axial compression at high slenderness.

A new column curve was derived, based on the tangent modulus approach, for flexural buckling of a plate with a through-thickness residual stress pattern typical of a connection element. The available data on stability of connection elements was compared to the flexural buckling, lateral-torsional buckling, and combined loading provisions in the AISC *Specification*. Based on these comparisons, practical design guidelines were recommended for the flexural buckling and lateral-torsional buckling of connection elements. It was found that rectangular connection elements can be designed using the flexural buckling provisions in AISC *Specification* Section E3 and the lateral-torsional buckling provisions in AISC *Specification* Section F11.

For combined axial-flexural loading of connection elements, it was shown that the shape of the interaction curve is dependent on the slenderness parameter, λ_y. Three slenderness zones were recommended. At low slenderness ($\lambda_y \leq 0.12$), the strength can be calculated using a plastic interaction curve. The strength of connection elements with high slenderness ($0.33 < \lambda_y$) is best predicted with AISC *Specification* Section H2. At intermediate slenderness ($0.12 < \lambda_y \leq 0.33$), the effects of stability can be neglected and the interaction equations in AISC *Specification* Section H1.1 are applicable. For cases with combined axial tension and lateral-torsional buckling, the increased buckling resistance can be calculated with the equation in AISC *Specification* Section H1.2.

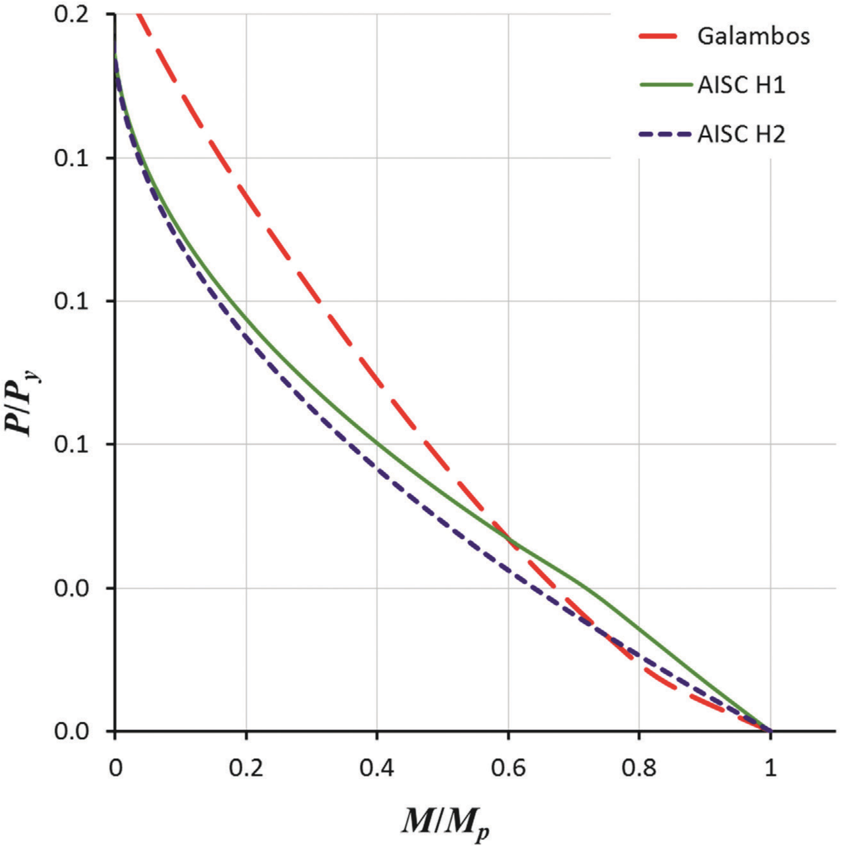

$\lambda_y = 2.5$

Fig. 14c. Interaction curves for single-axis flexure and axial compression at high slenderness.

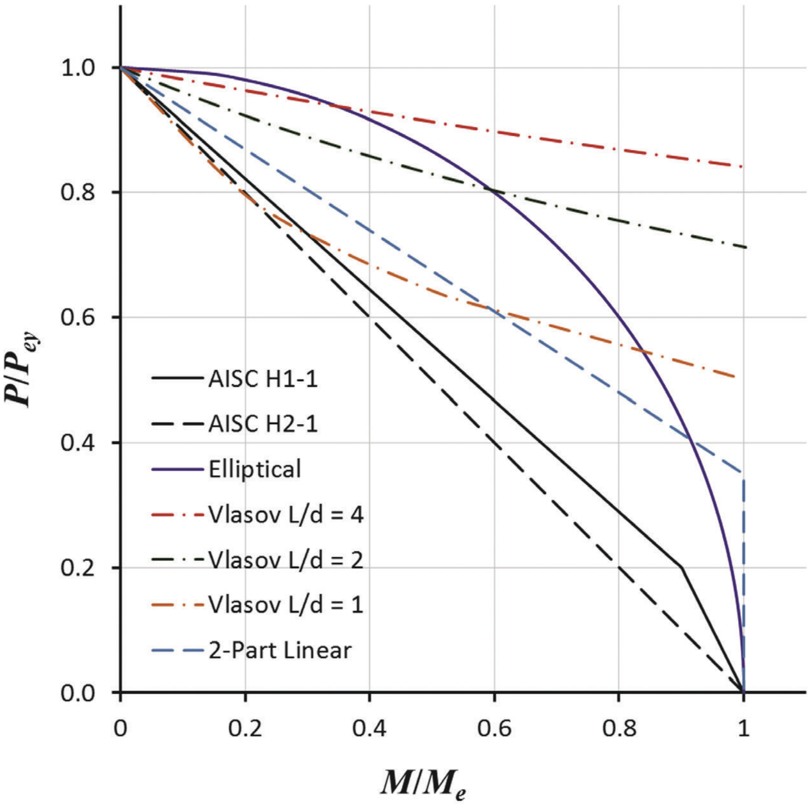

Fig. 15. Interaction curves for lateral-torsional buckling and flexural buckling.

DESIGN EXAMPLES

Coped Beam Example 1

In this example, the cope buckling strength will be calculated for a double-coped W18×50 beam subjected to shear and axial compression. The cope is 4½ in. long × 1½ in. deep at both flanges as shown in Figure 16. The beam material is ASTM A992, and the beam is braced laterally by a floor slab at the face of the top-flange cope.

ASTM A992: $F_y = 50$ ksi

W18×50: $t_w = 0.355$ in. $d = 18.0$ in.

Cope length: $c = c_t = c_b = 4\frac{1}{2}$ in.

Cope depth: $d_c = d_{ct} = d_{cb} = 1\frac{1}{2}$ in.

Distance from the face of the cope to the end reaction: $e = 4\frac{1}{2}$ in.

Reduced depth of web, $h_o = 18.0 \text{ in.} - (2)(1\frac{1}{2} \text{ in.}) = 15.0$ in.

The vertical and horizontal reactions are:

LRFD	ASD
$R_u = 90$ kips $F_{tu} = 120$ kips	$R_a = 60$ kips $F_{ta} = 80$ kips

The moment at the face of the cope is $M = Re$:

LRFD	ASD
$M_u = R_u e$ $= (90 \text{ kip})(4\frac{1}{2} \text{ in.})$ $= 405$ kip-in.	$M_u = R_u e$ $= (60 \text{ kip})(4\frac{1}{2} \text{ in.})$ $= 270$ kip-in.

Flexural Strength

From Dowswell and Whyte (2014), for beams with equal cope lengths at the top and bottom flange, C_b is

$$\begin{aligned} C_b &= \left[3 + \ln\left(\frac{L_b}{d}\right)\right]\left(1 - \frac{d_{ct}}{d}\right) \leq 1.84 \\ &= \left[3 + \ln\left(\frac{4\frac{1}{2} \text{ in.}}{18.0 \text{ in.}}\right)\right]\left(1 - \frac{1\frac{1}{2} \text{ in}}{18.0 \text{ in}}\right) \leq 1.84 \\ &= 1.48 \end{aligned}$$

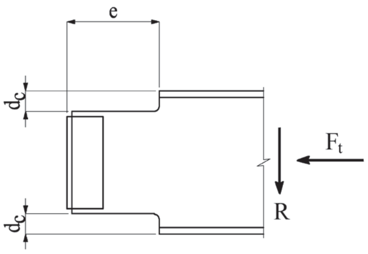

Fig. 16. Coped beam for Examples 1 and 2.

AISC *Specification* Section F11 is used with $C_b = 1.48$ and $L_b = c_t = 4\frac{1}{2}$ in. (Dowswell and Whyte, 2014):

$$M_y = (50 \text{ ksi})\left[\frac{(0.355 \text{ in.})(15.0 \text{ in.})^2}{6}\right]$$
$$= 666 \text{ kip-in.}$$

$$M_p = (50 \text{ ksi})\left[\frac{(0.355 \text{ in.})(15.0 \text{ in.})^2}{4}\right]$$
$$= 998 \text{ kip-in.}$$

$$\frac{L_b d}{t^2} = \frac{(4\tfrac{1}{2} \text{ in.})(18.0 \text{ in.})}{(0.355 \text{ in.})^2}$$
$$= 643$$

$$\frac{0.08E}{F_y} = \frac{(0.08)(29{,}000 \text{ ksi})}{(50 \text{ ksi})}$$
$$= 46.4$$

$$\frac{1.9E}{F_y} = \frac{(1.9)(29{,}000 \text{ ksi})}{(50 \text{ ksi})}$$
$$= 1{,}100$$

$$46.4 < 643 < 1{,}100$$

Therefore, the nominal flexural strength is

$$M_n = C_b\left[1.52 - 0.274\left(\frac{L_b d}{t^2}\right)\frac{F_y}{E}\right]M_y \le M_p$$
$$= (1.48)\left[1.52 - (0.274)(643)\left(\frac{50 \text{ ksi}}{29{,}000 \text{ ksi}}\right)\right](666 \text{ kip-in.}) \le 998 \text{ kip-in.}$$
$$= 998 \text{ kip-in.}$$

LRFD	ASD
$\phi M_n = (0.9)(998 \text{ kip-in.})$ $= 898$ kip-in.	$\dfrac{M_n}{\Omega} = \dfrac{998 \text{ kip-in.}}{1.67}$ $= 598$ kip-in.

Axial Strength

$$A_g = h_o t_w$$
$$= (15.0 \text{ in.})(0.355 \text{ in.})$$
$$= 5.33 \text{ in.}^2$$

$$\frac{KL}{r} = \frac{(0.5)(4\tfrac{1}{2}\text{ in.})}{(0.355\text{ in.})/\sqrt{12}}$$
$$= 22.0$$

$$22.0 < 25$$

Therefore, according to *Specification* Section J4.4,

$$\begin{aligned} P_n &= F_y A_g \\ &= (50\text{ ksi})(5.33\text{ in.}^2) \\ &= 267\text{ kips} \end{aligned}$$

LRFD	ASD
$\phi P_n = (0.9)(267\text{ kips})$ $= 240\text{ kips}$	$\frac{P_n}{\Omega} = \frac{267\text{ kips}}{1.67}$ $= 160\text{ kips}$

Stability Interaction

When $0.12 < \lambda_y \leq 0.33$ ($KL/r \leq 25$ for $F_y = 50$ ksi) and $M_n = M_p$, the effects of stability can be neglected and the interaction equation in AISC *Specification* Section H1.1 is applicable.

LRFD	ASD
$\frac{P_r}{P_c} = \frac{P_u}{\phi P_n}$ $= \frac{120\text{ kips}}{240\text{ kips}}$ $= 0.500$	$\frac{P_r}{P_c} = \frac{P_a}{P_n/\Omega}$ $= \frac{80\text{ kips}}{160\text{ kips}}$ $= 0.500$

Because 0.500 ≥ 0.2, according to *Specification* Section H1.1,

$$\frac{P_r}{P_c} + \frac{8}{9}\left(\frac{M_{rx}}{M_{cx}}\right) \leq 1.0$$

LRFD	ASD
$0.500 + \frac{8}{9}\left(\frac{405\text{ kip-in.}}{898\text{ kip-in.}}\right) = 0.901 < 1.0$	$0.500 + \frac{8}{9}\left(\frac{270\text{ kip-in.}}{598\text{ kip-in.}}\right) = 0.901 < 1.0$

Therefore, the cope is adequate for the limit state of local stability.

Coped Beam Example 2

In this example, the cope buckling strength will be calculated for a double-coped W18×50 beam subjected to shear and axial compression. The cope is 18 in. long × 1½ in. deep at both flanges as shown in Figure 16. The beam material is ASTM A992, and the beam is braced laterally by a floor slab at the face of the top-flange cope.

ASTM A992: $F_y = 50$ ksi

W18×50: $t_w = 0.355$ in. $d = 18.0$ in.

Cope length: $c = c_t = c_b = 18$ in.

Cope depth: $d_c = d_{ct} = d_{cb} = 1\frac{1}{2}$ in.

Distance from the face of the cope to the end reaction: $e = 18$ in.

Reduced depth of web, $h_o = 18.0 \text{ in.} - (2)(1\frac{1}{2} \text{ in.}) = 15.0$ in.

The vertical and horizontal reactions are shown here:

LRFD	ASD
$R_u = 15$ kips $F_{tu} = 45$ kips	$R_a = 10$ kips $F_{ta} = 30$ kips

The moment at the face of the cope is $M = Re$:

LRFD	ASD
$\begin{aligned} M_u &= R_u e \\ &= (15 \text{ kip})(18 \text{ in.}) \\ &= 270 \text{ kip-in.} \end{aligned}$	$\begin{aligned} M_u &= R_u e \\ &= (10 \text{ kip})(18 \text{ in.}) \\ &= 180 \text{ kip-in.} \end{aligned}$

Flexural Strength

From Dowswell and Whyte (2014), for beams with equal cope lengths at the top and bottom flange, C_b is

$$\begin{aligned} C_b &= \left[3 + \ln\left(\frac{L_b}{d}\right)\right]\left(1 - \frac{d_{ct}}{d}\right) \le 1.84 \\ &= \left[3 + \ln\left(\frac{18 \text{ in.}}{18.0 \text{ in.}}\right)\right]\left(1 - \frac{1\frac{1}{2} \text{ in}}{18.0 \text{ in}}\right) \le 1.84 \\ &= 1.84 \end{aligned}$$

AISC *Specification* Section F11 is used with $C_b = 1.84$ and $L_b = c_t = 18$ in. (Dowswell and Whyte, 2014):

$$\begin{aligned} S_x &= \frac{(0.355 \text{ in.})(15.0 \text{ in.})^2}{6} \\ &= 13.3 \text{ in.}^3 \end{aligned}$$

$$\begin{aligned} M_p &= (50 \text{ ksi})\left[\frac{(0.355 \text{ in.})(15.0 \text{ in.})^2}{4}\right] \\ &= 998 \text{ kip-in.} \end{aligned}$$

$$\begin{aligned} \frac{L_b d}{t^2} &= \frac{(18 \text{ in.})(18.0 \text{ in.})}{(0.355 \text{ in.})^2} \\ &= 2{,}570 \end{aligned}$$

$$
\begin{aligned}
\frac{1.9E}{F_y} &= \frac{(1.9)(29{,}000 \text{ ksi})}{(50 \text{ ksi})} \\
&= 1{,}100
\end{aligned}
$$

$$1{,}100 < 2{,}570$$

Therefore, the critical stress is

$$
\begin{aligned}
F_{cr} &= \frac{1.9EC_b}{\dfrac{L_b d}{t^2}} \\
&= \frac{(1.9)(29{,}000 \text{ ksi})(1.84)}{2{,}570} \\
&= 39.4 \text{ ksi}
\end{aligned}
$$

The nominal flexural strength is

$$
\begin{aligned}
M_n &= F_{cr} S_x \le M_p \\
&= (39.4 \text{ ksi})(13.3 \text{ in.}^3) \\
&= 524 \text{ kip-in.}
\end{aligned}
$$

LRFD	ASD
$\phi M_n = (0.9)(524 \text{ kip-in.})$ $= 472 \text{ kip-in.}$	$\dfrac{M_n}{\Omega} = \dfrac{542 \text{ kip-in.}}{1.67}$ $= 314 \text{ kip-in.}$

Axial Strength

$$
\begin{aligned}
A_g &= h_o t_w \\
&= (15.0 \text{ in.})(0.355 \text{ in.}) \\
&= 5.33 \text{ in.}^2
\end{aligned}
$$

$$
\begin{aligned}
\frac{KL}{r} &= \frac{(0.5)(18 \text{ in.})}{(0.355 \text{ in.})/\sqrt{12}} \\
&= 87.8
\end{aligned}
$$

$$87.8 > 25$$

Therefore, the axial strength will be calculated according to the provisions of *Specification* Chapter E. The elastic buckling stress is

$$
\begin{aligned}
F_e &= \frac{\pi^2 E}{\left(\dfrac{KL}{r}\right)^2} \\
&= \frac{\pi^2 (29{,}000 \text{ ksi})}{(87.8)^2} \\
&= 37.1 \text{ ksi}
\end{aligned}
$$

The slenderness parameter is

$$4.71\sqrt{\frac{E}{F_y}} = 4.71\sqrt{\frac{29{,}000\text{ ksi}}{50\text{ ksi}}}$$
$$= 113$$

$$47.8 < 113$$

Therefore, the critical buckling stress is

$$F_{cr} = \left[0.658^{\left(\frac{50\text{ ksi}}{37.1\text{ ksi}}\right)}\right](50\text{ ksi})$$
$$= 28.4\text{ ksi}$$

The nominal compressive strength is

$$\begin{aligned} P_n &= F_{cr}A_g \\ &= (28.4\text{ ksi})(5.33\text{ in.}^2) \\ &= 151\text{ kips} \end{aligned}$$

LRFD	ASD
$\phi P_n = (0.9)(151\text{ kips})$ $= 136\text{ kips}$	$\frac{P_n}{\Omega} = \frac{151\text{ kips}}{1.67}$ $= 90.4\text{ kips}$

Stability Interaction

When $0.33 < \lambda_y$ ($KL/r > 25$ for 50 ksi) or $M_n < M_p$, the effects of stability must be included in the design, and the interaction equation in AISC *Specification* Section H2 is applicable. Due to the high flexural stiffness in the strong-axis direction, the strong-axis second-order moment is neglected.

LRFD	ASD
$\frac{P_r}{P_c} + \frac{M_{rx}}{M_{cx}} \le 1.0$ $\frac{45\text{ kip}}{136\text{ kip}} + \frac{270\text{ kip-in.}}{472\text{ kip-in.}} = 0.903 < 1.0$	$\frac{P_r}{P_c} + \frac{M_{rx}}{M_{cx}} \le 1.0$ $\frac{30\text{ kip}}{90.4\text{ kip}} + \frac{180\text{ kip-in.}}{314\text{ kip-in.}} = 0.905 < 1.0$

Therefore, the cope is adequate for the limit state of local stability.

Coped Beam Example 3

In this example, the cope buckling strength will be calculated for a double-coped W18×50 beam subjected to shear and axial tension. The cope is 18 in. long × 1½ in. deep at both flanges as shown in Figure 17. The beam material is ASTM A992, and the beam is braced laterally by a floor slab at the face of the top-flange cope.

ASTM A992: $F_y = 50$ ksi

W18×50: $t_w = 0.355$ in. $d = 18.0$ in.

Cope length: $c = c_t = c_b = 18$ in.

Cope depth: $d_c = d_{ct} = d_{cb} = 1\frac{1}{2}$ in.

Distance from the face of the cope to the end reaction: $e = 18$ in.

Reduced depth of web, $h_o = 18.0 \text{ in.} - (2)(1\frac{1}{2} \text{ in.}) = 15.0$ in.

The vertical and horizontal reactions are:

LRFD	ASD
$R_u = 21$ kips $F_{tu} = 120$ kips	$R_a = 14$ kips $F_{ta} = 80$ kips

The moment at the face of the cope is $M = Re$:

LRFD	ASD
$M_u = R_u e$ $= (21 \text{ kip})(18 \text{ in.})$ $= 378$ kip-in.	$M_u = R_u e$ $= (14 \text{ kip})(18 \text{ in.})$ $= 252$ kip-in.

Flexural Strength

From Dowswell and Whyte (2014), for beams with equal cope lengths at the top and bottom flange, C_b is

$$\begin{aligned} C_b &= \left[3 + \ln\left(\frac{L_b}{d}\right)\right]\left(1 - \frac{d_{ct}}{d}\right) \le 1.84 \\ &= \left[3 + \ln\left(\frac{18 \text{ in.}}{18.0 \text{ in.}}\right)\right]\left(1 - \frac{1\frac{1}{2} \text{ in.}}{18.0 \text{ in.}}\right) \le 1.84 \\ &= 1.84 \end{aligned}$$

Specification Section H1.2 will be used to calculate the effect of the tension load on the lateral-torsional buckling strength.

$$\begin{aligned} I_y &= \frac{h_o t_w^3}{12} \\ &= \frac{(15.0 \text{ in.})(0.355 \text{ in.})^3}{12} \\ &= 0.0559 \text{ in.}^4 \end{aligned}$$

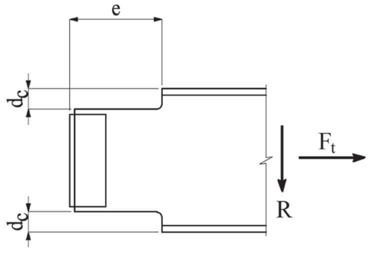

Fig. 17. Coped beam for Example 3.

$$
\begin{aligned}
P_{ey} &= \frac{\pi^2 E I_y}{L_b^2} \\
&= \frac{\pi^2 (29{,}000 \text{ ksi})(0.0559 \text{ in.}^4)}{(18 \text{ in.})^2} \\
&= 49.4 \text{ kips}
\end{aligned}
$$

According to Equation 60:

LRFD	ASD
$C_b' = 1.84\sqrt{1+\frac{(1.0)(120 \text{ kips})}{49.4 \text{ kips}}}$ $= 3.41$	$C_b' = 1.84\sqrt{1+\frac{(1.6)(80 \text{ kips})}{49.4 \text{ kips}}}$ $= 3.49$

AISC *Specification* Section F11 is used with $C_b = 3.41$ (LRFD), $C_b = 3.49$ (ASD), and $L_b = c_t = 18$ in. (Dowswell and Whyte, 2014):

$$
\begin{aligned}
S_x &= \frac{(0.355 \text{ in.})(15.0 \text{ in.})^2}{6} \\
&= 13.3 \text{ in.}^3
\end{aligned}
$$

$$
\begin{aligned}
M_p &= (50 \text{ ksi})\left[\frac{(0.355 \text{ in.})(15.0 \text{ in.})^2}{4}\right] \\
&= 998 \text{ kip-in.}
\end{aligned}
$$

$$
\begin{aligned}
\frac{L_b d}{t^2} &= \frac{(18 \text{ in.})(18.0 \text{ in.})}{(0.355 \text{ in.})^2} \\
&= 2{,}570
\end{aligned}
$$

$$
\begin{aligned}
\frac{1.9E}{F_y} &= \frac{(1.9)(29{,}000 \text{ ksi})}{(50 \text{ ksi})} \\
&= 1{,}100
\end{aligned}
$$

$$1{,}100 < 2{,}570$$

Therefore, the critical stress is

LRFD	ASD
$F_{cr} = \frac{1.9EC_b}{\frac{L_b d}{t^2}}$ $= \frac{(1.9)(29{,}000 \text{ ksi})(3.41)}{2{,}570}$ $= 73.1 \text{ ksi}$	$F_{cr} = \frac{1.9EC_b}{\frac{L_b d}{t^2}}$ $= \frac{(1.9)(29{,}000 \text{ ksi})(3.49)}{2{,}570}$ $= 74.8 \text{ ksi}$

The nominal flexural strength is

LRFD	ASD
$M_n = F_{cr}S_x \le M_p$ $= (73.1 \text{ ksi})(13.3 \text{ in.}^3)$ $= 972 \text{ kip-in.}$	$M_n = F_{cr}S_x \le M_p$ $= (74.8 \text{ ksi})(13.3 \text{ in.}^3)$ $= 995 \text{ kip-in.}$

LRFD	ASD
$\phi M_n = (0.9)(972 \text{ kip-in.})$ $= 875 \text{ kip-in.}$	$\dfrac{M_n}{\Omega} = \dfrac{995 \text{ kip-in.}}{1.67}$ $= 596 \text{ kip-in.}$

Axial Strength

$$A_g = h_o t_w$$
$$= (15.0 \text{ in.})(0.355 \text{ in.})$$
$$= 5.33 \text{ in.}^2$$
$$P_n = F_y A_g$$
$$= (50 \text{ ksi})(5.33 \text{ in.}^2)$$
$$= 267 \text{ kips}$$

LRFD	ASD
$\phi P_n = (0.9)(267 \text{ kips})$ $= 240 \text{ kips}$	$\dfrac{P_n}{\Omega} = \dfrac{267 \text{ kips}}{1.67}$ $= 160 \text{ kips}$

Stability Interaction

When $0.33 < \lambda_y$ ($KL/r > 25$ for 50 ksi) or $M_n < M_p$, the effects of stability must be included in the design, and the interaction equation in AISC *Specification* Section H2 is applicable.

$$\frac{P_r}{P_c} + \frac{M_{rx}}{M_{cx}} \le 1.0$$

LRFD	ASD
$\dfrac{P_r}{P_c} + \dfrac{M_{rx}}{M_{cx}} \le 1.0$ $\dfrac{120 \text{ kip}}{240 \text{ kip}} + \dfrac{378 \text{ kip-in.}}{875 \text{ kip-in.}} = 0.932 < 1.0$	$\dfrac{P_r}{P_c} + \dfrac{M_{rx}}{M_{cx}} \le 1.0$ $\dfrac{80 \text{ kip}}{160 \text{ kip}} + \dfrac{252 \text{ kip-in.}}{596 \text{ kip-in.}} = 0.923 < 1.0$

Therefore, the cope is adequate for the limit state of local stability.

SYMBOLS

A_c	area of the elastic core, in.^{2}
A_g	gross cross-sectional area, in.^{2}
B	moment amplification multiplier
C_b	lateral-torsional buckling modification factor
C_w	warping constant, in.^{6}
E	modulus of elasticity, ksi
F_{cr}	critical buckling stress, ksi
F_e	elastic buckling stress, ksi
F_y	specified minimum yield stress, ksi
G	shear modulus of elasticity, ksi
H	flexural constant
I	moment of inertia about the bending axis
I_x	strong-axis moment of inertia, in.^{4}
I_y	weak-axis moment of inertia, in.^{4}
I_{yc}	weak-axis moment of inertia of the elastic core, in.^{4}
J	torsional constant, in.^{4}
K	effective length factor for flexural buckling
K_t	torsion parameter
L	laterally unbraced length for lateral buckling, in.
L_b	distance between brace points for lateral-torsional buckling, in.
M_1	first-order moment, kip-in.
M_2	second-order moment, kip-in.
M_A	absolute value of moment at quarter point of the unbraced segment, kip-in.
M_B	absolute value of moment at centerline of the unbraced segment, kip-in.
M_C	absolute value of moment at three-quarter point of the unbraced segment, kip-in.
M_{cx}	available flexural strength about the strong axis, kip-in.
M_{cy}	available flexural strength about the weak axis, kip-in.
M_e	elastic critical buckling moment, kip-in.
$M_{\max}$	absolute value of maximum moment in the unbraced segment, kip-in.
M_n	nominal moment, kip-in.
M_p	plastic moment, kip-in.
M_r	required flexural strength, kip-in.
M_{rx}	required flexural strength about the strong axis, kip-in.
M_{ry}	required flexural strength about the weak axis, kip-in.
M_y	nominal strong-axis yield moment, kip-in.
P	axial load, kips
P_c	available axial strength, kips
P_e	elastic critical buckling load, kips
P_{el}	elastic critical buckling load for an eccentrically loaded compression member, kips
P_{ey}	elastic weak-axis critical buckling load, kips
P_{ez}	elastic torsional critical buckling load, kips
P_r	required axial strength, kips
P_y	axial yield load, kips
R_m	cross-section monosymmetry parameter
S_x	strong-axis elastic section modulus, in.^{3}
Z_x	strong-axis plastic modulus, in.^{3}
b	width of elastic core, in.
d	plate depth, in.
e_y	eccentricity in the y-direction, inducing strong-axis flexure, in.
r	radius of gyration, in.
r_o	polar radius of gyration, in.
r_x	strong-axis radius of gyration, in.
t	plate thickness, in
x_s	width of the rectangular tension block in the simplified residual stress pattern
α	elastic core dimensional parameter
δ_0	initial mid-height out-of-straightness, in.
γ	depth of the yielded portion of the cross section
λ	slenderness parameter for lateral-torsional buckling
λ_y	slenderness parameter for flexural buckling
σ	axial stress, ksi
σ_{rc}	compression residual stress, ksi
σ_{rt}	tension residual stress, ksi
σ_y	yield stress, ksi
τ	ratio of tangent modulus to elastic modulus

REFERENCES

AISC (1997), *Hollow Structural Sections Connections Manual,* American Institute of Steel Construction, Chicago, IL.

AISC (2010a), *Specification for Structural Steel Buildings*, ANSI/AISC 360-10, American Institute of Steel Construction, Chicago, IL.

AISC (2010b), *Code of Standard Practice for Steel Buildings and Bridges*, American Institute of Steel Construction, Chicago, IL.

AISC (2011), *Steel Construction Manual*, 14th Ed., American Institute of Steel Construction, Chicago, IL.

Albermani, F., Khoo, X. and Perera, M. (2009), "Design of Eccentrically Connected Cleat Plates in Compression," *Proceedings of the Sixth International Conference on Advances in Steel Structures*, Hong Kong, China, The Hong Kong Institute of Steel Construction.

Alpsten, G.A. (1968), "Thermal Residual Stresses in Hot-Rolled Steel Members," Report No. 337.3, Fritz Engineering Laboratory, Lehigh University, Bethlehem, PA.

Alpsten, G.A. and Tall, L. (1969), "Residual Stresses in Thick Welded Plates," Report No. 337.12, Fritz Engineering Laboratory, Lehigh University, Bethlehem, PA.

ASCE (1997), *Effective Length and Notional Load Approaches for Assessing Frame Stability: Implications for American Steel Design*, American Society of Civil Engineers, Reston, VA.

ASTM (2013), *Standard Specification for General Requirements for Rolled Structural Steel Bars, Plates, Shapes, and Sheet Piling*, ASTM A6, ASTM International, West Conshohocken, PA.

Bambach, M.R. and Rasmussen, K.J.R. (2002, May), "Tests of Unstiffened Elements Under Combined Compression and Bending," Research Report No. R818, Center for Advanced Structural Engineering, The University of Sydney.

Bjorhovde, R. (1988), "Columns: From Theory to Practice," *Engineering Journal,* AISC, Vol. 25, No. 1, First Quarter, pp. 21–34.

Bjorhovde, R., Brozzetti, J., Alpsten, G.A. and Tall, L. (1972), "Residual Stresses in Thick Welded Plates," *Welding Research Supplement,* August, pp. 392-s – 405-s.

Bjorhovde, R., Engstrom, M.F., Griffis, L.G., Kloiber, L.A. and Malley, J.O. (2001), *Structural Steel Selection Considerations — A Guide for Students, Educators, Designers, and Builders*, American Society of Civil Engineers, Reston, VA.

Blehaut, H., Gognau, D., Flahaut, P. Khouchaf, L. and Hariri, S. (2002), "Characterisation of the Effects of Grinding on Residual Stresses," *Materials Science Forum*, Vol. 404–407, pp. 179–184.

Chakrabarti J. (2000), *Applied Plasticity,* Springer, New York, NY.

Cheng, J.J., Yura, J.A. and Johnson, C.P. (1984, July), "Design and Behavior of Coped Beam," Ferguson Lab Report, The University of Texas at Austin.

Clifton, G.C. (2006, July), "Design Procedure for Eccentrically Loaded Cleats in Compression," HERA Design and Construction Bulletin No. 80, Heavy Engineering Research Association, Manukau City, New Zealand.

Clifton, G.C., Mago, N. and El Sarraf, R. (2007), "Eccentric Cleats in Compression and Columns in Moment-Resisting Connections," HERA Report R4-142:2007, Heavy Engineering Research Association, Manukau City, New Zealand.

Dowswell, B. (2005), *Design of Steel Gusset Plates with Large Cutouts*, Ph.D. Dissertation, University of Alabama at Birmingham.

Dowswell, B. (2006), "Effective Length Factors for Gusset Plate Buckling," *Engineering Journal*, AISC, Vol. 43, No. 2, Second Quarter.

Dowswell, B. (2012a), "Effective Length Factors for Chevron Gusset Plates," *Engineering Journal*, AISC, Vol. 49, No 3, Third Quarter.

Dowswell, B. (2012b), "Connection Design for Industrial Structures—Problems and Solutions," *Proceedings of the Structures for Mining and Related Materials Handling Conference*, South African Institute of Steel Construction, October 15–18, Vanderbijlpark, South Africa.

Dowswell, B. (2014), "Gusset Plate Stability Using Variable Stress Trajectories," *Proceedings of the ASCE/SEI Structures Congress,* April 3–5, Boston, MA.

Dowswell, B. (2015), "Plastic Strength of Connection Elements," *Engineering Journal*, AISC, Vol. 52, No. 1, First Quarter.

Dowswell, B. and Whyte, R. (2014), "Local Stability of Double-Coped Beams," *Engineering Journal*, AISC, Vol. 51, No. 1, First Quarter.

Dwight, J.B. and Moxham, K.E. (1977), "Comprehensive Strength of Welded Plates," *Stability of Structures Under Static and Dynamic Loads*, ASCE, pp. 463–480.

Dwight, J.B. and Ractliffe, A.T. (1967), "The Strength of Thin Plates in Compression," *Thin Walled Steel Structures-Their Design and Use in Building*, Crosby Lockwood & Son, LTD., London, pp. 3–34.

Fouad, F.H., Davidson, J.S., Delatte, N., Calvert, E.A., Chen, S., Nunez, E. and Abdalla, R. (2003), "Structural Supports for Highway Signs, Luminaries, and Traffic Signals," NCHRP Report 494, Transportation Research Board, Washington, DC.

Galambos, T.V. (1968), *Structural Members and Frames*, Prentice-Hall, New York, NY.

Galambos, T.V. and Surovek, A.E. (2008), *Structural Stability of Steel*, John Wiley and Sons, New York, NY.

Harris, I.D. (1997), "Plasma Arc Cutting of Bridge Steels," Report 384, National Cooperative Highway Research Program, National Academy Press, Washington, DC.

Haaijer, G. (1953, June 15), "Welded Continuous Frames and Their Components-Progress Report S," Fritz Laboratory Report No. 205E-2, Lehigh University, Bethlehem, PA.

Hartmann, A.J. (1971), "Inelastic Flexural-Torsional Buckling," *Journal of the Engineering Mechanics Division*, ASCE, Vol. 97, No. EM4, pp. 1,103–1,119.

Harvey, J.F. (1985), *Theory and Design of Pressure Vessels*, Van Nostrand Reinhold Co., New York, NY.

Hogan, T.J. and Collins, R.T. (2010), "Design Model for Light Bracing Cleat Connections," *Steel Construction*, Australian Steel Institute, Vol. 43, No. 2, pp. 3–56.

Kim, S.E. and Chen, W.F. (1996), "Practical Advanced Analysis for Braced Steel Frame Design," *Journal of Structural Engineering*, ASCE, Vol. 122, No. 11, pp. 1,266–1,274.

McFalls, R.K. and Tall, L. (1969), "A Study of Welded Columns Manufactured from Flame-Cut Plates," *Welding Research Suplement,* April, pp. 141-s – 153-s.

Mohr, B.A. and Murray, T.M. (2008), "Bending Strength of Steel Bracket and Splice Plates," *Engineering Journal*, AISC, Vol. 45, No. 2, Second Quarter.

Neal, B.G. (1950), "The Lateral Instability of Yielded Mild Steel Beams of Rectangular Cross-Section," *Philosophical Transactions of the Royal Society of London*, Vol. 242, No. 846, pp. 197–242.

Packer, J. Sherman, D. and Lecce, M. (2010), *Hollow Structural Section Connections*, Design Guide 24, AISC, Chicago, IL.

Pisarenko, G.S. and Mullagulov, M.K. (1998), "Approximate Method for the Analysis of Stability of Beams Under the Action of a System of Longitudinal and Transverse Forces," *Strength of Materials*, Vol. 30, No. 3, pp. 291–298.

Rao, N. and Tall, L. (1961), "Residual Stresses in Welded Plates," *Welding Research Supplement,* October, pp. 468-s–480-s.

Robinson, S. (1983), *Failure of Steel Gusset Plates*, Ph.D. Dissertation, Department of Civil Engineering and Construction, The University of Ashton in Birmingham, Birmingham, AL.

Rogers, N.A. and Dwight, J.B. (1977), "Outstand Strength," *Steel Plated Structures, An International Symposium*, Granada Publishing LTD, London.

Seely, F.B. and Putnam, W.K. (1919, November 10), *The Relation Between the Elastic Strengths of Steel in Tension, Compression and Shear*, Bulletin No. 115, Engineering Experiment Station, Vol. 17, No. 11, University of Illinois, Champaign-Urbana, IL.

Spragen, W. and Claussen, G.E. (1937), "Shrinkage Stresses in Welding, A Review of Literature to January 1, 1937," *Welding Research Supplement*, November.

Tall, L. (1964), "Residual Stresses in Welded Plates," *Welding Research Supplemen*t, January, pp. 10-s–23-s.

Thornton, W.A. (1984), "Bracing Connections for Heavy Construction," *Engineering Journal*, AISC, Vol. 21, No. 3, Third Quarter, pp. 139–148.

Timoshenko, S.P. and Gere, J.M. (1961), *Theory of Elastic Stability*, 2nd Ed., McGraw-Hill, New York, NY.

Tomas, J., Nseir, J., Camotim, D. and Boissonnade, N. (2013), "Stability, Failure and Design of I-Section Steel Beams Subjected to Tension," *Proceedings of the Annual Stability Conference,* St. Louis, MO., April 16–20, Structural Stability Research Council, pp. 669–695.

Vlasov, V. Z. (1961), *Thin-Walled Elastic Beams*, 2nd Ed., National Science Foundation, Washington, DC.

Wilkinson, T., Stock, D. and Hastie, A. (2010), "Eccentric Cleat Plate Connections in Hollow Section Members in Compression," *Proceedings: Tubular Structures XIII*, The University of Hong Kong.

Wittrick, W.H. (1952), "Lateral Instability of Rectangular Beams of Strain-Hardening Material Under Uniform Bending," *Journal of the Areonautical Sciences*, Vol. 119, No. 12, pp. 835–843.

Young, B.W. and Dwight, J.B. (1971), *Residual Stresses and their Effect on the Moment Curvature Properties of Structural Steel Sections*, CIRIA Technical Note 32, London.

Dynamic Shear Strength of Riveted Structural Connections

CHRISTOPHER P. RABALAIS and C. KENNAN CRANE

ABSTRACT

Riveted lap-spliced specimens were tested to observe how the fasteners' shear strengths were affected by joint configuration, number of shear planes, and loading type. A 200,000-lbf-capacity dynamic loader was used to fail the specimens under a monotonic dynamic or monotonic quasi-static load. The test data were normalized by the number of shear planes loaded in each test and estimated ultimate tensile strength of the driven rivet. A statistical analysis (ANOVA and t-test) was conducted on data sets from the 86 tests to determine the significant factors affecting the fastener shear strength. Conclusions from the analyses indicated that the loading type has the most significant effect on shear capacity, resulting in a dynamic increase factor of 1.72 relative to the rivet's quasi-static shear capacity. Shear type did have an effect on riveted specimens performance. Joint configuration only affected the response of riveted specimens under dynamic loadings.

KEYWORDS: rivet, shear strength, dynamic loading, quasi-static loading, dynamic increase factor.

INTRODUCTION

Many national landmark bridges are relatively old, opened in early to mid-1900s. These bridges were designed and constructed using older standards and fasteners, such as hot-driven rivets.

Over the past century, rivets were tested to determine their shear only, tension only, and combined tension and shear capacities for both static and cyclic loadings. However, one scenario has yet to be tested on either bolts or rivets: a short-duration, monotonic dynamic load that causes a shear/bearing failure in the fasteners in 1 to 6 milliseconds (msec).

Civil engineers are very aware of the threat of monotonic dynamic impacts critically damaging or destroying important structural components. This is why it is important that the dynamic shear strength rivets be researched.

Few tests were conducted on the performance of riveted connections in the first years after the creation of the Research Council on Riveted and Bolted Structural Joints (RCRBSJ). Other tests were conducted in the 1930s, such as Wilson and Oliver's "Tension Tests of Rivets" (Wilson and Oliver, 1930).

The research performed in the mid-1900s tested specimens in combined tension and shear and noted the effects of initial tension in the rivet due to cooling. From that research, a ratio of ultimate shear strength of the driven rivet to ultimate tensile strength of the undriven rivet was determined to be 0.75 (Higgins and Munse, 1952; Munse and Cox, 1956; Kulak et al., 1987). It is important to note that the tensile strength was based on the undriven rivet's ultimate tensile strength. This strength is much easier to determine than the driven-rivet ultimate tensile strength. For reference, the ultimate tensile strength of the driven rivet is approximately 20% greater than the undriven strength when machine driving is used (Kulak et al., 1987; Schenker et al., 1954). Therefore, if the ratio of shear strength to tensile strength was based on the driven rivet's ultimate tensile strength, the value would be approximately 0.625. Further testing also determined that a riveted joint in double shear would perform the same as one in single shear (Jones, 1956).

OBJECTIVES

The purpose of the research presented in this article was to develop an experimental plan that examined the behavior of rivets that are subjected to both quasi-static and dynamic shear loads.

This research has the following three primary objectives:

1. Determine the dynamic and quasi-static shear strength of standard strength hot-driven rivets.
2. Compare dynamic shear strength to quasi-static shear strength for rivets in order to determine an applicable dynamic increase factor for each.
3. Determine if dynamic shear strength of the rivets is affected by joint patterns and/or number of shear

---

Christopher P. Rabalais, Research Civil Engineer, U.S. Army Corps of Engineers–Engineer Research and Development Center (USACE-ERDC), Vicksburg, MS (corresponding). Email: Christopher.P.Rabalais@usace.army.mil

C. Kennan Crane, Ph.D., P.E., Research Structural Engineer, U.S. Army Corps of Engineers–Engineer Research and Development Center (USACE-ERDC), Vicksburg, MS. Email: Charles.k.crane@usace.army.mil

Paper No. 2015-12R

planes, and verify that the quasi-static shear strength is not affected by joint patterns and number of shear planes as shown in previous research.

Research conducted by the Research Council on Structural Connections and others was reviewed and analyzed to determine the most appropriate type of specimens and variables to be tested. It was determined to fabricate specimens that incorporate axial bars and fasteners, as shown in Figure 1. These specimens were designed so that failure would occur in the fastener.

The loading of the specimens was performed by using a rapid-loading testing apparatus housed at the U.S. Army Corps of Engineers–Engineer Research and Development Center (USACE-ERDC) in Vicksburg, Mississippi. The 200-kip dynamic loader is capable of applying multiple loading rates to the specimen, with an approximate loading rate ranging from 10 to 100,000 lbf/msec. The loader was operated at the maximum loading rate possible and slowest loading rate possible for the dynamic loading type and quasi-static loading type tests, respectively. Failure of the fasteners occurred in approximately 1 to 6 msec for the dynamic loading type and in approximately 500 to 4,000 msec for the quasi-static loading type. The quasi-static loading rate is approximately 10 to 15 times faster than typical ASTM static loading/cross-head speeds. The actual loading rate for each specimen type was dependent on the fastener type.

The results of these tests were normalized to the number of fasteners and shear planes in the specimen and the average measured ultimate tensile strength of the respective fastener type. A statistical analysis was conducted on these results to determine the effects of the chosen variable on the specimen response.

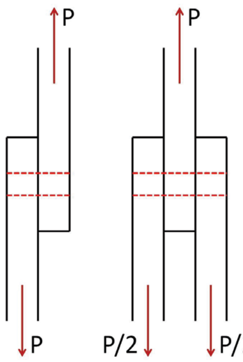

Fig. 1. Free-body diagram example of single shear (left) and double shear (right).

TEST DESIGN

Test Specimens

A test specimen for this research was defined as the combination of plates and rivet(s) to create a structural joint. Each specimen consisted of either two ½-in. plates or two ½-in. plates and one 1-in. plate, for single- and double-shear tests, respectively. The plate material complied with ASTM A36 standard specifications for carbon structural steel. The specimen plates were designed such that the only possible failure in the overall test specimen would occur from failure of the rivet in shear. A plate design was developed using connection design specifications from AISC (2011) and Kulak et al. (1987) using the "worst-case-scenario" design strengths of the test specimen components—that is, highest specified fastener strength and cross-sectional area, largest number of fasteners, double shear of the fastener, and lowest specified plate strength. Figure 2 shows the typical plate designs for the 1-in.- and ½-in.-thick specimens. The six top holes were 1$\frac{1}{16}$ in. in diameter, where the plates were attached to the gripping mechanism, and the bottom hole(s) was $\frac{9}{16}$ in. in diameter, where the fasteners attached the plates. All dimensions in Figure 2 were to the center of the appropriate hole.

The rivets used in the experiments were ASTM A502 (2003), "Standard Specifications for Rivets, Steel, Structural," grade 1, standard-strength rivets. Each rivet had a nominal diameter of ½ in., which is smaller than typical rivets in structural applications. The ½-in. size was chosen to replicate a component of a previous test that used ½-in. nominal fasteners. Note that previous research by Munse and Cox (1956) showed that a rivet's ultimate strength varied significantly depending on the diameter, but no conclusive trend was found.

Joint Configurations

This research tested five unique joint configurations. These configurations were selected to model typical joint patterns found in bridge and other structural connections and to keep the specimen response within the load capacity of the rapid loading machine. Figure 3 shows the selected joint configurations.

The first configuration was a single fastener in the center of the plate specimen. This configuration was selected as the control for the test series. It allowed for the determination of the capacity of a single fastener in both single and double shear. That capacity was then compared with other configurations to determine effects of multiple fasteners at a joint.

The second and third configurations utilized different two-fastener configurations. Configuration 2 has two fasteners in a horizontal line. Configuration 3 has two fasteners in a vertical line. The test results from configurations 2 and 3 would help to determine if a joint, under a monotonic impact/dynamic load, showed the same results.

The fourth and fifth configurations utilized different four-fastener configurations. Configuration 4 has four fasteners in a square pattern, and configuration 5 has four fasteners in a staggered configuration. These four-fastener configurations were chosen because they more closely mimicked the interaction between fasteners seen in actual structural joints. The staggered joint was chosen because it is the most typical joint configuration in use in the field as staggering of fasteners increases the efficiency of large joints under static loads (Munse, 1970).

All of the joint configurations were selected to have a large spectrum of tests to determine if the ultimate strength of the joint was truly additive based upon the number of failure planes in the joint. That is, if a joint has three failure planes, its ultimate strength should be three times greater than a joint with one failure plane. It is important to note the size of the components for this series of testing were much smaller than typical gusset plate connections in bridges and buildings. The smaller joint size was chosen to keep the joint's ultimate strength below the maximum capacity of the load frame.

Hot-Driven Rivets

The rivets were placed in the plate test specimens by Ballard Forge in Seattle, Washington. Ballard Forge used rivets procured from Jay-Cee Sales & Rivets Inc. in Farmington, Michigan. Rivets were heated and driven by a hydraulic riveter at a range of 1500 °F to 1950 °F. Dimensions of the rivet conformed to ANSI Standard B18.1.2. Note that the rivets placed for this research were not driven using pneumatic hammers like rivets driven in the field. The hydraulic riveter is used in most shop fabrications and considered to be superior to the field driving process.

The hot-driving process does two things to the rivet that are not considered when determining the design strength of a riveted joint: The rivet develops tension caused by the axial

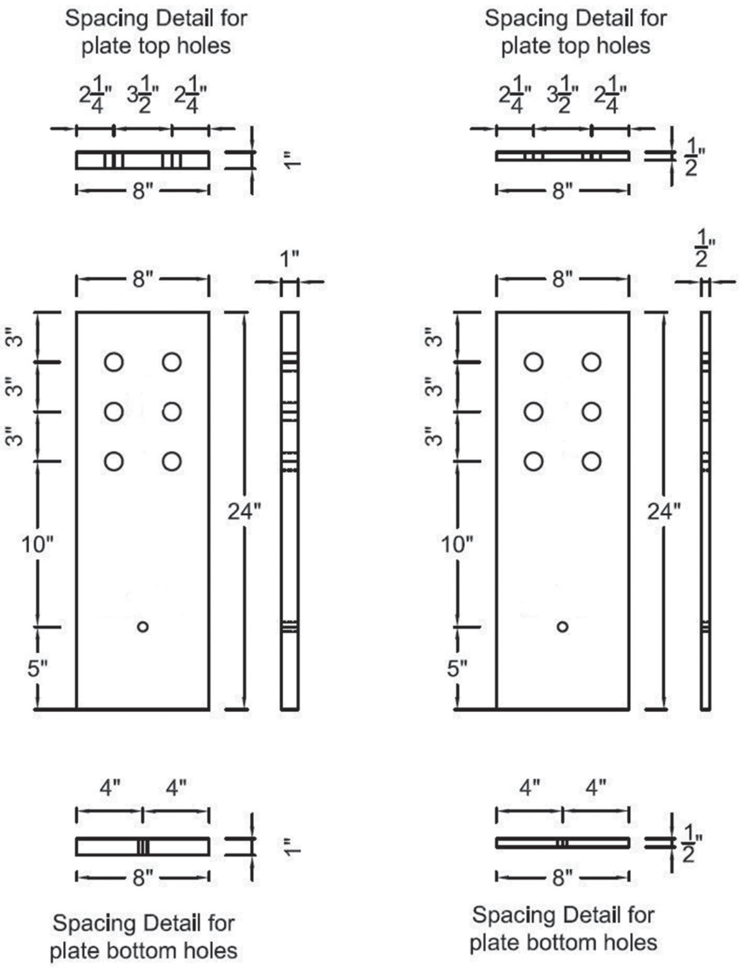

Fig. 2. Typical plate test specimens.

shrinkage of the rivet as it cools, and the rivet almost always fills the hole, as in Figure 4. Both of these effects help riveted joints to resist slip.

The nominal diameter of the rivet was 0.5 in. Post-driving, the riveted specimens that were tested had larger diameters but exhibited the characteristic of having a smaller diameter as the grip length of the rivet increased (Wilson and Oliver, 1930). The average diameter of double shear rivets was 0.545 in. for a stress area of 0.233 in.^{2} The average diameter of single shear rivets was 0.560 in. for a stress area of 0.246 in.^{2}

Samples of undriven rivets were milled and tested to ASTM E8 (2013), "Standard Test Methods for Tension Testing of Metallic Materials." The average, ultimate, undriven-rivet tensile strength was 77 ksi. An estimated value for driven-rivet strength was calculated using the hydraulic driven rivet's increase factor of 1.2 (Kulak et al., 1987; Schenker et al., 1954). Therefore, the estimated driven rivet ultimate tensile strength is 92 ksi. Size limitations of the driven rivets prevented direct measurements of the ultimate static tensile strength being taken.

Testing Machine and Instrumentation

The test specimens were failed using the 200-kip dynamic loader, shown in Figure 5. This unique loader is located at USACE-ERDC in Vicksburg, Mississippi, and has been used for many test series since the 1970s (Flathau, 1971). A uniaxial tension load was applied to the test specimen by using a compressible fluid (Xiameter/Dow Corning 100 CS silicone fluid) to apply pressure above and below a piston. The test specimen was attached to the piston and reaction structure above the piston. The bottom portion of the specimen and piston moved downward when pressure below the piston was released. The upper portion of the specimen remained stationary and resisted movement, resulting in an axial tension load applied to the specimen. Typical operating pressures of the compressible fluid for tests completed in this research ranged from 1500 to 3000 psi, depending on the number of fasteners in the specimen.

The pressure was released by a rapid-opening solenoid valve through a variable-sized orifice. The size of the orifice controlled the flow rate of the compressed fluid exiting the loader, thereby controlling the loading rate on the specimen. However, the actual load rate was dictated by the specimen's response to the load. The orifice sizes used were 4.5 in. for dynamic loading types and 1⁄16 in. for quasi-static loading types.

The typical time for the applied load to fail the test specimens was 1 to 6 msec for dynamic loading and 500 to 4000+ msec for quasi-static loading. Figures 6 and 7 show a typical load versus time curve for the dynamic and quasi-static loadings, respectively. The chosen figures were from tests with the same shear type and joint configuration but have different loading types applied.

Two load cells and two accelerometers were used to measure the forces and accelerations, respectively, during

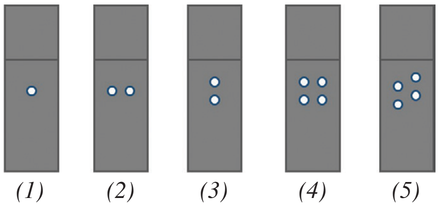

Fig. 3. Five joint configurations for testing.

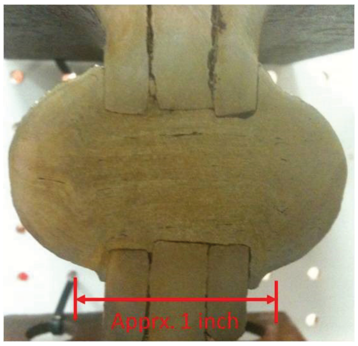

Fig. 4. Typical hot-driven, wrought iron, riveted connection cross-section.

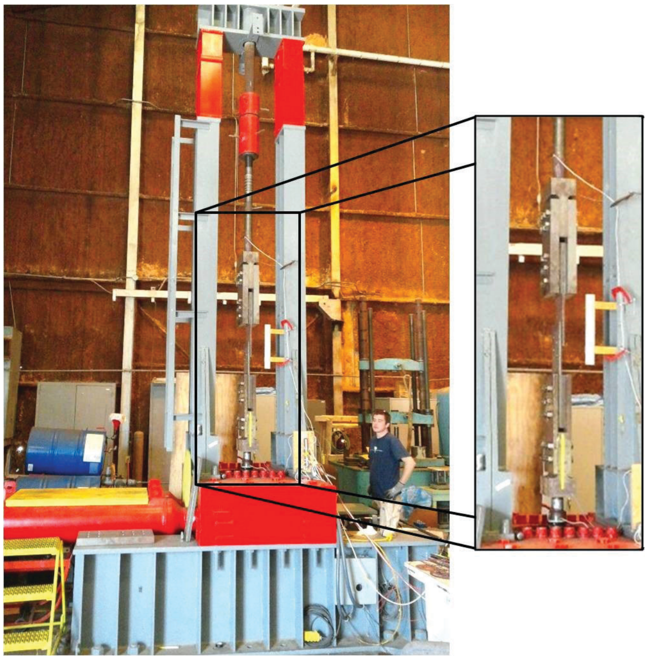

Fig. 5. 200-kip dynamic loader and test specimen.

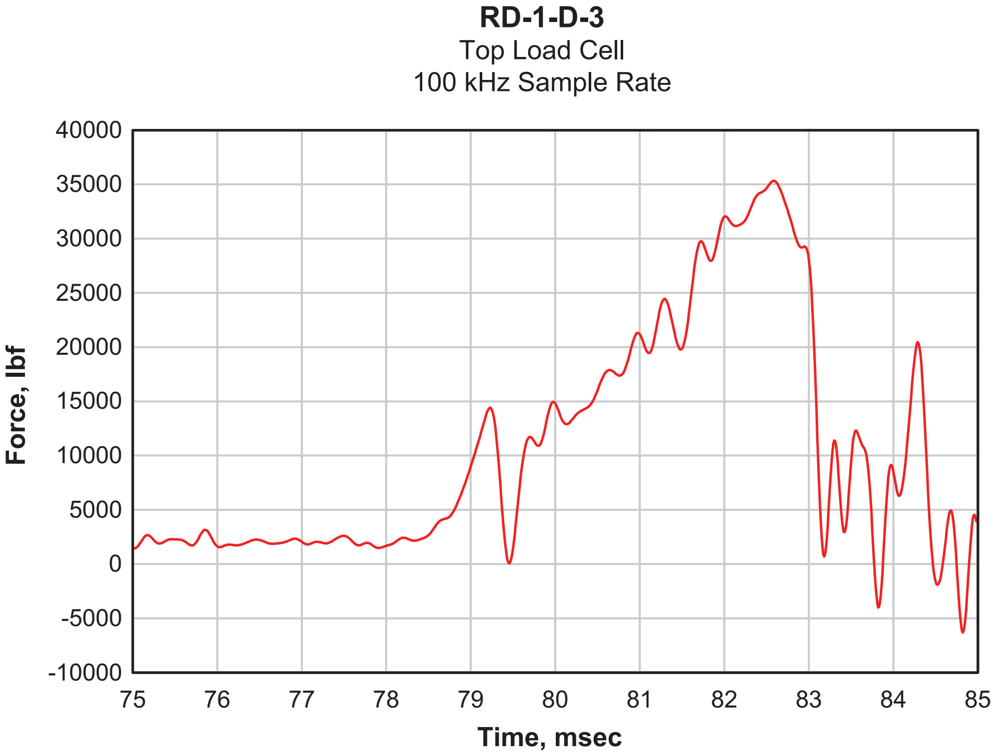

Fig. 6. Typical total load vs. time curve for dynamic loading type.

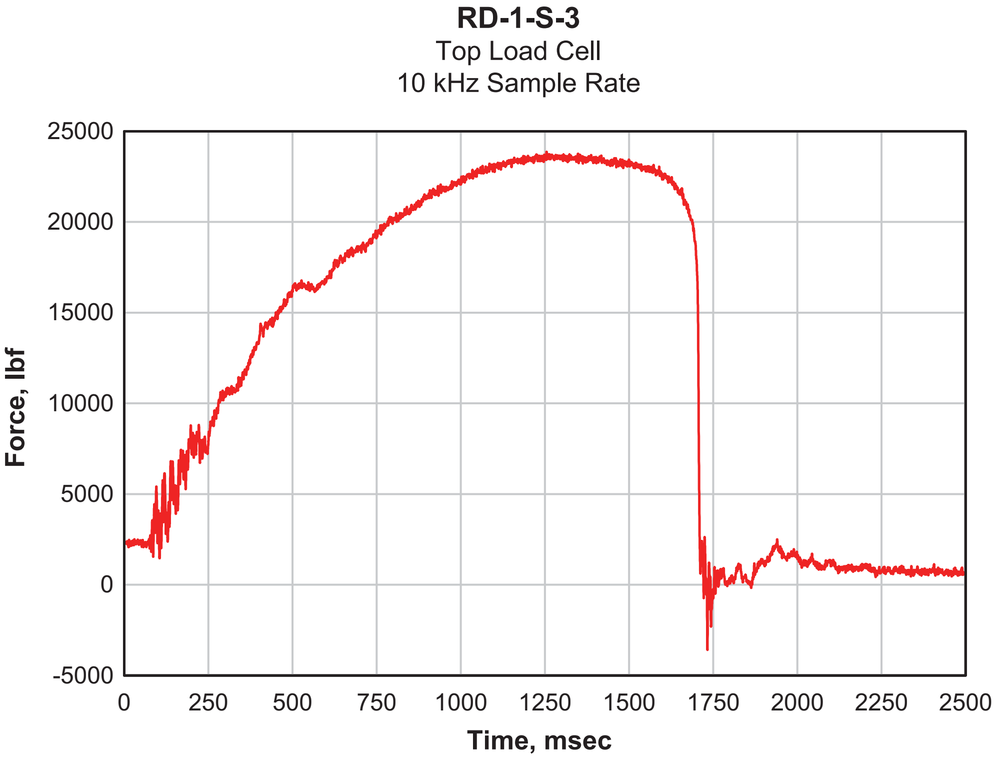

Fig. 7. Typical total load vs. time curve for quasi-static loading type.

Table 1. List of Initials Used in Test Name

Test Characteristic	Label	Description
Structural fastener type	R	Rivets
Shear type	D	Double shear
	S	Single shear
Joint configuration	1	Single fastener
	2	Two fasteners—horizontal
	3	Two fasteners—vertical
	4	Four fasteners—square
	5	Four fasteners—staggered
Loading type	D	Dynamic
	S	Quasi-static

testing. One of each was placed above and below the specimen. The two load cells were specifically designed for the 200-kip loader and were integrated into the loader structure. The load cells were comprised of a series of strain gauges arranged around a specific-diameter steel rod. The load cells were calibrated in such a way that a positive load measurement corresponded to tension, and negative load measurement corresponded to compression in the load cell.

Two Sigma 7270A 20K piezoresistive accelerometers were used initially, but they were damaged during testing of one specimen. Two PCB Electronics Model 3991A1120KG piezoresistive accelerometers were used in their place for the remainder of the tests. All four accelerometers had a peak sensitivity of 20,000 g's. The accelerometers were mounted to the specimen in a vertical orientation in order to measure the acceleration of the specimen in the direction of loading. The accelerometers were calibrated such that a positive acceleration measurement corresponded to the specimen accelerating up, and a negative acceleration measurement corresponded to the specimen accelerating down.

All the data were recorded using a Hi-Techniques Synergy P data acquisition system. The data from the instrumentation used for this test series were collected at a 100-kHz to 1000-kHz sampling rate for the dynamic loading type tests and at a 10-kHz sampling rate for the quasi-static loading type tests. Acquisition of the data was triggered remotely when the rapid-opening valve was fired.

Phantom v4.3 and v5.1 high-speed cameras were used to record footage at 8,113 frames per second (fps) for dynamic tests and 1000 fps for quasi-static tests. The resolution of the footage is limited to 256 × 256 pixels because of the frame rate needed to accurately capture footage for dynamic tests. The camera was triggered simultaneously with the data acquisition system. The high-speed camera footage was used to aid in determining the time of maximum load and failure of the specimen.

Test Labeling

The labeling system for test names in the test series was in the following order:

- Structural fastener type/shear type
- Joint configuration
- Loading type
- Test number

The list of initials used in the test name is shown in Table 1. For example, the riveted, single-shear, single-fastener, dynamic loading, test number 4 had the test name: "RS-1-D-4".

Each joint configuration was tested at least four times for each loading type and for each shear type. Some test combinations had more tests added than others due to malfunctions during testing of previous tests of that combination. A total of 86 tests were conducted on riveted lap splices.

TEST RESULTS

The table of results for each loading type is shown in Tables 2 and 3. All data values shown in the "Dynamic Load" or "Quasi-Static Load" columns of Tables 2 and 3 were values from the upper load cell (for both loading types) and accelerometer (for dynamic loading types only). Data values in the "Ratio of Ultimate Shear Stress to Ultimate Tensile Stress" column were the average ratio of shear stress to ultimate tensile stress seen by a single shear plane on the fastener (values were normalized by the number of shear planes in the test). Footnoted values in that column were excluded from analysis.

The upper load cell and accelerometer data for the dynamic tests were processed using existing processes developed in Flathau (1971) specifically for the 200-kip

Table 2. Results from Riveted, Dynamic Loading Type Specimens

Test Name	Estimated Ultimate Tensile Strength, ksi	Stress Area, in.^{2}	Dynamic Load, lbf	Shear Load of Each Rivet per Plane, lb	Shear Stress of Each Rivet per Plane, psi	Ratio of Ultimate Shear Stress to Ultimate Tensile Strength, ksi/ksi
RD-1-D-1	92	0.2333	30997	15498	66436	0.722
RD-1-D-2	92	0.2333	44711	22356	95830	1.042[1]
RD-1-D-3	92	0.2333	35320	17660	75702	0.823
RD-1-D-4	92	0.2333	33290	16645	71352	0.776
RS-1-D-1	92	0.2463	16149	16149	69224	0.713
RS-1-D-2	92	0.2463	15577	15577	66771	0.687
RS-1-D-3	92	0.2463	13717	13717	58799	0.605
RS-1-D-4	92	0.2463	16120	16120	69100	0.711
RD-2-D-1	92	0.2333	85304	21326	91417	0.994
RD-2-D-2	92	0.2333	72277	18069	77457	0.842
RD-2-D-3	92	0.2333	85538	21385	91668	0.996
RD-2-D-4	92	0.2333	55856	13964	59859	0.651
RS-2-D-1	92	0.2463	39446	19723	84546	0.870
RS-2-D-2	92	0.2463	47960	23980	102793	1.056
RS-2-D-3	92	0.2463	42505	21253	91103	0.938
RS-2-D-4	92	0.2463	79577	39789	170559	1.756
RS-2-D-5	92	0.2463	77341	38671	165767	1.707
RS-2-D-6	92	0.2463	—	—	—	— [2]
RD-3-D-1	92	0.2333	79761	19940	85476	0.929
RD-3-D-2	92	0.2333	132608	33152	142111	1.545
RD-3-D-3	92	0.2333	—	—	—	— [3]
RD-3-D-4	92	0.2333	106104	26526	113708	1.236
RS-3-D-1	92	0.2463	55509	27754	118973	1.225
RS-3-D-2	92	0.2463	60093	30047	128799	1.326
RS-3-D-3	92	0.2463	60332	30166	129311	1.331
RS-3-D-4	92	0.2463	54216	27108	116203	1.196
RD-4-D-1	92	0.2333	209128	26141	112057	1.218
RD-4-D-2	92	0.2333	157324	19665	84299	0.916
RD-4-D-3	92	0.2333	113424	14178	60776	0.661
RD-4-D-4	92	0.2333	246880	30860	132286	1.438
RD-4-D-5	92	0.2333	79875	9984	42800	0.465
RD-4-D-6	92	0.2333	—	—	—	— [4]
RS-4-D-1	92	0.2463	66323	16581	71076	0.732
RS-4-D-2	92	0.2463	54412	13603	58311	0.600
RS-4-D-3	92	0.2463	117432	29358	125847	1.296
RS-4-D-4	92	0.2463	101994	25498	109303	1.125
RS-4-D-5	92	0.2463	85437	21359	91559	0.943
RS-4-D-6	92	0.2463	79230	19808	84908	0.874
RD-5-D-1	92	0.2333	147573	18447	79074	0.860
RD-5-D-2	92	0.2333	160638	20080	86075	0.936
RD-5-D-3	92	0.2333	213216	26652	114247	1.242
RD-5-D-4	92	0.2333	167113	20889	89544	0.973
RS-5-D-1	92	0.2463	—	—	—	— [3]
RS-5-D-2	92	0.2463	66400	16600	71159	0.733
RS-5-D-3	92	0.2463	94465	23616	101234	1.042
RS-5-D-4	92	0.2463	83951	20988	89967	0.926

1 Malfunction of top accelerometer and maximum load value is omitted from analysis.

2 No usable data were collected.

3 No data were recorded.

4 Malfunction of top accelerometer and maximum load value is omitted from analysis.

Table 3. Results from Riveted, Quasi-Static Loading Type Specimens

Test Name	Estimated Ultimate Tensile Strength, ksi	Stress Area, in.^{2}	Dynamic Load, lbf	Shear Load of Each Rivet per Plane, lb	Shear Stress of Each Rivet per Plane, psi	Ratio of Ultimate Shear Stress to Ultimate Tensile Strength, ksi/ksi
RD-1-S-1	92	0.2333	23973	11987	51382	0.559
RD-1-S-2	92	0.2333	20460	10230	43852	0.477
RD-1-S-3	92	0.2333	23868	11934	51156	0.556
RD-1-S-4	92	0.2333	21347	10674	45754	0.497
RS-1-S-1	92	0.2463	16745	16745	71778	0.739
RS-1-S-2	92	0.2463	15885	15885	68094	0.701
RS-1-S-3	92	0.2463	15774	15774	67618	0.696
RS-1-S-4	92	0.2463	12597	12597	53998	0.556
RD-2-S-1	92	0.2333	45063	11266	48292	0.525
RD-2-S-2	92	0.2333	47787	11947	51212	0.557
RD-2-S-3	92	0.2333	—	—	—	—[1]
RD-2-S-4	92	0.2333	41680	10420	44667	0.486
RS-2-S-1	92	0.2463	34049	17024	72977	0.751
RS-2-S-2	92	0.2463	29164	14582	62509	0.644
RS-2-S-3	92	0.2463	31753	15876	68056	0.701
RS-2-S-4	92	0.2463	—	—	—	—[1]
RD-3-S-1	92	0.2333	42087	10522	45103	0.490
RD-3-S-2	92	0.2333	56375	14094	60415	0.657
RD-3-S-3	92	0.2333	50915	12729	54563	0.593
RD-3-S-4	92	0.2333	42020	10505	45031	0.489
RS-3-S-1	92	0.2463	33036	16518	70806	0.729
RS-3-S-2	92	0.2463	23757	11878	50918	0.524
RS-3-S-3	92	0.2463	25103	12552	53805	0.554
RS-3-S-4	92	0.2463	29604	14802	63451	0.653
RD-4-S-1	92	0.2333	85417	10677	45769	0.497
RD-4-S-2	92	0.2333	87479	10935	46874	0.509
RD-4-S-3	92	0.2333	98195	12274	52616	0.572
RD-4-S-4	92	0.2333	—	—	—	—[1]
RS-4-S-1	92	0.2463	51894	12974	55613	0.573
RS-4-S-2	92	0.2463	44832	11208	48045	0.495
RS-4-S-3	92	0.2463	51454	12864	55141	0.568
RS-4-S-4	92	0.2463	54607	13652	58520	0.602
RD-5-S-1	92	0.2333	86537	10817	46369	0.504
RD-5-S-2	92	0.2333	88741	11093	47550	0.517
RD-5-S-3	92	0.2333	96454	12057	51683	0.562
RD-5-S-4	92	0.2333	—	—	—	—[1]
RS-5-S-1	92	0.2463	—	—	—	—[1]
RS-5-S-2	92	0.2463	52404	13101	56160	0.578
RS-5-S-3	92	0.2463	45432	11358	48688	0.501
RS-5-S-4	92	0.2463	53620	13405	57463	0.592

[1] No data were recorded.

loader to determine the total load applied to the specimen during testing. Other data processing, such as filtering techniques detailed in Carleton (1970), was typical of the techniques used by USACE-ERDC. Further explanation of data-processing techniques is given in Rabalais (2015).

STATISTICAL ANALYSIS OF RIVETED SPECIMEN RESPONSE

The rivet specimen data were analyzed using two statistical testing techniques: the multifactor analysis of variance (ANOVA) and the t-test. The three factors that could affect the riveted specimen response, loading type, joint configuration, and shear type were inserted into a three-factor ANOVA on the data. Individual comparisons of means were conducted based on the results of this ANOVA using the t-test statistic assuming unequal sample variance so that the full significance of the results could be better understood. The probability threshold for statistical significance, or alpha value, of 0.05 is used for all statistical tests. All statistical calculations were completed using Microsoft Excel.

The ratio of ultimate shear stress to ultimate tensile strength, or "specimen response," value was selected as the response variable for the statistical analysis. This value provided for comparisons of the effects of the variables against one another.

The rivet specimen data for all tests were analyzed using the multifactor ANOVA. The three factors—loading type, joint configuration, and shear type—were inserted into a three-factor ANOVA on the riveted specimen data. The results of the rivet specimen data ANOVA indicated the most significant factor affecting the specimen response was loading type, as expected. Joint configuration also caused a statistically significantly different specimen response.

A t-test was completed on the riveted specimen data for the loading type because the ANOVA indicated it to be the most significant factor on specimen response. Figure 8 is the plot of the sample data. The t-test indicated that for riveted specimens, the two loading types caused statistically significant differences in the specimen response. The sample means were 0.992 [coefficient of variation (CV) of 30%] and 0.577 (CV of 14%) for dynamic and quasi-static loading types, respectively. The probability of the samples not being affected by loading type was less than 0.0001.

Note that for Figure 8 and other data plots herein, the individual dots were the measured data points, and the solid line across the entire plot indicated the mean of all the data points analyzed. The X-axis shows the specific samples within the factor that were being compared to one another. The medium-length line near the middle of the sample distribution was the sample mean. The first short line on either side of the mean line indicated the error bars of the mean; ±1.96 standard errors on each side of the sample mean is the range where any new sample mean will fall with 95% confidence. The outermost short lines from the mean line indicate 1 standard deviation from the sample mean.

Because the samples were very statistically significantly different, an increase in shear strength with respect to rivet ultimate static tensile strength could be quantified, referred to as the dynamic increase ratio. Computing the dynamic increase ratio for the rivet response was done by dividing the mean of the specimens subjected to dynamic loading type by the mean of the specimens subjected to quasi-static loading type. The order is specific because the increase ratio is made with respect to the ultimate static strength of the rivet. The mean difference between the samples equated to a dynamic increase ratio of 1.72.

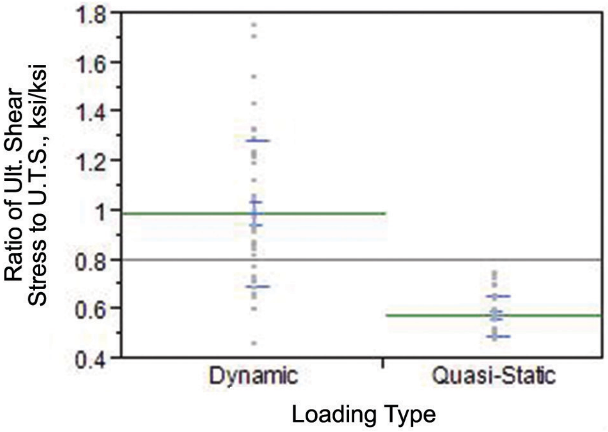

Fig. 8. Comparison by loading type for riveted specimens.

Dynamic increase ratios are not well defined for materials in shear, so it is difficult to compare the 1.72 ratio to previous research. However, results have been published for dynamic increase ratios of materials in tension. Zukas et al. (1982) show an increase in strength from approximately 60 ksi to approximately 90 ksi for SAE 1020 steel (a dynamic increase ratio of 1.5) when the tensile strain rate was increased from 0.1 s^{-1} to approximately 1000 s^{-1}. While this cannot be directly compared with the current shear tests, it does show that there is a similar increase in strength when the strain rate of a material is increased in either tension or shear.

It is important to note that the specimens' ultimate shear strength under the dynamic loading type varied more than those under quasi-static loading type. It is likely that the large variance for dynamic loading type tests is due to the much higher shear strain rates. As the load moves rapidly through the material, it will find faults in the material and will cause the material's ultimate strength to be more sensitive to local imperfections. Faults in the material vary greatly and can be attributed to several things, such as manufacturing and installation techniques. The large sample variance would significantly reduce the design shear strength used under dynamic loading conditions.

The first ANOVA also indicated the joint configuration factor caused a statistical difference for all riveted specimens and would generally be analyzed next. The next analyses performed were separate ANOVAs for riveted specimens subjected to dynamic loading type and quasi-static loading type because of the very significant difference between the loading types. This was to make sure that the statistical significance between joint configurations was not caused by the extreme difference in loading type and to clearly see if joint configuration (or shear type) had an effect on specimen response as shown in previous research.

The ANOVA results from the riveted specimens subjected to dynamic loading type indicated a statistically significant difference in the specimen response due to the joint configuration. The ANOVA results from the riveted specimens subjected to quasi-static loading type indicated a statistically significant difference in specimen response due to shear type.

The first factor analyzed using the t-test was the joint configuration for riveted specimens subjected to dynamic loading. The plot of the sample data of the riveted, dynamic-loading type specimens for each joint configuration is shown in Figure 9.

The comparisons of each configuration indicated that there were statistically significant differences in riveted specimen responses due to joint configurations. There was a significant statistical and practical difference between some configuration means. However, the variation of the data was high (numerous outliers in joint configurations 2 and 3), and the sample size was small. Therefore, it was difficult to determine the cause of the difference. More tests are needed to get a better sample distribution. Some of the difference, however, may have been due to the acceleration/inertial force data or individual sample strengths.

The next t-test was completed on the effects of shear type on the riveted specimens subjected to quasi-static loadings. Previous research had concluded that there was a difference in the response of the specimen when the grip length of compared rivets was different. The grip lengths for the rivets tested were 1 in. and 2 in. for single and double shear, respectively.

The t-test results for riveted, quasi-static specimens indicated a statistically significant difference in the specimen response due to shear type. The sample means are 0.620 (CV of 13%) and 0.532 (CV of 9%) for single and double shear, respectively. The probability that the specimen were not affected by shear type was 0.001. This was a significant difference and was practically different as well. The difference can be easily seen in the plot of the sample data shown in Figure 10. This comparison also shows that riveted

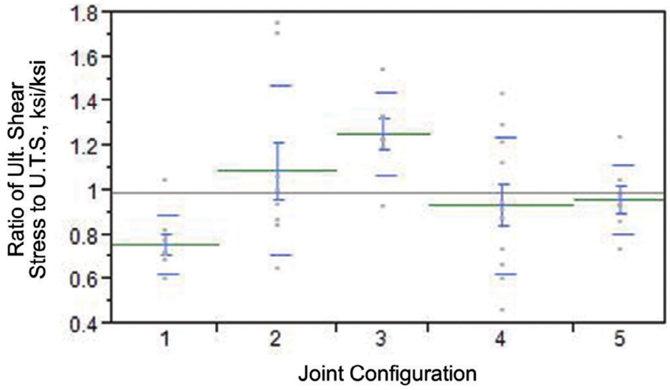

Fig. 9. Comparison by joint configuration for riveted, dynamic-loading type specimen response.

specimen response contributed significantly to the statistically significant difference due to shear type in the overall quasi-static loading–type specimens comparison.

The difference in double and single shear specimens was likely due to the longer grip length, with double shear rivets having more initial tension. Wilson and Oliver (1930) observed this effect in their testing of many rivets with multiple gauge lengths. They concluded the initial tensile stress in the rivet shank is higher in longer-grip rivets. If the double-shear rivets have a greater initial tensile stress (which is closer to the yield limit than single-shear rivets), they would not have the same amount of available strength in shear.

The riveted specimens subjected to dynamic loading type were also given a t-test comparing the response due to shear type. The results indicated no statistically significant difference, although the single-shear specimens did have a greater mean than the double-shear specimens. However, the CV of the samples was 32% and 28% for single and double shear, respectively. This large amount of variation in these samples may have masked any statistical differences in the riveted, dynamic specimen responses that were seen in the riveted, quasi-static specimens.

Design guides and other research have adjusted the measured shear strength to a factor of the undriven-rivet ultimate tensile strength. A separate analysis was completed on the normalized measured shear strength to the ultimate undriven-rivet tensile strength because testing was completed to determine the undriven-rivet ultimate tensile strength. The quasi-static specimen mean normalized to the undriven ultimate tensile strength was 0.690. The mean of single- and double-shear, quasi-static specimens was 0.741 and 0.636, respectively. This falls in line with the range of values given in Kulak et al. (1987), Wilson and Oliver (1930), and Schenker et al. (1954).

To summarize the analysis of riveted specimens, the loading type has the most significant effect on specimen response as a rivet under dynamic loading has a 72% (SD of 8.7%) increase in ultimate shear capacity when compared to a similar rivet subjected to quasi-static loading. The configuration of the joint under dynamic loading has some statistically significant effect on the specimen response. The shear type of the specimen under quasi-static loading has a statistically significant effect on the specimen response due to the grip length increasing the initial stress (decreasing available shear strength). However, the dynamic specimens show a similar result due to shear type, but there was no statistically different response, more than likely due to variation of the results.

CONCLUSIONS

The analysis of results of the tests performed in this research justified the following conclusions about the shear strength of various structural fasteners under multiple loadings, shear types, and joint configurations:

1. Loading type (dynamic or quasi-static) had the most significant effect on the shear strength of a rivet, regardless of the joint configuration or shear type. The dynamic increase factor for the quasi-static shear strength overall was 1.72.
2. Riveted specimens subjected to the quasi-static loading type were statistically significantly affected by the shear type. The riveted, double-shear specimen response was statistically significantly less than the riveted, single-shear specimen response and may be caused by an increase in initial tension (causing less available shear strength) in longer grip lengths (single-shear rivets were half the length of double-shear rivets, 1 in. to 2 in.).

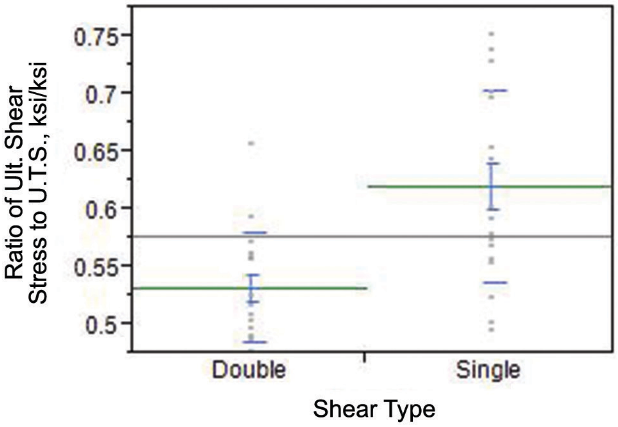

Fig. 10. Comparison by shear type of riveted, quasi-static loading-type specimen response.

3. The quasi-static shear strength of rivets, normalized to the undriven-rivet ultimate tensile strength (0.690 overall, 0.741 for single shear, 0.638 for double shear), was within the established range of values for the ratio of shear stress to tensile strength.
4. The increase factor of 1.2 for undriven-rivet ultimate tensile strength to driven-rivet ultimate tensile strength given by Kulak et al. (1987) and Schenker et al. (1954) was a good estimate for this data. The mean ratio of rivet, quasi-static specimen shear strength to the estimated ultimate driven-rivet tensile strength was 0.577, which is similar to the expected design strength for driven rivets (0.625) and von Mises failure criterion for shear strength of ductile materials (0.577).
5. The dynamic loading type induced a higher variability in the data than the quasi-static loading type (coefficient of variation of 30% and 14% for dynamic and quasi-static, respectively), possibly masking any significant differences in the data.

These conclusions are based solely on the data gathered during testing of the 86 specimens. Their individual responses may or may not be indicative of the global responses of the specimen types. The tests were completed on new steel rivets and may not be indicative of existing field rivets.

ACKNOWLEDGMENTS

This research projected was supported and funded by the Department of Homeland Security and the Federal Highway Administration. They participated in the research through interagency agreements with the U.S. Army Corps of Engineers–Engineer Research and Development Center. Permission to publish was granted by the Director, Geotechnical and Structures Laboratory, Engineer Research and Development Center, U.S. Army Corps of Engineers. Ballard Forge, Seattle, Washington, was contracted to hot-drive rivets to assemble the test specimens. Rivets were procured from Jay-Cee Sales & Rivets Inc., Farmington, Michigan. This paper is a portion of a thesis published by the primary author for partial fulfillment of a master's of science degree from Texas A&M University. Dr. William L. Beason of Texas A&M University was the thesis committee chairman.

REFERENCES

AISC (2011), *Steel Construction Manual,* 14th Ed., American Institute for Steel Construction, Chicago, IL.

ASTM (2003), "Standard Specification for Rivets, Steel, Structural," Standard A502-03, ASTM International, West Conshohocken, PA.

ASTM (2013), "Standard Test Methods for Tension Testing of Metallic Materials," Standard E8-13a, ASTM International, West Conshohocken, PA.

Carleton, H.D. (1970), "Digital Filters for Routine Data Reduction," Miscellaneous Paper N-70-1, U.S. Army Engineer Waterways Experiment Station, Vicksburg, MS.

Flathau, W.J. (1971), "Dynamic Tests of Large Reinforcing Bar Splices," Technical Report N-71-2, U.S. Army Engineer Waterways Experiment Station, Vicksburg, MS.

Higgins, T. R. and Munse, W. H. (1952), "How Much Combined Stress Can a Rivet Take?" *Engineering News-Record*, Vol. 149, No. 23, pp. 40–42.

Jones, J. (1956), "Effect of Bearing Ratio on Static Strength of Riveted Joints," *Journal of the Structural Division*, ASCE, Vol. 82, No. ST6, Paper 1108.

Kulak, G.L., Fisher, J.W. and Struik, J.H.A. (1987), *Guide to Design Criteria for Bolted and Riveted Joints,* 2nd Ed., American Institute of Steel Construction, Chicago, IL.

Munse, W.H. (1970, August), "Final Report on Riveted and Bolted Structural Joints, Project IHR-5," Structural Research Series No. 365, University of Illinois Engineering Experiment Station, Champaign, IL.

Munse, W.H. and Cox, H.L. (1956), "The Static Strength of Rivets Subjected to Combined Tension and Shear," *University of Illinois Engineering Experiment Station Bulletin*, Vol. 54, No. 437.

Rabalais, C.P. (2015), "Analysis of Bolt and Rivet Structural Fasteners Subjected to Dynamic and Quasi-Static Shear Loadings." M.S. thesis, Texas A&M University, College Station, TX.

Schenker, L., Salmon, C.G. and Johnston, B.G. (1954), "Structural Steel Connections," Engineering Research Institute, AFSWP Report No. 352, University of Michigan, Ann Arbor, MI.

Wilson, W.M. and Oliver, W.A. (1930), "Tension Tests of Rivets," *University of Illinois Engineering Experiment Station Bulletin*. Vol. 27, No. 43.

Zukas, J.A., Nicholas, T, Swift, H.F., Greszczuk, L.B. and Curran, D.R. (1982), *Impact Dynamics*. John Wiley & Sons, New York, NY.

Updates to Expected Yield Stress and Tensile Strength Ratios for Determination of Expected Member Capacity in the 2016 AISC *Seismic Provisions*

JUDY LIU

ABSTRACT

The expected yield stress and expected tensile strength ratios for hollow structural sections (HSS), pipe, and steel reinforcement for steel-concrete composite construction have been updated for the 2016 AISC *Seismic Provisions for Structural Steel Buildings*. For HSS, each grade of steel, including the new ASTM A1085 specification, has its own R_y and R_t values. Expected yield stress and tensile strength ratios have also been defined for different grades of steel reinforcement. The revisions were based on analysis of mill test data for HSS and pipe from a number of producers and a comprehensive mill survey conducted by the Concrete Reinforcing Steel Institute (CRSI).

Keywords: capacity design, expected yield stress, expected tensile strength, hollow structural sections, steel reinforcement.

INTRODUCTION

The AISC *Seismic Provisions for Structural Steel Buildings* uses a capacity design methodology for seismic force-resisting systems. For calculation of the expected capacity of a designated yielding component, the expected yield stress ratio, R_y, is employed, where R_y is defined as the ratio of the expected yield stress to the specified minimum yield stress, F_y. In the 2016 AISC *Seismic Provisions*, this ratio is also used in calculations of the limiting width-to-thickness ratios for members designated as highly or moderately ductile, as well as in calculations of spacing and required strength of lateral bracing (AISC, 2016). To better estimate expected capacities associated with fracture limit states in a designated yielding member, an expected tensile strength ratio, R_t, was introduced in the 2005 AISC *Seismic Provisions* (Liu et al., 2007), where R_t is defined as the ratio of the expected tensile strength to the specified minimum tensile strength, F_u.

For the 2016 AISC *Seismic Provisions*, updates were sought for expected yield stress and expected tensile strength ratios for hollow structural sections (HSS), pipe, and steel reinforcement for steel-concrete composite construction. Specifically, for HSS, there was interest in differentiating between the different grades of steel, such as ASTM A500 Grade C, which is the preferred material specification for round and rectangular HSS (Anderson et al., 2015). There was also interest in adding R_y and R_t values for the new ASTM A1085 specification. Further study of expected strength ratios for pipe was motivated by a potential to reduce the high ratios, which may be conservative. Mill test data for HSS and pipe were solicited and received from a number of producers. For steel reinforcement, data obtained by the Concrete Reinforcing Steel Institute (CRSI) through a comprehensive mill survey were utilized (CRSI, 2012).

HSS AND PIPE DATA

Seven different producers provided tensile test data for rectangular HSS, round HSS, and pipe, including grades A500 Grade B, A500 Grade C, A501 Grade B, and A53 Grade B. Some data sets included material specified as A500 Grade B/C. Data for ASTM A1085 were not obtained until later in the study. Outside dimensions ranged from less than 1 in to a few samples at 120 or 250 in. Thicknesses ranged from less than 0.01 in. to 0.75 in. Data provided represented mill production from 2010–2012. A53 Grade B was the sole exception, with less than 3% of data from 2008 and less than 1% from 2013. A summary of the HSS and pipe data is provided in Table 1.

Tables 2 through 10 summarize analysis results for the different grades of rectangular and round HSS and pipe. Ratios of measured to specified minimum yield stress and tensile strengths were calculated and defined as yield ratio (YR) and tensile ratio (TR). The ratios of the measured yield stress (Y) to the measured tensile strength (T) were included, along with YR/TR. Key statistics such as the average (AVG), standard deviation (ST.DEV.), coefficient of variation (CV), maximum, and minimum were calculated. Coefficient

---

Judy Liu, Professor, Oregon State University, School of Civil and Construction Engineering, Corvallis, OR, E-mail: judy.liu@oregonstate.edu

Paper No. 2016-01

Table 1. HSS and Pipe Material Specifications

Shape	Material Specification	Specified Minimum Yield Stress (ksi)	Specified Minimum Tensile Strength (ksi)	Data Count
Rectangular HSS	A500 Grade B	46	58	31,264
	A500 Grade C	50	62	14,140
	A500 Grade B/C	46	58	3,018
	A501 Grade B	50	70	402
Round HSS	A500 Grade B	42	58	2,958
	A500 Grade C	46	62	1,149
	A500 Grade B/C	42	58	568
	A501 Grade B	50	70	196
Pipe	A53 Grade B	35	60	738

Table 2. Yield and Tensile Ratios for Rectangular HSS A500 Grade B

Rect. A500 Gr. B, Count = 31264				Highly Ductile, Count = 6514				Moderately Ductile, Count = 5594			
	YR	TR	B* (in.)	YR	TR	YR/TR	Y/T	YR	TR	YR/TR	Y/T
MAX	2.52	2.04	60.0	2.17	1.81	1.27	1.01	2.28	1.94	1.27	1.01
MIN	1.00	1.00	0.75	1.01	1.00	0.72	0.57	1.00	1.00	0.77	0.61
AVG	1.31	1.26	6.14	1.36	1.29	1.06	0.84	1.32	1.26	1.06	0.84
ST.DEV.	0.12	0.09	3.16	0.13	0.10	0.08	0.07	0.12	0.10	0.09	0.07
CV	9%	7%	51%	9%	8%	8%	8%	9%	8%	9%	9%

*B is larger outside dimension

Table 3. Yield and Tensile Ratios for Rectangular HSS A500 Grade C

Rect. A500 Gr. C, Count = 14140				Highly Ductile, Count = 3736				Moderately Ductile, Count = 3042			
	YR	TR	B* (in.)	YR	TR	YR/TR	Y/T	YR	TR	YR/TR	Y/T
MAX	2.11	1.82	120	1.84	1.74	1.36	1.10	2.11	1.82	1.49	1.20
MIN	0.78	0.78	1.00	0.78	0.78	0.84	0.68	0.96	1.00	0.72	0.58
AVG	1.24	1.19	6.39	1.31	1.22	1.08	0.87	1.25	1.19	1.05	0.85
ST.DEV.	0.12	0.08	7.29	0.12	0.09	0.06	0.05	0.11	0.08	0.06	0.05
CV	9%	7%	114%	9%	7%	5%	5%	9%	7%	5%	5%

*B is larger outside dimension

of variation (CV) was calculated so that the data could be directly compared to existing material surveys. For A500 Grade B/C, the specified minimum values for yield stress and tensile strength for A500 Grade B were used in the calculations. The data in Tables 2 through 10 are separated into categories showing all samples for a given material specification and shape, as well as those shapes satisfying the limiting width-to-thickness ratios for compression elements for highly ductile and moderately ductile members. Limiting width-to-thickness ratios were calculated using Table D1.1 in the 2010 AISC *Seismic Provisions*. It should be noted that none of the rectangular HSS with very large outside dimensions (e.g., 120 or 250 in.) qualified as moderately or highly ductile. "Count" indicates number of samples, or data points, in each category (i.e., all, highly ductile, and moderately ductile samples).

Histograms were generated for ratios of measured to specified minimum yield stress and tensile strength. In general, the data exhibited normal distributions, as shown in Figures 1 and 2 for yield and tensile ratios for A500 Grade B

Table 4. Yield and Tensile Ratios for Rectangular HSS A500 Grade B/C

Rect. A500 Gr. B/C, Count = 3018				Highly Ductile, Count = 765				Moderately Ductile, Count = 764			
	YR	TR	B* (in.)	YR	TR	YR/TR	Y/T	YR	TR	YR/TR	Y/T
MAX	1.94	1.81	250	1.81	1.59	1.26	1.00	1.94	1.81	1.24	0.98
MIN	1.09	1.07	0.75	1.10	1.07	0.86	0.68	1.09	1.07	0.89	0.71
AVG	1.28	1.18	10.32	1.32	1.20	1.10	0.87	1.27	1.16	1.09	0.87
ST.DEV.	0.11	0.09	35.36	0.11	0.09	0.05	0.04	0.11	0.09	0.05	0.04
CV	9%	8%	342%	9%	7%	5%	5%	9%	8%	5%	5%

*B is larger outside dimension

Table 5. Yield and Tensile Ratios for Rectangular HSS A501 Grade B

Rect. A501 Gr. B, Count = 402				Highly Ductile, Count = 152				Moderately Ductile, Count = 30			
	YR	TR	B* (in.)	YR	TR	YR/TR	Y/T	YR	TR	YR/TR	Y/T
MAX	1.63	1.24	7.87	1.49	1.16	1.28	0.92	1.30	1.11	1.17	0.84
MIN	1.03	1.02	3.54	1.03	1.02	0.98	0.70	1.05	1.02	1.00	0.71
AVG	1.18	1.09	5.36	1.16	1.08	1.07	0.77	1.15	1.07	1.07	0.76
ST.DEV.	0.10	0.04	1.35	0.10	0.04	0.06	0.04	0.09	0.03	0.06	0.04
CV	9%	4%	25%	9%	4%	6%	6%	8%	3%	6%	6%

*B is larger outside dimension

Table 6. Yield and Tensile Ratios for Round HSS A500 Grade B

Round A500 Gr. B, Count = 2958				Highly Ductile, Count = 2736				Moderately Ductile, Count = 143			
	YR	TR	D (in.)	YR	TR	YR/TR	Y/T	YR	TR	YR/TR	Y/T
MAX	3.09	2.43	12.75	2.03	1.53	1.41	1.02	1.69	1.45	1.33	0.96
MIN	0.86	0.91	0.84	0.86	0.91	0.82	0.59	1.07	1.00	0.93	0.67
AVG	1.44	1.19	3.72	1.45	1.18	1.23	0.89	1.37	1.24	1.10	0.80
ST.DEV.	0.15	0.11	2.99	0.15	0.11	0.09	0.07	0.13	0.08	0.07	0.05
CV	11%	9%	0.81	10%	9%	8%	8%	9%	7%	6%	6%

Table 7. Yield and Tensile Ratios for Round HSS A500 Grade C

Round A500 Gr. C, Count = 1149				Highly Ductile, Count = 1070				Moderately Ductile, Count = 7			
	YR	TR	D (in.)	YR	TR	YR/TR	Y/T	YR	TR	YR/TR	Y/T
MAX	1.95	1.66	4.00	1.95	1.66	1.34	1.00	1.43	1.19	1.26	0.93
MIN	0.87	0.73	1.00	0.87	0.73	0.82	0.61	1.12	1.11	1.01	0.75
AVG	1.33	1.17	2.00	1.33	1.17	1.14	0.85	1.25	1.15	1.08	0.80
ST.DEV.	0.14	0.09	0.82	0.14	0.09	0.10	0.07	0.10	0.03	0.08	0.06
CV	11%	8%	0.41	10%	8%	9%	9%	8%	2%	8%	8%

Table 8. Yield and Tensile Ratios for Round HSS A500 Grade B/C

Round A500 Gr. B/C, Count = 568				Highly Ductile, Count = 546				Moderately Ductile, Count = 8			
	YR	TR	D (in.)	YR	TR	YR/TR	Y/T	YR	TR	YR/TR	Y/T
MAX	1.96	1.53	6.63	1.96	1.53	1.36	0.99	1.42	1.17	1.22	0.88
MIN	1.07	1.06	0.84	1.07	1.06	0.89	0.65	1.19	1.08	1.08	0.78
AVG	1.37	1.14	4.45	1.37	1.14	1.20	0.87	1.30	1.12	1.17	0.85
ST.DEV.	0.11	0.07	1.48	0.10	0.07	0.07	0.05	0.07	0.03	0.05	0.04
CV	8%	6%	33%	8%	6%	6%	6%	6%	3%	4%	4%

Table 9. Yield and Tensile Ratios for Round HSS A501 Grade B

Round A501 Gr. B, Count = 196				Highly Ductile, Count = 106				Moderately Ductile, Count = 40			
	YR	TR	D (in.)	YR	TR	YR/TR	Y/T	YR	TR	YR/TR	Y/T
MAX	1.43	1.19	7.63	1.37	1.19	1.19	0.85	1.43	1.19	1.22	0.87
MIN	1.03	0.99	3.50	1.03	0.99	0.99	0.71	1.05	1.02	0.99	0.71
AVG	1.16	1.09	5.85	1.16	1.09	1.06	0.76	1.22	1.11	1.09	0.78
ST.DEV.	0.09	0.04	1.44	0.09	0.04	0.05	0.04	0.10	0.04	0.06	0.04
CV	8%	4%	25%	8%	4%	5%	5%	8%	4%	5%	5%

Table 10. Yield and Tensile Ratios for Pipe A53 Grade B

Pipe A53 Gr. B, Count = 738				Highly Ductile, Count = 728				Moderately Ductile, Count = 10			
	YR	TR	D (in.)	YR	TR	YR/TR	Y/T	YR	TR	YR/TR	Y/T
MAX	2.06	1.30	6.63	2.06	1.30	1.69	0.99	1.86	1.14	1.68	0.98
MIN	1.26	0.97	1.66	1.34	0.97	1.30	0.76	1.26	0.97	1.26	0.74
AVG	1.60	1.04	4.06	1.60	1.04	1.53	0.89	1.57	1.04	1.51	0.88
ST.DEV.	0.13	0.05	1.67	0.13	0.05	0.08	0.05	0.20	0.05	0.15	0.09
CV	8%	5%	41%	8%	5%	5%	5%	13%	4%	10%	10%

rectangular HSS. Histograms for all shapes, including some subcategories of highly ductile or moderately ductile shapes, were reported in Liu (2013).

The data were investigated for any dependency on geometric properties. Plots of ratios of measured to specified minimum yield stress versus width-to-thickness, b/t, and measured to specified minimum tensile strength versus b/t, are shown in Figures 3, 4 and 5 for A500 Grade B rectangular HSS. Figure 5 shows the measured to specified minimum yield stress for a smaller range of b/t. There does not appear to be a strong trend, or difference, in yield or tensile ratios for b/t values above or below the moderately and highly ductile limits. Figure 6 shows some dependency on the ratio of measured to specified minimum yield stress to the larger outside dimension for very small HSS. However, the difference did not appear to be significant enough to warrant discounting small HSS in the analysis. As shown in Table 2, the average yield ratio for highly ductile shapes is 1.36 compared with 1.32 for moderately ductile shapes. Similar plots were generated, and similar observations made, for other shapes and material specifications (Liu, 2013).

The 2010 AISC *Seismic Provisions* used R_y and R_t of 1.4 and 1.3 for HSS and 1.6 and 1.2, respectively, for pipe, as shown in Figure 7. These 2010 R_y and R_t values align well with the average YR and TR values for rectangular HSS A500 Grade B (Table 2) and, in particular, for highly ductile HSS. The values compare reasonably well for YR and TR for round HSS A500 Grade B (Table 6). The values may be slightly conservative for some A500 Grade C (Tables 3 and 7). The data in Tables 4 and 8 also suggest that the 2010 R_y and R_t values are appropriate for cases in which Grade B is specified, but a Grade B/C is provided. Meanwhile, the data in Tables 5 and 9 suggest that even lower values could be used for A501 Grade B, but there are relatively fewer data

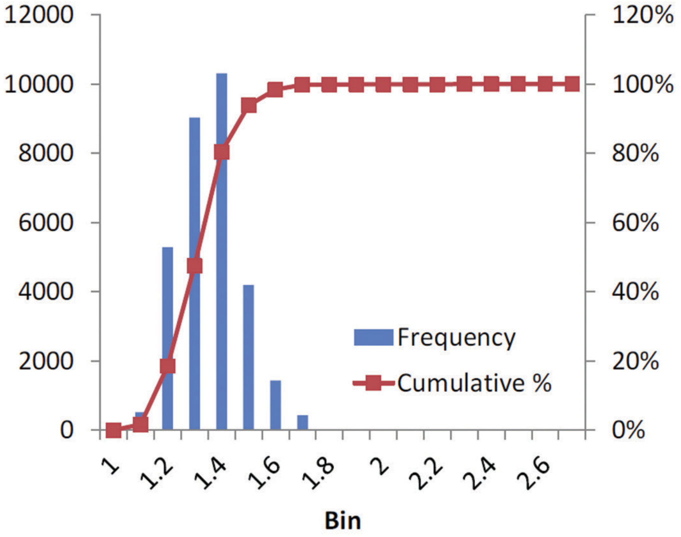

Fig. 1. Histogram for ratios of measured to specified minimum yield stress, rectangular HSS A500 Grade B.

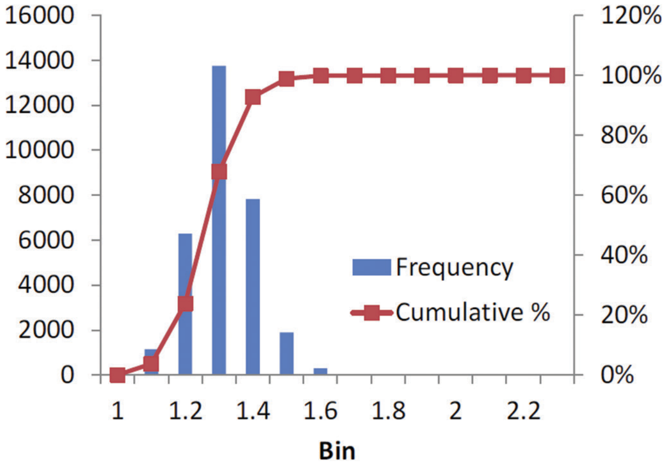

Fig. 2. Histogram for ratios of measured to specified minimum tensile strength, rectangular HSS A500 Grade B.

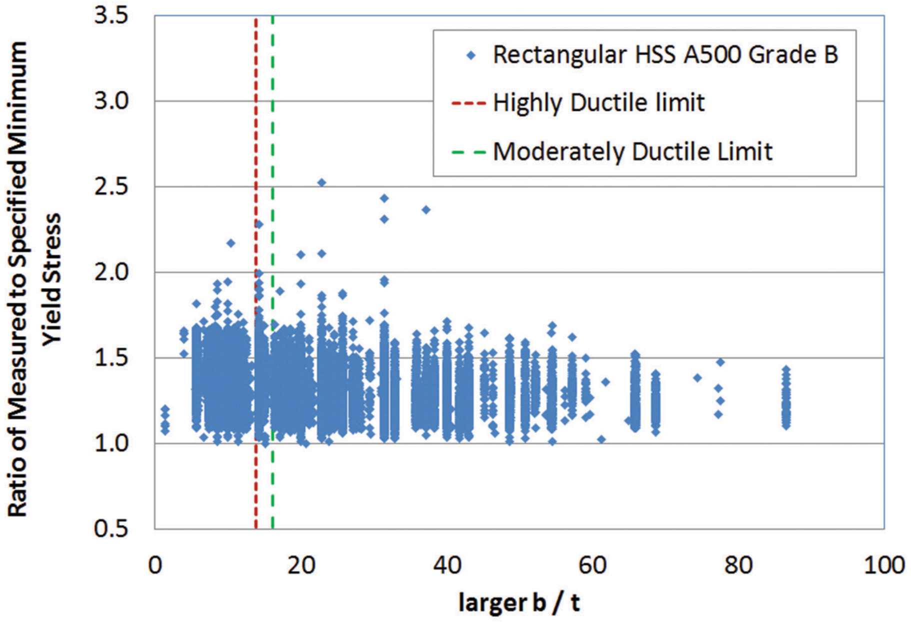

Fig. 3. Ratio of measured to specified minimum yield stress versus larger b/t *for rectangular HSS A500 Grade B.*

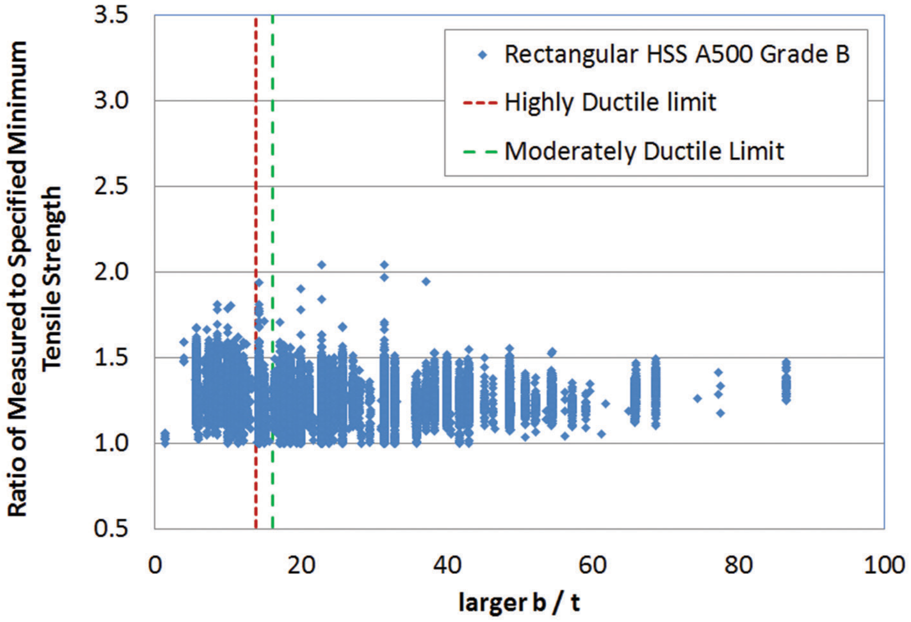

Fig. 4. Ratio of measured to specified minimum tensile strength versus larger b/t *for rectangular HSS A500 Grade B.*

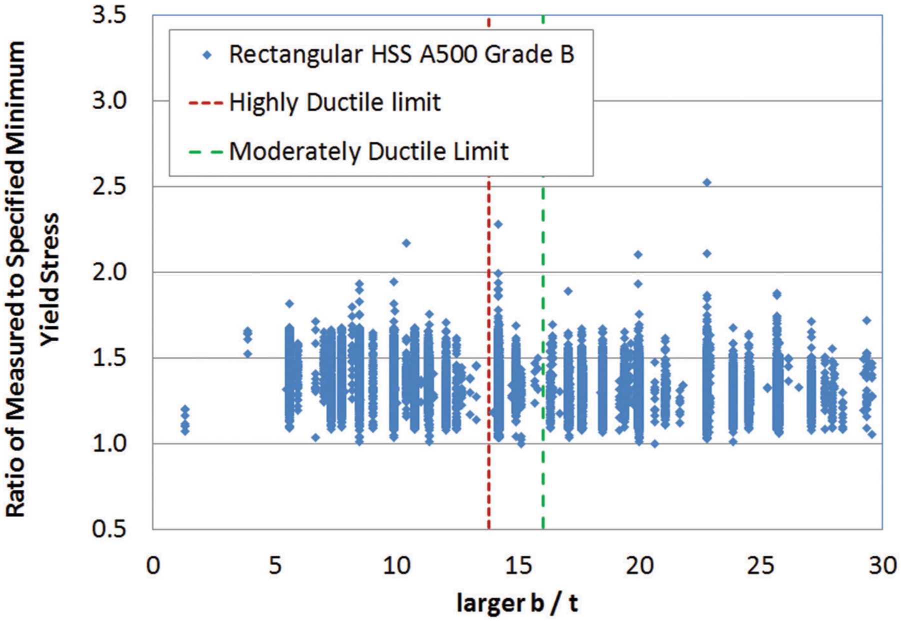

Fig. 5. Ratio of measured to specified minimum yield stress versus larger b/t for rectangular HSS A500 Grade B, shown for b/t *range of 0 to 30.*

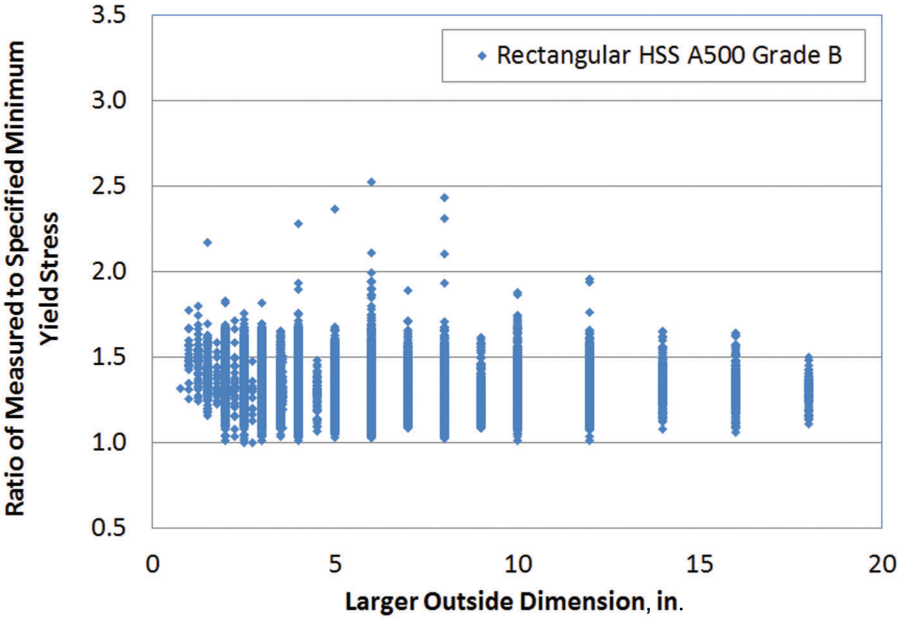

Fig. 6. Ratio of measured to specified minimum yield stress versus larger outside dimension (in.) for rectangular HSS A500 Grade B.

Table 11. Comparison of Y/T and R_yF_y/R_tF_u

Shape	Material Specification	Mean Y/T (for Highly Ductile)	R_yF_y/R_tF_u
HSS (Rectangular)	A500 Gr. B	0.84	0.85
	A500 Gr. C	0.87	0.87
	A500 Gr. B/C	0.87	0.85
	A501 Gr. B	0.77	0.77
HSS (Round)	A500 Gr. B	0.89	0.78
	A500 Gr. C	0.85	0.80
	A500 Gr. B/C	0.87	0.78
	A501 Gr. B	0.76	0.77
Pipe	A53 Gr. B	0.89	0.78

points (less than 600 total for rectangular and round HSS) to support this modification.

The data for pipe were insufficient to support any modification to the existing R_y and R_t values. One possible change, based on the data in Table 10, could be to lower the R_t value. However, these data were also primarily from one source, with relatively fewer data points than for the HSS.

Confirmation of HSS R_y and R_t values can also be seen in ratios of measured yield to measured tensile strength for individual specimens. Comparisons of the 2010 HSS R_y/R_t (1.08) to the YR/TR values in the tables for rectangular HSS show that the 2010 R_y/R_t would represent the data well, with an average YR/TR value on the order of 1.07 for rectangular HSS. The mean Y/T values may also be directly compared with the design R_yF_y/R_tF_u values, as shown in Table 11. The table again shows good correlation for rectangular HSS. However, the R_yF_y/R_tF_u values are lower than the mean Y/T values for round HSS and pipe, with the exception of A501 Grade B HSS. For design, this may result in an overestimation of the expected net section fracture capacity versus the expected gross section yield capacity.

EXPECTED YIELD AND TENSILE STRENGTH RATIOS FOR ASTM A1085

The investigation of expected yield and tensile strength ratios for ASTM A1085 was challenging due to limited production. First, in the absence of a comparable data set for A1085, a subset of the A500 Grade B, Grade C, and Grade B/C data was analyzed. The data were truncated to include only those points that satisfied the minimum yield stress of 50 ksi and the maximum yield stress of 70 ksi for A1085. Then, a small set of A1085 data was obtained and also analyzed. Tables 12 through 17 summarize the yield and tensile ratio statistics for the truncated A500 data, with comparison to the original data. The values were also sorted by highly and moderately ductile sections and analyzed for any dependence on geometric properties.

In general, the yield and tensile ratios are lower for the truncated data than for the original data, suggesting lower R_y and R_t values for A1085. Overall, the data seem to support an R_y on the order of 1.2 for A1085. However, values for highly ductile members trend higher. The yield ratios for highly ductile A500 Grade C rectangular HSS and Grade B

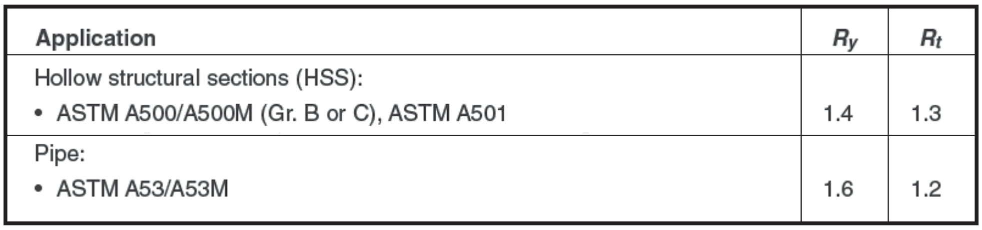

Application	R_y	R_t
Hollow structural sections (HSS): • ASTM A500/A500M (Gr. B or C), ASTM A501	1.4	1.3
Pipe: • ASTM A53/A53M	1.6	1.2

Fig. 7. Excerpt from Table A3.1, 2010 AISC Seismic Provisions, for HSS and pipe.

Table 12. Original and Truncated Data for Round A500 Grade B

Round A500 Gr. B			Truncated (i.e., without data that does not satisfy A1085)					
	Original		All		Highly Ductile		Moderately Ductile	
	Count = 2958		Count = 1870		Count = 1491		Count = 190	
	YR	TR	YR	TR	YR	TR	YR	TR
MAX	3.09	2.43	1.40	1.33	1.40	1.32	1.40	1.33
MIN	0.86	0.91	1.00	1.00	1.00	1.00	1.00	1.00
AVG	1.44	1.19	1.23	1.10	1.25	1.09	1.16	1.13
ST.DEV.	0.15	0.11	0.10	0.06	0.09	0.06	0.09	0.06
CV	11%	9%	8%	6%	7%	6%	8%	6%

Table 13. Original and Truncated Data for Round A500 Grade C

Round A500 Gr. C			Truncated (i.e., without data that does not satisfy A1085)					
	Original		All		Highly Ductile		Moderately Ductile	
	Count = 1149		Count = 967		Count = 861		Count = 40	
	YR	TR	YR	TR	YR	TR	YR	TR
MAX	1.95	1.66	1.40	1.34	1.40	1.34	1.32	1.28
MIN	0.87	0.73	1.00	1.00	1.00	1.00	1.03	1.01
AVG	1.33	1.17	1.21	1.12	1.22	1.12	1.14	1.12
ST.DEV.	0.14	0.09	0.10	0.06	0.09	0.06	0.07	0.06
CV	11%	8%	8%	6%	8%	6%	6%	5%

Table 14. Original and Truncated Data for Round A500 Grade B/C

Round A500 Gr. B/C			Truncated (i.e., without data that does not satisfy A1085)					
	Original		All		Highly Ductile		Moderately Ductile	
	Count = 568		Count = 274		Count = 222		Count = 46	
	YR	TR	YR	TR	YR	TR	YR	TR
MAX	1.96	1.53	1.40	1.23	1.40	1.23	1.36	1.18
MIN	1.07	1.06	1.01	1.00	1.01	1.00	1.07	1.00
AVG	1.37	1.14	1.19	1.06	1.19	1.06	1.20	1.05
ST.DEV.	0.11	0.07	0.07	0.05	0.07	0.05	0.08	0.05
CV	8%	6%	6%	4%	6%	4%	6%	5%

Table 15. Original and Truncated Data for Rectangular A500 Grade B

Rectangular A500 Gr. B			Truncated (i.e., without data that does not satisfy A1085)					
	Original		All		Highly Ductile		Moderately Ductile	
	Count = 31264		Count = 28048		Count = 5566		Count = 4914	
	YR	TR	YR	TR	YR	TR	YR	TR
MAX	2.52	2.04	1.40	1.53	1.40	1.49	1.40	1.53
MIN	1.00	1.00	1.00	1.00	1.00	1.00	1.00	1.00
AVG	1.31	1.26	1.20	1.13	1.23	1.14	1.21	1.13
ST.DEV.	0.12	0.09	0.09	0.07	0.09	0.08	0.09	0.07
CV	9%	7%	8%	6%	7%	7%	7%	6%

Table 16. Original and Truncated Data for Rectangular A500 Grade C

Rectangular A500 Gr. C	Original		Truncated (i.e., without data that does not satisfy A1085)					
			All		Highly Ductile		Moderately Ductile	
	Count = 14140		Count = 12691		Count = 2913		Count = 2746	
	YR	TR	YR	TR	YR	TR	YR	TR
MAX	2.11	1.82	1.40	1.40	1.40	1.40	1.40	1.38
MIN	0.78	0.78	1.00	1.00	1.01	1.00	1.00	1.00
AVG	1.24	1.19	1.22	1.13	1.26	1.14	1.23	1.12
ST.DEV.	0.12	0.08	0.09	0.06	0.08	0.07	0.09	0.06
CV	9%	7%	7%	6%	7%	6%	7%	6%

Table 17. Original and Truncated Data for Rectangular A500 Grade B/C

Rectangular A500 Gr. B/C	Original		Truncated (i.e., without data that does not satisfy A1085)					
			All		Highly Ductile		Moderately Ductile	
	Count = 3018		Count = 1857		Count = 559		Count = 425	
	YR	TR	YR	TR	YR	TR	YR	TR
MAX	1.94	1.81	1.40	1.33	1.40	1.33	1.40	1.29
MIN	1.09	1.07	1.00	1.00	1.01	1.00	1.00	1.00
AVG	1.28	1.18	1.22	1.09	1.24	1.10	1.22	1.09
ST.DEV.	0.11	0.09	0.07	0.06	0.07	0.06	0.07	0.05
CV	9%	8%	6%	5%	5%	5%	6%	5%

round HSS are 1.26 and 1.25, respectively. The data were surveyed to determine if higher yield ratios were for only for sections with small outside dimensions that might not be used in seismic applications (e.g., less than 6 in.), but there was no such trend with these data. Graphs of actual to minimum specified yield stress were also analyzed for the grades with the largest differences between highly ductile and overall R_y values (rectangular Grades B and C). These results suggested that, beyond the tendency for the average values to be higher for highly ductile members, there are no particular values of thickness, t, or width-to-thickness, b/t, for which the ratios are always high. Figures 8 and 9 show comparisons of yield ratio to b/t and t for the truncated A500 Grade C rectangular HSS data. Similar results were obtained with the Grade B data.

A very small set of A1085 data was also obtained and analyzed. There were 24 samples of ASTM A1085 steel and 31 samples of dual-grade (A1085/A500 Grade C) steel. The data set included round and rectangular HSS, with thicknesses ranging from 5⁄16 in. to 7⁄8 in. and outside dimensions ranging from 4 to 16 in. Table 18 shows yield and tensile ratio statistics. These data support an R_y on the order of 1.2 for A1085 and 1.2 or lower for R_t. Unfortunately, with so few data points, plots of yield and tensile ratios versus b/t were inconclusive.

YIELD AND TENSILE STRENGTH RATIOS FOR REINFORCING BAR

Data for A615 Grade 60, A615 Grade 75, A706 Grade 60, and Dual A615/A706 Grade 60 bars were studied with respect to expected yield and tensile strength values. For A615 Grade 60, particular attention was paid to the most commonly used bar sizes (nos. 7–11). Data had been submitted by domestic reinforcing steel producers and were estimated by CRSI to represent approximately 90% of total production in 2011 (CRSI, 2012).

Table 19 shows the number of data points and the total weight in tons for each grade of steel. Each data point represented one heat of steel, and a weight representing the size of that heat was tabulated. From this information, weighted average values, weighted standard deviations, and weighted coefficients of variation (CV) were calculated, along with maximum and minimum values. Histograms were generated for yield and tensile strengths for all grades. In general, the data exhibited normal distributions (Liu, 2013).

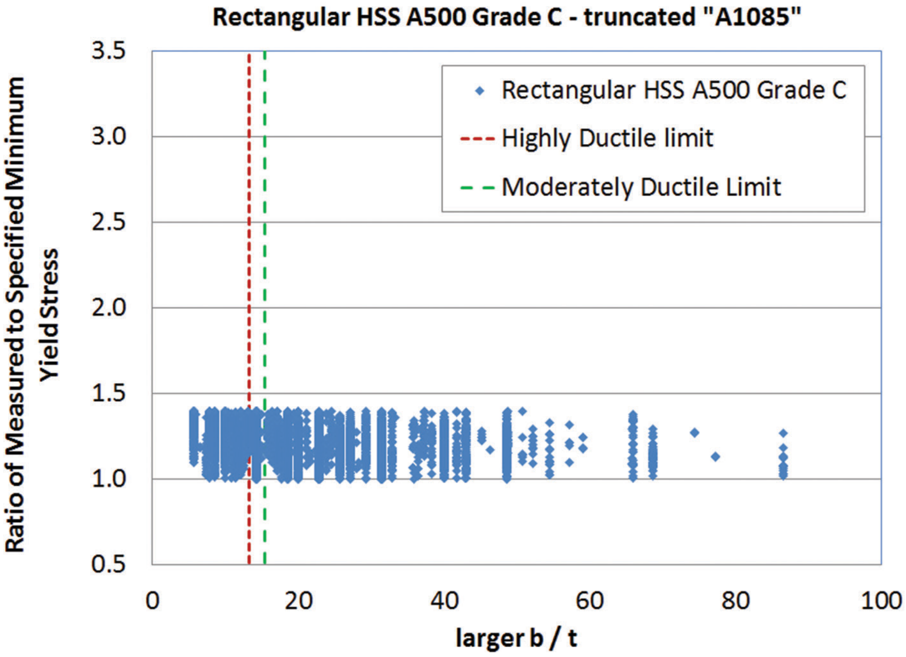

Fig. 8. Yield ratio versus b/t *for truncated A500 Grade C (rectangular HSS) data.*

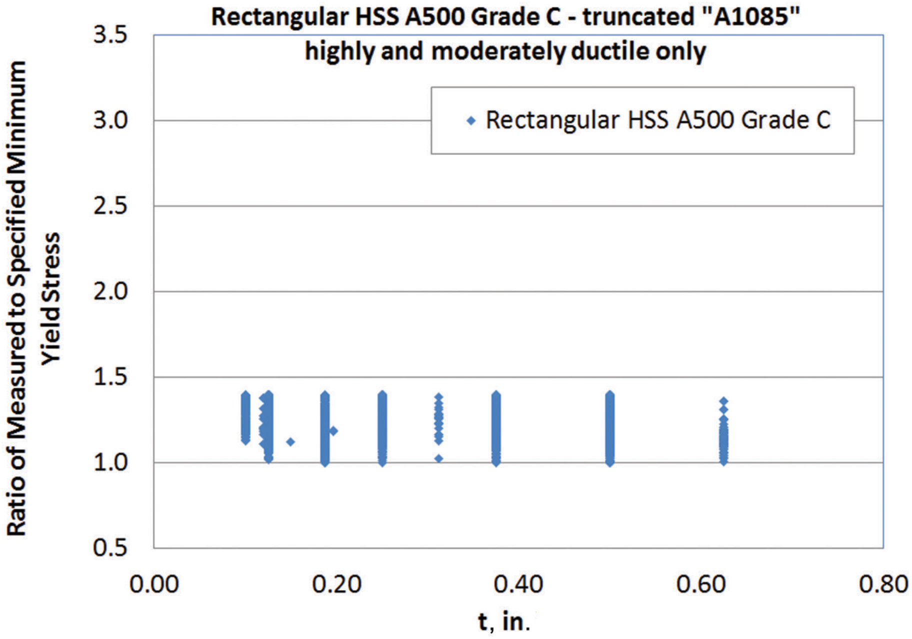

Fig. 9. Yield ratio versus thickness, t, *for truncated A500 Grade C (rectangular HSS) data.*

Table 18. Yield and Tensile Ratios for ASTM A1085 Data

	Dual-Grade (A1085/A500 Grade C)		A1085 Only	
	Count = 31		Count = 24	
	YR	TR	YR	TR
MAX	1.33	1.23	1.28	1.23
MIN	1.06	1.04	1.13	1.04
AVG	1.21	1.14	1.19	1.12
ST.DEV.	0.07	0.05	0.04	0.05

Table 19. Reinforcing Bar Data Analyzed

Material Specification	Data Count	Weight (tons)
A615 Grade 60	19,860	1,054,190
A615 Grade 75	2,174	147,930
A706 Grade 60	5,810	320,708
Dual A615/A706 Grade 60	1,328	132,315

Table 20. Yield and Tensile Strength Data for A615 Grade 60 Bar

Bar Size	Data Count	Weight (tons)	Yield Ratio (Weighted Average)	Tensile Ratio (Weighted Average)
3	1,794	136,863	1.18	1.21
4	12,225	810,826	1.18	1.17
5	16,321	1,059,469	1.17	1.17
6	11,445	747,669	1.17	1.18
7	4,555	297,294	1.17	1.18
8	5,233	343,707	1.18	1.16
9	3,743	243,603	1.19	1.17
10	2,791	171,807	1.19	1.15
11	3,538	231,539	1.19	1.15
14	131	8,247	1.20	1.14
18	56	3,167	1.24	1.17
ALL sizes	61,832	4,054,190	1.18	1.17
7 to 11 only	19,860	1,287,950	1.18	1.16

The 2010 AISC *Seismic Provisions* used R_y and R_t values of 1.25 for all steel reinforcement (AISC, 2010). Analysis of the CRSI data supported lower expected yield stress and tensile strength ratios for the grades investigated (Liu, 2013). Table 20 summarizes data for A615 Grade 60 bars, showing average yield and tensile ratios less than 1.20 for the entire data set. The average value for the no. 18 bars was 1.24, but the expected yield ratio for a subset of more common bar sizes (nos. 7–11) averaged less than 1.20. Similar results were obtained for all grades, with the exception of A615 Grade 75, which had an average yield ratio of 1.11. Meanwhile, the CRSI database only included 11 samples for A706 Grade 80 bars, but those data suggested similar yield and tensile strength ratios as for A706 Grade 60 bars. Similarly, the 21 samples for A615 Grade 80 bars showed similar yield and tensile strength ratios as for the A615 Grade 75 bars (CRSI, 2012).

Table 21. HSS and Steel Reinforcement R_y and R_t Values in the 2016 *Seismic Provisions* (AISC, 2016)

Application	R_y	R_t
Hollow Structural Sections (HSS)		
ASTM A500 Grade B	1.4	1.3
ASTM A500 Grade C	1.3	1.2
ASTM A501	1.4	1.3
ASTM A53 (Pipe)	1.6	1.2
ASTM A1085	1.25	1.15
Steel Reinforcement		
A615 Grade 60	1.2	1.2
A615 (Grades 75 and 80)	1.1	1.2
A706 (Grades 60 and 80)	1.2	1.2

EXPECTED YIELD AND TENSILE STRENGTH RATIOS FOR THE 2016 *SEISMIC PROVISIONS*

The data for steel reinforcement and HSS were used to refine the R_y and R_t values in the 2016 *Seismic Provisions* (Table 21). The original R_y and R_t of 1.4 and 1.3 for HSS were kept for ASTM A500 Grade B and ASTM A501, respectively. These values corresponded well to calculated yield and tensile ratios for A500 Grade B. With relatively few data points, the information for A501 was insufficient to justify lower R_y and R_t values. A53 pipe data confirmed the original R_y of 1.6. The limited data were insufficient, however, to justify an R_t value lower than 1.2. Data for ASTM A500 Grade C motivated reductions of R_y and R_t to 1.3 and 1.2. Investigation of limited A1085 data in combination with A500 grades that satisfied A1085 limits on yield stress formed the basis for R_y and R_t values of 1.25 and 1.15. Steel reinforcement data supported R_y and R_t values of 1.2 for all grades investigated, except for an R_y of 1.1 for A615 Grades 75 and 80.

ACKNOWLEDGMENTS

This study was conducted with support from the American Institute of Steel Construction. The author would like to thank AISC staff and members of AISC Task Committee 9 (Seismic Design)—in particular, Subcommittee 6 on Composite Construction and Subcommittee 3 on Materials—for their technical assistance. Special thanks to the steel producers who provided data and to Tony Johnson, CRSI, for sharing their mill database.

REFERENCES

AISC (2010), *Seismic Provisions for Structural Steel Buildings,* ANSI/AISC 341-10, American Institute of Steel Construction, Chicago, IL.

AISC (2016), *Seismic Provisions for Structural Steel Buildings,* ANSI/AISC 341-16, American Institute of Steel Construction, Chicago, IL.

Anderson, M., Carter, C.J. and Schlafly, T.J. (2015), "Are You Properly Specifying Materials?" *Modern Steel Construction,* AISC, February.

CRSI (2012), *CRSI Mill Database: 2011 Annual Summary Report,* Concrete Reinforcing Steel Institute, Schaumburg, IL.

Liu, J., Sabelli, R., Brockenbrough, R. and Fraser, T. (2007), "Expected Yield Stress and Tensile Strength Ratios for Determination of Expected Member Capacity in the 2005 AISC Seismic Provisions," *Engineering Journal,* AISC, Vol. 44, No. 1, First Quarter, pp. 15–26.

Liu, J. (2013), "Updates to Expected Yield and Tensile Strength Ratios," *Report to the American Institute of Steel Construction,* Chicago, IL, November, 40 pages.

Steel Structures Research Update

Steel-Concrete Composite Beams at Ambient and Elevated Temperatures

JUDY LIU

INTRODUCTION

Ongoing and recently completed research on steel-concrete composite beams and floor systems at ambient and elevated temperatures is presented. The research highlighted here includes investigations into shear connector slip, composite beams with high-strength steel, and tests of real-scale composite floor systems subjected to fire and structural loading.

A parametric study incorporating effects of shear connector slip into fiber-based models of composite beams was conducted at Purdue University. This research was part of an investigation on behavior and design of composite beams subjected to fire. The researchers identified significant factors affecting the flexural capacity of partially composite beams and produced design recommendations. The research team, led by Dr. Kristi Selden, now an Associate at Wiss, Janney, Elstner Associates Inc., included Dr. Amit Varma, project Principal Investigator and Professor at Purdue University, and Dr. J.R. Mujagic, Structural Engineering Consultant.

Composite beams with different materials and components are being investigated at the University of New South Wales. Deconstructable steel-concrete composite beams and steel-timber composite beams are topics of study, but the focus for this research update is the work on composite beams with high-strength steel and concrete. The researchers have developed a validated finite element model, quantified the available rotation capacity of composite beams with high-strength materials, and produced an empirical equation to predict this capacity. The research is a collaboration among Dr. Huiyong Ban, Research Associate, Department of Civil Engineering, Tsinghua University; Dr. Mark Bradford, Laureate Professor in the School of Civil and Environmental Engineering and Research Director in the Centre for Infrastructure Engineering and Safety (CIES) at the University of New South Wales (UNSW); and Dr. Brian Uy, Professor in Civil and Environmental Engineering at UNSW and Director in CIES.

Tests of real-scale composite floor systems subjected to fire and structural loading will be conducted at the National Fire Research Laboratory (NFRL) at the National Institute of Standards and Technology (NIST). This series of tests will take advantage of the unique capabilities of the recently expanded and renovated NFRL with two-story, multi-bay specimens. The experiments will be used to investigate behavior of composite floor systems in fire with respect to factors such as symmetry in framing (i.e., orientation of secondary beams in adjacent bays), concrete slab/metal deck geometry as it affects the development of a compression ring, restraint of thermal expansion provided by connections, and fire exposure. Dr. John Gross and Dr. Lisa Choe, Research Structural Engineers, lead this experimental research at NIST.

SHEAR STUD SLIP IN PARTIALLY COMPOSITE BEAMS

Steel-concrete composite beams are designed using a strength-based approach outlined by the AISC *Specification for Structural Steel Buildings* (2010). However, the load-slip behavior of headed stud anchors can affect the flexural capacity of partially composite beams. A benchmarked fiber-based model was utilized in a parametric study to evaluate effects of beam length, percent composite action, and other properties. Observations on shear connector ductility and strength by Oehlers and Sved (1995) and Mujagic and Easterling (2009) were incorporated into the design of the study. Results of the parametric study were synthesized into recommendations for design of composite beams (Selden et al., 2015).

Composite Beam Model

A fiber-based model was developed for use in the parametric study. This model was capable of capturing the section-level moment-curvature behavior of a composite beam. The two-dimensional cross section was divided into individual fibers with appropriate geometry and material stress-strain relationships. At the steel-concrete interface, a slip strain was used to account for slip of the shear stud and was based on

---

Judy Liu, Ph.D., Research Editor of the AISC Engineering Journal, Professor, University of Oregon, School of Civil and Construction Engineering, Corvallis, OR. Email: judy.liu@oregonstate.edu

the load-slip relationship by Zhao and Kruppa (1997). The shear connector slip was assumed to be evenly distributed along the length of the beam. It should be noted that shear studs used in decks oriented perpendicular to the beam span have less stud slip capacity as compared to studs in a flat slab (Selden et al., 2015).

The fiber-based model was benchmarked against results from experiments and analyses of three-dimensional finite models. Details can be found in Selden (2014). For the fiber model and a three-dimensional finite element model (FEM) of a simply supported composite beam, Figure 1a shows comparisons of shear stud slip to stud location along the length of a beam with 80% composite action. Figure 1b shows these same comparisons for a beam with 40% composite action. The figures demonstrate the validity of the fiber-based model as well as the increase in stud slip with a decrease in composite action.

Parametric Study

Various geometric and material properties and their effects on the maximum moment capacity of the composite beam were investigated. The study included flat concrete slabs and concrete on steel corrugated deck with the deck oriented perpendicular to the beam span. The full range of composite action, from 0 to 100% composite, was considered in order to fully evaluate any trends in behavior. Additional parameters included maximum allowable slip of the shear studs, steel material properties, and beam length. Sample composite beam details for the results presented here are W12×19 steel sections; 5½ in-thick normal weight concrete slab or 3-in. metal deck with 2½-in. normal weight concrete topping; ¾-in.-diameter shear studs; and beam lengths of 13, 25 and 35 ft. Full ranges and details can be found in Selden (2014).

Effects of Degree of Composite Action, Beam Length, Allowable Stud Slip

Fiber model results were normalized with respect to the nominal moment capacity calculated following the AISC *Specification* (AISC, 2010); the normalized value is denoted as $M/M_{n,AISC}$. Normalized moment values were evaluated for varying degree of composite action, η, with 1.0 corresponding to 100% composite action. Comparisons were also made with parameters such as beam length and maximum allowable stud slip.

The moment capacity is sensitive to the degree of composite action and the beam length. As the degree of composite action decreases, so does the effect of slip at the steel-concrete interface and the deviation of the moment capacity from the nominal moment capacity. The partially composite beams are unable to reach the nominal moment capacity due to slip of the shear studs. Increasing the length of the beam further reduces the moment capacities for the partially composite beams. Figure 2a shows trends in normalized moment for degree of composite action and beam length for flat slab cases. Figure 2b shows these trends for cases with perpendicular deck.

The moment capacity is also sensitive to the ductility of the shear connectors or the maximum allowable stud slip. An initial 0.20 in. was used for maximum allowable stud slip for the flat slab case; this corresponded to the deformation at the peak shear force. Without modifying the initial load-slip model, the maximum allowable stud slip was increased to 0.35 in., and a constant shear force was assumed for 0.20 in. to 0.35 in. of slip. For the perpendicular deck case, the initial and increased allowable stud slip values were 0.13 in. and 0.25 in. The comparisons for normalized moment, degree of composite action, and allowable stud slip are shown in Figure 3a for the flat slab cases and Figure 3b for the

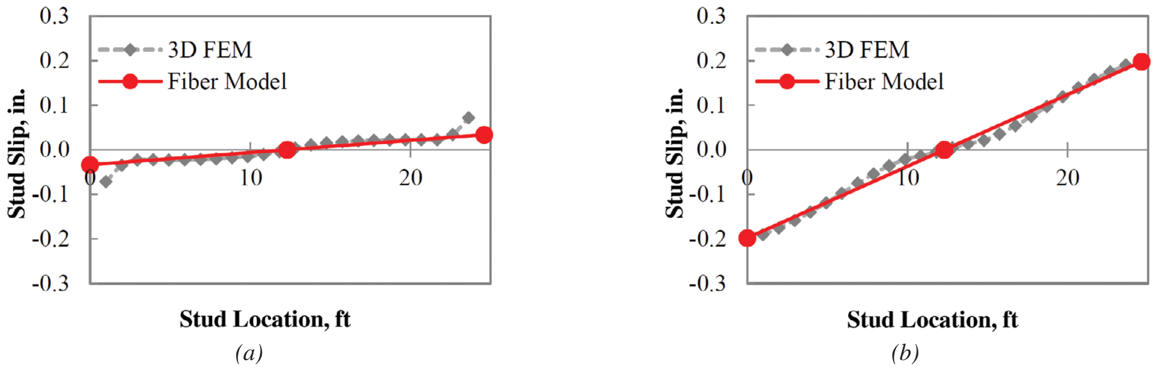

Fig. 1. Comparison of stud slip to stud location for (a) 80% composite action and (b) 40% composite action.

perpendicular deck cases. The increases in allowable slip increase the moment capacities achieved before reaching the shear slip capacity.

Summary and Recommendations

A parametric study utilizing fiber-based models of composite beams and considering the load-slip behavior of the shear studs demonstrated reductions in moment capacity due primarily to three factors: degree of composite action, beam length, and maximum allowable slip of the shear connector. The results summarized here and presented in Selden (2014) led the researchers to recommend that composite beams be designed with a minimum of 50% composite action (Selden et al., 2015).

A complementary study has investigated shear connector slip and implications for design of composite beams and girders in the United States and has provided additional recommendations (Mujagic et al., 2015). The researchers created a database of "practically occurring composite beams and girders" that satisfy AISC *Specification* requirements (AISC, 2010), 2015 IBC (ICC, 2015) loading criteria, and common detailing and fabrication requirements. Within that database, they investigated the ductility of shear connectors, making observations of configurations that exhibited significant deviations between the available and required ductility of those shear connectors. Their observations and design recommendations can be found in Mujagic et al. (2015).

COMPOSITE BEAMS WITH HIGH-STRENGTH MATERIALS

Use of high-strength (HS) steel in composite beams increases loading capacity and reduces self-weight. Additional benefits may be realized by pairing HS steel with HS concrete. However, the post-yield performance (e.g., ultimate strain capacity) of HS steel is not as good as for conventional

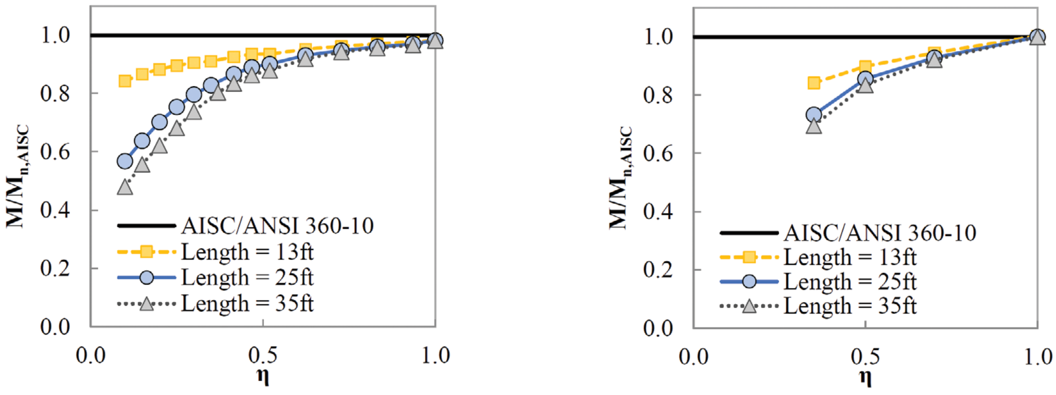

(*a*) (*b*)

Fig. 2. Normalized moment, degree of composite action, and beam length for (a) flat slab and (b) perpendicular deck.

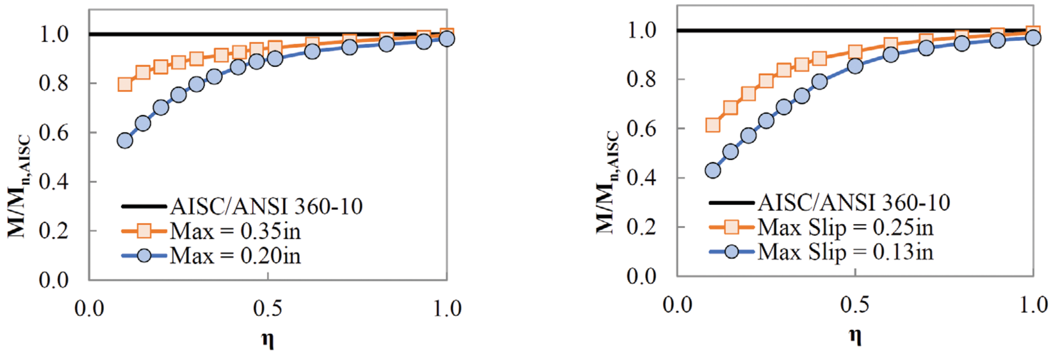

(*a*) (*b*)

Fig. 3. Normalized moment, degree of composite action, and allowable stud slip for (a) flat slab and (b) perpendicular deck.

steels, and there is limited research on the structural behavior of composite beams with HS steel (Ban et al., 2016). Ban and colleagues note that "the plastic deformation and loading capacities of composite beams incorporating HS materials would logically have different features to those with conventional materials. As a result, relevant knowledge that provides an understanding of the structural performance of such members is much needed."

Research Objectives and Methods

Ban et al. (2016) worked to quantify the ductility of composite beams with HS steel and HS concrete using a validated three-dimensional finite element model. Specifically, the rotation capacities of numerous models of composite beams with HS materials in positive bending were measured. Rotation capacity was defined as the ratio of the ultimate rotation, θ_u, at the maximum moment, M_u, to the yield rotation, θ_y, at the yield moment, M_y. Effects of parameters such as steel strength, concrete strength, degree of shear connection, presence of profiled steel decking, and beam span-to-depth ratio were explored. Results were used to develop a nonlinear empirical equation for prediction of rotation capacity of composite beams with HS materials, as well as recommendations for ductility of shear connectors.

Finite Element Model

The finite element model used in this study was based on prior work in ABAQUS by Ban and Bradford (2013). Shell elements (S4R) were used for the steel beam. Connector elements (CONN3D2) were used for the shear connectors. For models with profiled steel decking, solid elements (C3D8) were used for the concrete, shell elements (S4R) were used for the metal deck, and truss elements (T3D2) were used for the reinforcing steel. Figure 4 shows the steel beam, reinforcing steel, and concrete for a flat slab composite beam model.

Material models included a multilinear isotropic hardening model for the steel beam and an elastic-perfectly plastic model for the reinforcing steel. A damage-plasticity model was used for the concrete. For the shear connectors, the load-slip relationship by Ollgaard et al. (1971) was used. Large slip capacities were deliberately assigned so as to avoid shear interaction failure in the analyses. Additional details for the finite element model can be found in Ban et al. (2016).

The finite element model was validated through modeling of 27 steel-concrete composite beams (from four different studies) and comparisons against reported test results for those beams. Reported yield strengths for the steel

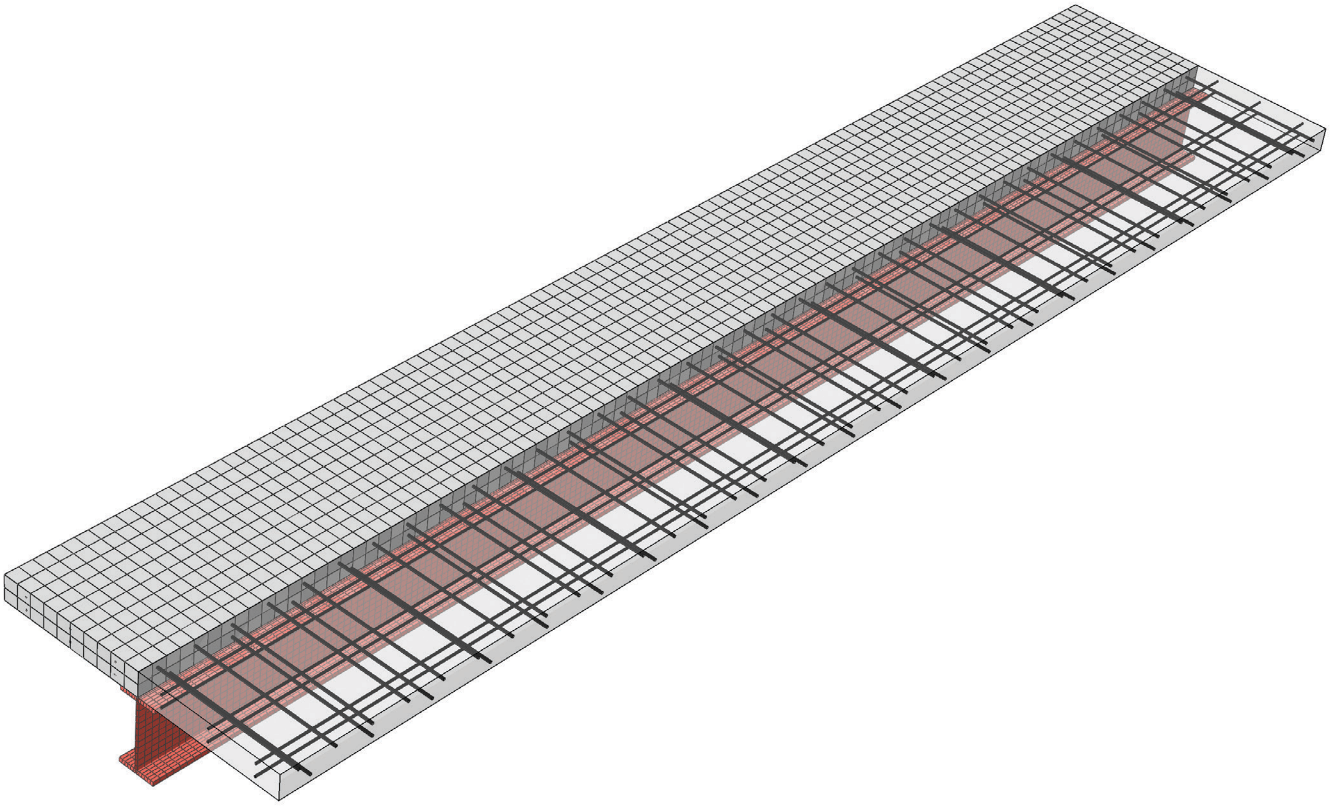

Fig. 4. Finite element model of a flat slab composite beam.

beams ranged from 31 to 109 ksi, and concrete compressive strengths ranged from 2.90 to 11.1 ksi. The experimental results were from one-point, two-point, and uniformly distributed load tests on composite beams. The finite element model was able to predict the ultimate moment capacities of the composite beams to within ±5%. Comparisons of load or moment versus mid-span deflection also showed good agreement between the finite element model and test results for initial stiffness and failure modes (Ban et al., 2016).

Parametric Study

A total of 1,380 composite beams were modeled for a parametric study that considered effects of the material properties, the shear connections, section geometry, and initial imperfections. Ten grades of steel, with yield strengths ranging from 34 to 139 ksi, were included. Concrete compressive strengths ranged from 2.90 to 14.5 ksi. Nine different degrees of shear connection and three distribution patterns (e.g., uniform, concentrated toward supports) were modeled. Five different cross sections, solid slabs and slabs with profiled steel decking, and seven ratios of beam span (L) to total depth (D) were studied, with L/D ranging from 13.75 to 45.0. Initial imperfections included initial geometric imperfections and residual stresses in the steel beam. Details can be found in Ban et al. (2016).

Parameters that had little to no influence on the available rotation capacity, or ductility, of the composite beams were the degree of shear connection, distribution patterns for the shear connectors, cross-sectional dimensions, solid slabs or slabs with profiled steel decking, initial geometric imperfections, and residual stresses.

Rotation capacities generally increased as the steel yield strength decreased. Conversely, the rotation capacities tended to increase as the concrete strength increased, although this trend was not as pronounced as the trend with steel strength. The combined steel and concrete strength effect can be described using the depth ratio of the plastic neutral axis, x_{pl}, defined as the distance between the plastic neutral axis and the extreme fiber of the concrete slab in compression divided by the overall depth (D). The available rotation capacity increases as x_{pl} decreases.

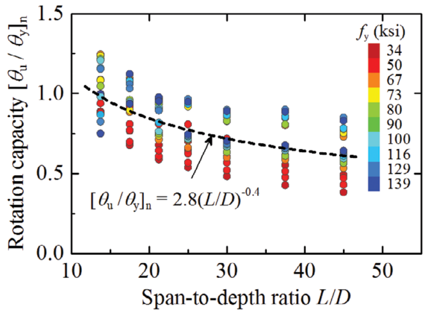

Fig. 5. Rotation capacity relationship to span-to-depth ratio.

The span-to-depth ratio was another significant parameter. The available rotation capacity decreases with an increase in L/D, as shown in Figure 5. This is because "higher levels of development of the curvature and of the steel plasticity are demanded for composite beams with larger L/D values" but are limited by "the nearly constant ultimate strain for different concrete strengths" (Ban et al., 2016).

Empirical Equation and Recommendations

Based on the results of the parametric study, an empirical equation for available rotation of composite beams was developed. This equation (Equation 1) considers steel yield strength (f_y), depth ratio of the plastic neutral axis (x_{pl}), and span-to-depth ratio (L/D). The predicted rotation capacities from the empirical equation compare favorably to those from the finite element analysis results, within ±15% (Figure 6). As with the finite element model, the empirical equation can be used for predictions for composite beams with conventional strength or HS materials. Given the available rotation capacities for composite beams, the researchers are currently investigating the required rotation capacities in composite beams and frames with HS materials (Ban et al., 2016).

$$\frac{\theta_u}{\theta_y} = \frac{507.6(e)^{-1.7x_{pl}}}{f_y\left(L/D\right)^{0.4}} + 1 \tag{1}$$

As noted earlier for the shear connectors, large slip capacities were deliberately assigned so as to avoid shear interaction failure in the analyses. In the parametric study, for steel yield strengths less than 67 ksi or concrete compressive strengths greater than 10 ksi, slip was less than 0.24 in. However, results also showed increasing maximum slip of

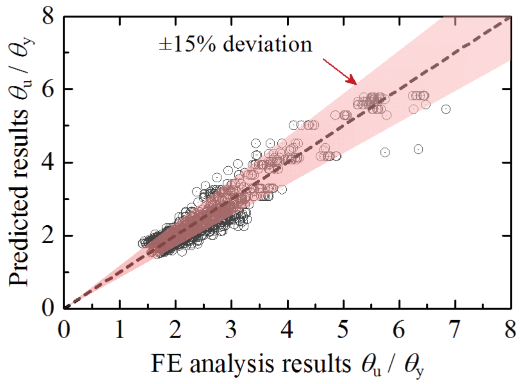

Fig. 6. Predicted rotation capacities for equation and finite element analysis.

the connectors with increase in steel yield strength. Ban et al. (2016) recommend slip capacities of 0.35 or 0.47 in. for different combinations of steel yield and concrete compressive strength.

FIRE-STRUCTURE INTERACTION

The National Institute of Standards and Technology (NIST) is planning a series of real-scale experiments at the recently renovated National Fire Research Laboratory (NFRL). This series focuses on the performance of steel-concrete composite floor systems in fire, with the aim to provide technical information, through experimental tests, for advancing performance-based design for fire conditions. The motivation for the investigation dates back to NIST research on the fire-induced collapse of the World Trade Center (WTC) 7 building. The WTC investigation identified potential vulnerabilities of composite floor systems in uncontrolled fires with issues related to structural layout, sources of thermal restraint, and connections. Meanwhile, two recent stakeholder workshops at NIST (Almand, 2012; Yang et al., 2015) presented the large-scale structural-fire testing capabilities of the NFRL and unprecedented opportunities for research. Among the priorities defined at the workshops: conduct three-dimensional full-scale tests on structural systems and contribute to the “generation of a database of large-scale experiments documenting the performance of structural connections, components, subassemblies, and systems under realistic fire and loading conditions for validation of analytical models” (Yang et al., 2015). Also, as stated in Almand (2012), “a focus on large scale experiments related to the many unanswered questions about composite floor system performance would have great practical import and a major impact on design methods.”

National Fire Research Laboratory (NFRL)

The National Fire Research Laboratory (NFRL) at NIST was expanded in 2015 and can “accommodate experiments on real-scale structural systems and components up to two stories in height and 2 bays × 3 bays in plan.” (Bundy et al., 2016). High-bay areas include a strong floor, strong wall, overhead cranes, exhaust hoods, an emissions control system (ECS), and a hydraulic loading system, enabling testing of structures under realistic fire and structural loading. The exhaust hood above the strong floor is used for quantification of the heat release rate as a function of time, and retractable side skirts on the hood can be positioned to improve smoke capture. Hydraulic actuators can be mounted underneath the strong floor. Figure 7 shows a cross section of the NFRL and a photograph of calibration of the heat release rate measurement system with a 10-MW fire. Additional

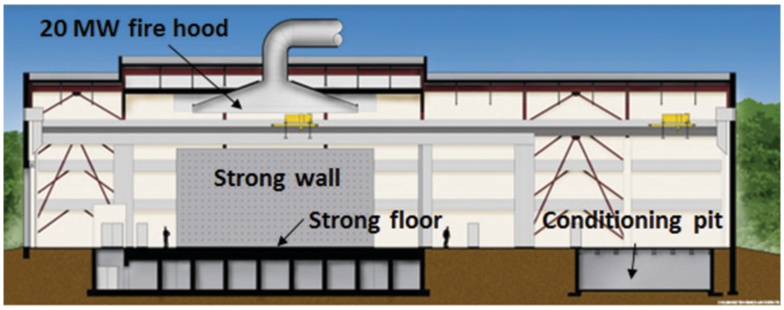

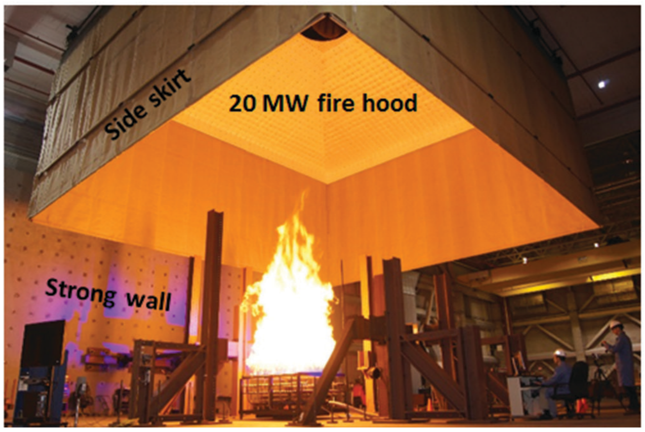

Fig. 7. Section view of the NFRL and calibration of heat release rate measurement system.

details of the NFRL and its capabilities can be found in Bundy et al. (2016).

Research Plan

Of the "unanswered questions about composite floor system performance" (Almand, 2012) in steel frame construction, NIST has focused a number of important factors for behavior in fire, as identified in the literature. The primary objectives for the experiments are to characterize behavior of the composite floor system and to improve models that can be used for performance-based design of steel frame buildings for fire.

Test Specimen and Test Parameters

A two-story, two-bay by three-bay composite floor system is to be experimentally investigated. Story heights are 11 ft, and the test bay is 20 ft by 30 ft. Figure 8 shows a plan view of the test frame shaded in gray, with the test bay in dark gray. An outline of the hood shows its placement above the test bay. Note that the test bay can be configured as an interior, edge or corner bay of a building, as illustrated by the dashed lines in Figure 8. Also shown at the East and West perimeters are bracing modules. Restraint on the East side can be varied through use of actuators. The North–South frames can also be braced at the strong wall.

Parameters to be investigated in the tests include the orientation of secondary beams in adjacent bays (i.e., "symmetry in framing" or "balanced framing"), geometry and orientation of the deck (and floor framing) with regard to formation of a compression ring, test bay location (corner, edge or interior bay), and types of beam to girder connections (bolted double-angle or single-plate shear connections). Also varied are the magnitude and location of service gravity loads using six actuators located underneath the strong floor (Figure 9).

Parameters related to the fire loading are the thickness of the spray-applied fire resistive materials (SFRM), fires on

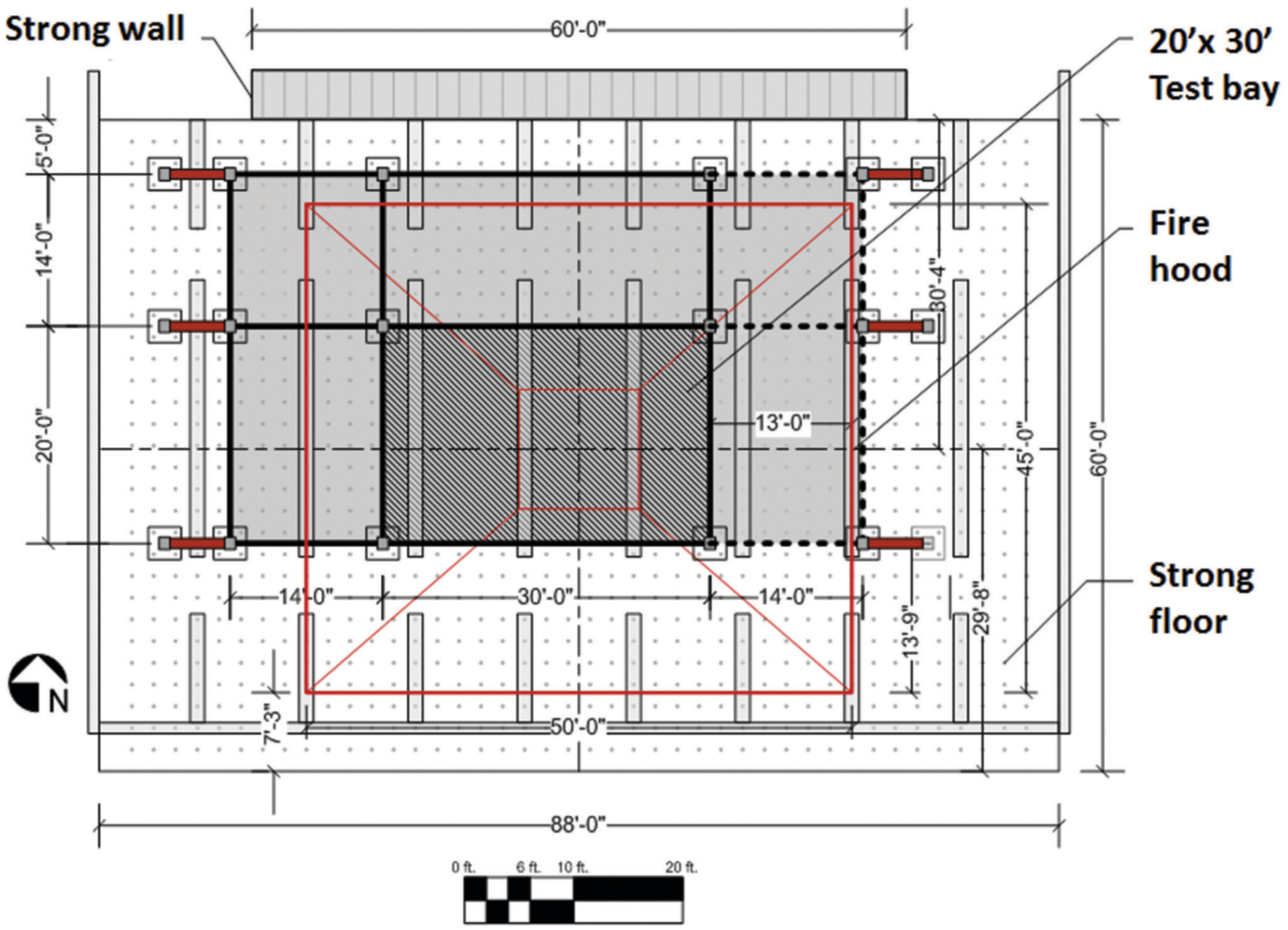

Fig. 8. Plan view of the test frame.

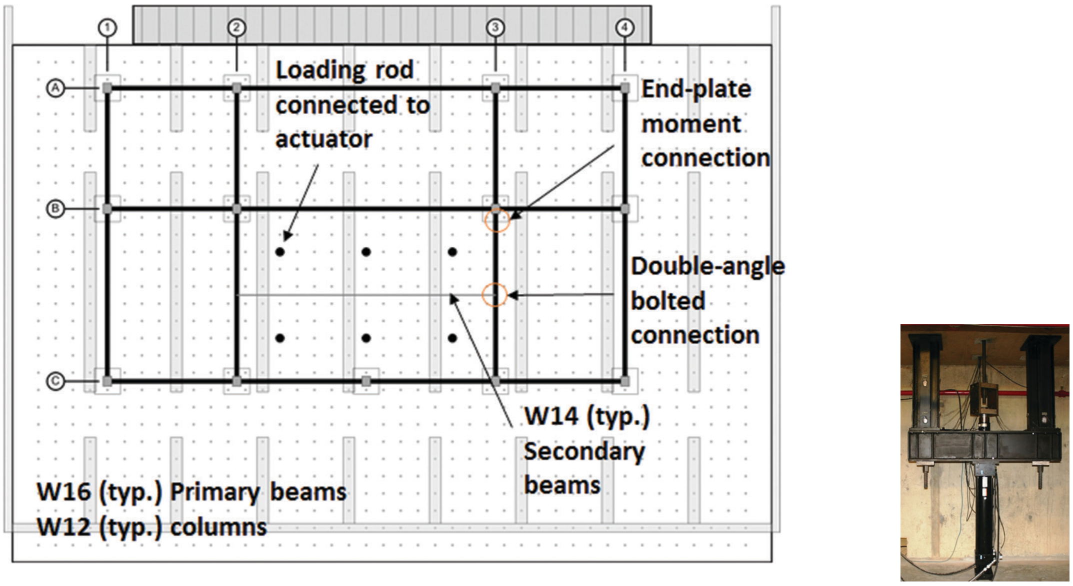

(a) (b)

Fig. 9. (a) Locations of service gravity loads; (b) actuator mounted underneath the strong floor.

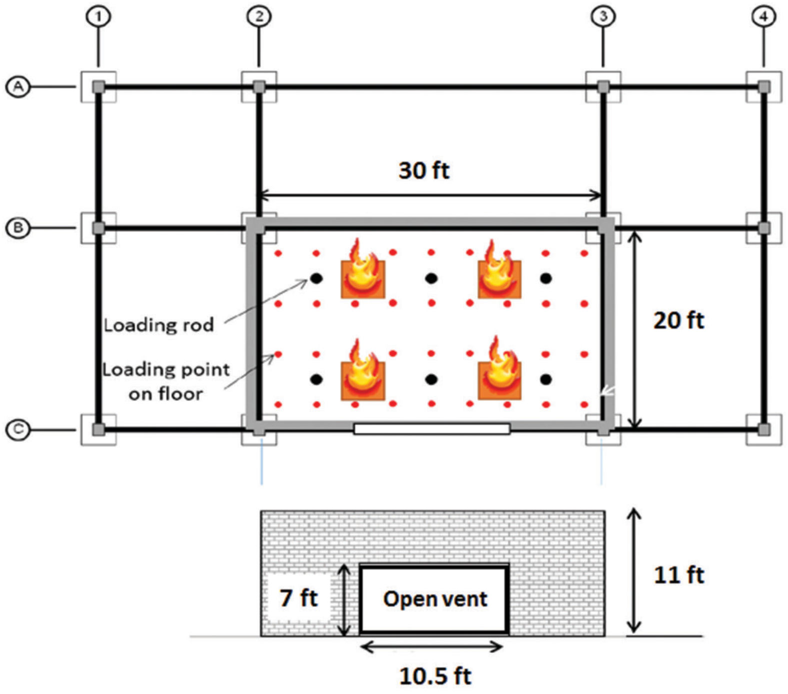

Fig. 10. Schematic of the test bay, burners, loading points, and enclosure.

multiple floors, and fire conditions (e.g., severity, duration, and location of the proposed structural fire). Figure 10 is a schematic of the test bay, showing locations of natural gas burners, locations of gravity loading points, and the outline of the enclosure with an open vent on one side as shown in the elevation drawing. The four burners can simulate a fire traveling through the room. Additional details on the test program, including development of and specifics on the fire loading, can be found in Choe et al. (2016) and Manzello and Suzuki (2015).

Expected Outcomes

The tests planned at the NFRL represent a major advance in real-scale testing of steel-concrete composite floor systems under fire and structural loading. The two story, multi-bay test specimens and test matrix capture a broad spectrum of geometric, design and loading parameters. The temperature and structural response data, through heating and cooling phases, will be extremely valuable for validation of physics-based models for prediction of structural performance under fire. As such, this research will provide important steps forward for performance-based standards for fire resistant design of steel buildings.

SUMMARY

A few studies on steel-concrete composite beams and floor systems at ambient and elevated temperatures were highlighted. A parametric study with fiber-based models incorporating effects of shear connector slip was used to identify significant factors affecting the flexural capacity of partially composite beams and produce design recommendations. A validated finite element model was used to quantify the available rotation capacity of composite beams with high-strength materials and in the development of an empirical equation to predict this capacity. Tests of real-scale composite floor systems subjected to fire and structural loading will take advantage of the unique capabilities of the NFRL and provide valuable data to help answer questions about the performance of these systems under fire.

ACKNOWLEDGMENTS

Special thanks to Lisa Choe, Kristi Selden, and Huiyong Ban for their contributions to this article. Amit Varma provided technical support and direction for this research update. The research on shear connector slip was based upon work funded by the National Science Foundation (NSF) Award No. 0758461, the American Iron and Steel Institute (AISI), and the American Institute of Steel Construction (AISC). The work on composite beams with high-strength steel was supported by an Australian Research Council (ARC) Linkage Project (LP 150101196), awarded to Mark Bradford and Brian Uy for collaborative research involving the University of New South Wales (UNSW); Tsinghua University; and China Construction Steel Structure Corporation—as well as an Australian Laureate Fellowship (FL100100063) awarded to Mark Bradford. Huiyong Ban was supported through a Research Associate Fellowship provided by the School of Civil and Environmental Engineering at UNSW. The fire-structure interaction experimental program is supported by the Engineering Laboratory of the National Institute of Standards and Technology. The technical contributions of John Gross, William Grosshandler, and Matthew Bundy are also gratefully acknowledged.

REFERENCES

AISC (2010), *Specification for Structural Steel Buildings*, ANSI/AISC 360-10, American Institute of Steel Construction, Chicago, IL.

Almand, K. (2012), "Structural Fire Resistance Experimental Research—Priority Needs of U.S. Industry," National Fire Protection Association, Fire Protection Research Foundation, Quincy, MA.

Ban, H. and Bradford, M.A. (2013), "Flexural Behaviour of Composite Beams with High Strength Steel," *Engineering Structures,* Vol. 56, November, pp. 1,130–1,141.

Ban, H., Bradford, M.A., Uy, B. and Liu, X. (2016), "Available Rotation Capacity of Composite Beams with High-Strength Materials under Sagging Moment," *Journal of Constructional Steel Research,* Vol. 118, March, pp. 156–168.

Bundy, M., Hamins, A., Gross, J., Grosshandler, W. and Choe, L. (2016), "Structural Fire Experimental Capabilities at the NIST National Fire Research Laboratory," *Fire Technology,* Vol. 52, No.4, pp. 959–966.

Choe, L., Gross, J., Grosshandler, W. and Bundy, M. (2016), "Fire-Structure Interaction Experiment Plan for a Full-Scale Composite Floor System," National Institute of Standards and Technology, Gaithersburg, MD. (Manuscript in preparation)

ICC (2015), *International Building Code*, International Code Council, Falls Church, VA.

Manzello, S. and Suzuki, S. (2015), "Summary of Workshop for Fire Structure Interaction and Large Outdoor Fires," NIST SP 1189, National Institute of Standards and Technology, Gaithersburg, MD.

Mujagic, J.R.U. and Easterling, W.S. (2009), "Reliability Assessment of Composite Beams," *Journal of Constructional Steel Research,* Vol. 65, pp. 2,111–2,128.

Mujagic, J.R.U., Easterling, W.S., Bennett, J.S. and Varma, A.H. (2015), "Assessment of Shear Connection Ductility in Composite Beams—Implications on the U.S. Design Practice," Report No. CE/VPI-15/12, Virginia Polytechnic Institute and State University, Blacksburg, VA.

Oehlers, D.J. and Sved, G. (1995), "Composite Beams with Limited-Slip-Capacity Shear Connectors," *Journal of Structural Engineering,* ASCE, Vol. 121, pp. 932–938.

Ollgaard, J.G., Slutter, R.J. and Fisher, J.W. (1971), "Shear Strength of Stud Connectors in Lightweight and Normal-Weight Concrete," *Engineering Journal,* AISC, Vol. 8, No. 2, Second Quarter, pp. 55–64.

Selden, K.L. (2014), *Structural Behavior and Design of Composite Beams Subjected to Fire*, Ph.D. Dissertation, Purdue University, West Lafayette, IN.

Selden, K.L., Varma, A.H. and Mujagic, J.R. (2015), "Consideration of Shear Stud Slip in the Design of Partially Composite Beams," *SEI Structures Congress 2015*, Portland, OR, pp. 888–899. doi: 10.1061/9780784479117.076.

Yang, J., Bundy, M., Gross, J., Hamins, A., Sadek, F. and Raghunathan, A. (2015), "International R&D Roadmap for Fire Resistance of Structures," *Summary of NIST/CIB Workshop* (NIST SP 1188), National Institute of Standards and Technology, Washington, DC.

Zhao, B. and Kruppa, J. (1997), "Fire Resistance of Composite Slabs with Profiled Steel Sheet and of Composite Steel Concrete Beams Part 2: Composite Beams." Final Report, ECSC—Contract No. 7210 SA 509, CTICM, France.